REPAIR OF BRIDGE STEEL GIRDERS DAMAGED BY DISTORTION-INDUCED
FATIGUE
By

Fatih Alemdar

Submitted to the graduate degree program in Civil Engineering and the Graduate Faculty of the
University of Kansas in partial fulfillment of the requirements for the degree of Doctor of
Philosophy.

_____

Chairperson Dr. Adolfo B. Matamoros

_____

Dr. Caroline R. Bennett

_____

Dr. Ronald M. Barrett

_____

Dr. JoAnn Browning

_____

Dr. Stanley Rolfe

Date Defended: 10/26/2011

The Dissertation Committee for Fatih Alemdar
certifies that this is the approved version of the following dissertation:

REPAIR OF BRIDGE STEEL GIRDERS DAMAGED BY DISTORTION-INDUCED
FATIGUE

_____

Chairperson: Adolfo B. Matamoros

Date approved: 12/07/2011

ABSTRACT

This study investigates the repair of steel bridge girders damaged by distortion-induced fatigue. The study is presented in three parts. The first part describes finite element modeling techniques used to evaluate the potential for fatigue cracks in steel girders subjected to distortion-induced fatigue. The modeling techniques employed in this study were intended to identify areas near welded connections in bridge girders with the highest potential for developing fatigue cracks, and to evaluate the effectiveness of retrofit measures in reducing the potential for crack propagation near welded connections with existing fatigue cracks. Computer simulations correlated well with experimentally observed crack patterns and were useful in providing an indication of the effectiveness of various retrofit measures.

The second part of the study investigates the use of composite materials to repair fatigue damage in steel girders. A total of 17 specimens with pre-existing fatigue cracks were tested under cyclic loading to evaluate the performance of composite overlays when used to repair fatigue damage in steel structures. Two control specimens were tested without overlays and the remaining 15 were repaired with Carbon Fiber Reinforced Polymer (CFRP) overlays of various thicknesses. Results indicate that this method was very effective, and that proper implementation of this type of repair can reduce the crack propagation rate to negligible values.

The third part of the study consisted of physical and computer simulations of 914-mm (36-in.) deep girder-cross frame subassemblies subjected to cyclic loading. The simulations were carried out to investigate the stress demands caused by distortion-induced fatigue and to evaluate the effectiveness of various retrofit measures. Previously used repair methods for distortion-induced fatigue damage have attempted to reduce the stress demand in the web gap

region by increasing the flexibility of cross-frame to girder connection or by restraining the lateral motion of the cross-frame by attaching the connection plate to the slab. A new retrofit approach was investigated in this study designed to reduce the stress demand in the web gap region by distributing the force at the girder-cross frame connection over a larger area. A new retrofit detail is proposed based on this approach, which consists of adding steel angles connecting the girder web and the connection plate, and a steel bar on the back side of the girder web to distribute the lateral force over a wider region of the web. Experimental and computer simulation results are presented showing that this repair method is very effective in preventing the growth of horseshoe-shaped cracks around the web-cross frame connection and of straight cracks near the junction between the flange and web.

ACKNOWLEDGEMENTS

TABLE OF CONTENTS

LIST OF FIGURES

LIST OF TABLES

LIST OF SYMBOLS

Symbol	Description	Units (SI, US Imp.)
a	Crack Length	[mm], [in.]
d	Depth	[mm], [in.]
E	Modulus of Elasticity	[MPa], [ksi]
f	Flexible	
L	Specimen Length	[mm], [in.]
m	Medium	
N	Fatigue Loading Cycles	
s	Stiff	
t	Thickness	[mm], [in.]
x	Longitudinal Distance	[mm], [in.]
Δy	Change in Deflection	[mm], [in.]
$\Delta\sigma$ or dS	Stress Range	[MPa], [ksi]
ε	Strain	[mm/mm], [in./in.]
σ	Stress	[MPa], [ksi]

LIST OF ACRONYMS

Acronym	Description
A	Angle
AASHTO	American Association of State Highway and Transportation Officials
BP	Back Plate
CFRP	Carbon Fiber Reinforced Polymer
CP	Connection Plate
DOT	Department of Transportation
FEA	Finite Element Analysis
FRP	Fiber Reinforced Polymer
HSS	Hot Spot Stress
LRFD	Load and Resistance Factor Design
LVDT	Linear Variable Differential Transformer
MVCCT	Modified Virtual Crack Closure Technique
SIF	Stress Intensity Factor
XFEM	Extended Finite Element Method

LIST OF SUBSCRIPTS

c	Critical
FRP	Fiber Reinforced Polymer
max	Maximum
s	Steel

CHAPTER 1.   INTRODUCTION

This thesis presents a study to develop and evaluate repair methods that may be used to mitigate traffic-induced fatigue damage in steel bridge structures. Fatigue damage in steel bridges mostly occurs in areas of the bridge where there are abrupt geometry changes, or where a relatively large force is transferred through a small area. Both of these types of vulnerabilities can exist in welded connections. In some instances secondary stresses, which are difficult to quantify during the design process without sophisticated analysis models, can combine with the aforementioned vulnerabilities leading to fatigue damage. This is the case for distortion-induced fatigue, a problem that afflicts a large number of structural steel bridges designed prior to the mid-1980's.

The distortion-induced fatigue problem presents many challenges, in terms of analysis and repair. The distribution of stresses in web gap regions of steel bridges (Fig. 1-5), where fatigue cracks due to distortion-induced fatigue often originate, is very complex. Due to the complexity of the stress field, cracked areas are subjected to loadings that produce mixed mode fracture. Repairing distortion-induced fatigue damage is also difficult because geometric constraints limit the type of repair methods that can be applied to prevent further growth of fatigue cracks. Given the unique nature of this problem it is important for engineers to have at their disposal various alternatives for repair. The development of new techniques to repair distortion-induced fatigue damage is the focus of this study.

The research presented in this thesis investigates repair methods for two different types of fatigue cracks observed in web gap regions of bridges with distortion-induced fatigue damage: fracture-mode-1 type cracks and mixed-fracture-modes-1-and-3 type cracks. The method of

1

repair investigated for fracture-mode-1 cracks consisted of bonding Carbon Fiber Reinforced Polymers (CFRP) overlays over the cracks to provide an alternate load path and reduce the driving stress range at the tip of the crack. Mixed-mode cracks were repaired using a simple reinforcement scheme applied at the web gap region consisting of two angles and a back plate. In the case of mixed-mode cracks, a simple repair technique often used in steel bridges, the drilling of crack-stop holes at the tip of the fatigue cracks, was also evaluated. The findings of these two investigations are discussed in the three separate papers which follow.

The first paper is focused on the repair of distortion-induced fatigue cracks in web-gap regions of steel girders. The research comprised experimental and computer simulations of 9 ft-long girder segments subjected to distortion-induced fatigue loading applied through a cross frame. Computer simulations consisted of high-resolution Finite Element (FE) models of the girder specimen. Calculated stress demands and potential crack propagation patterns obtained from the FE simulations were found to be in excellent agreement with direct observations from the physical simulations of the specimens. Locations of maximum principal tensile stress computed with the FE models were found to be very good indicators of the propagation path followed by fatigue cracks in the girder subassemblies.

The second paper focuses on the repair of fracture-mode-1 type cracks using composite overlays. Specimens consisting of tensile coupons with existing fatigue cracks of a pre-established length were repaired with two different types of CFRP overlays. The first type of overlay was prefabricated using pre-impregnated fiber plies while the second was sprayed directly on the specimens using a chopped-fiber sprayer. Because the composite overly reduces the stress demand at the area vulnerable to fatigue damage, this technique has the advantage that it can be used in combination with small-diameter crack-stop holes avoiding excessive

2

weakening of the cross section. The experimental study showed that this repair technique was highly effective in preventive further damage to the specimens, reducing the rate of crack growth to negligible values.

The third paper is intended to summarize the various simulation techniques employed in the first two studies, and also to document the process followed in evaluating various retrofit measures on the basis of those simulation techniques. This is a topic of particular importance given the significant cost associated with physical simulations. The development of reliable simulation techniques to evaluate the potential for fatigue damage in uncracked and cracked steel members is essential for quantifying the potential for damage and for vetting repair techniques so that experimental work can focus on the most promising repair techniques.

Comparison between the behavior of test subassembly and a bridge structure

Given potential interactions between primary and secondary stresses, it is clearly preferable to test a complete bridge systems instead of subassemblies. The main advantage of testing subassemblies is that a testing program can be conducted for a fraction of the cost of testing a single bridge system. Because the former technique was employed in this study, a comparison was carried out between results from high-resolution computer simulations of the subassemblies and from complete bridge systems. This comparison provided a reference about the similarities and differences between the two. An analytical study on distortion-induced fatigue in steel bridges, comprising more than 1000 high-resolution simulations of bridge systems with similar girder dimensions as those used in the subassemblies evaluated in this study, was carried out by Hassel (2011). FE simulation results, illustrated in Figs. 1 through 5, show that the distribution of stresses in the web gap region of the subassemblies was similar to

that in the web gap region of the two-span continuous model bridge employed by Hassel. In both instances the main areas of vulnerability were at the weld between the connection plate and the girder web, and at the weld between the web and the flange.
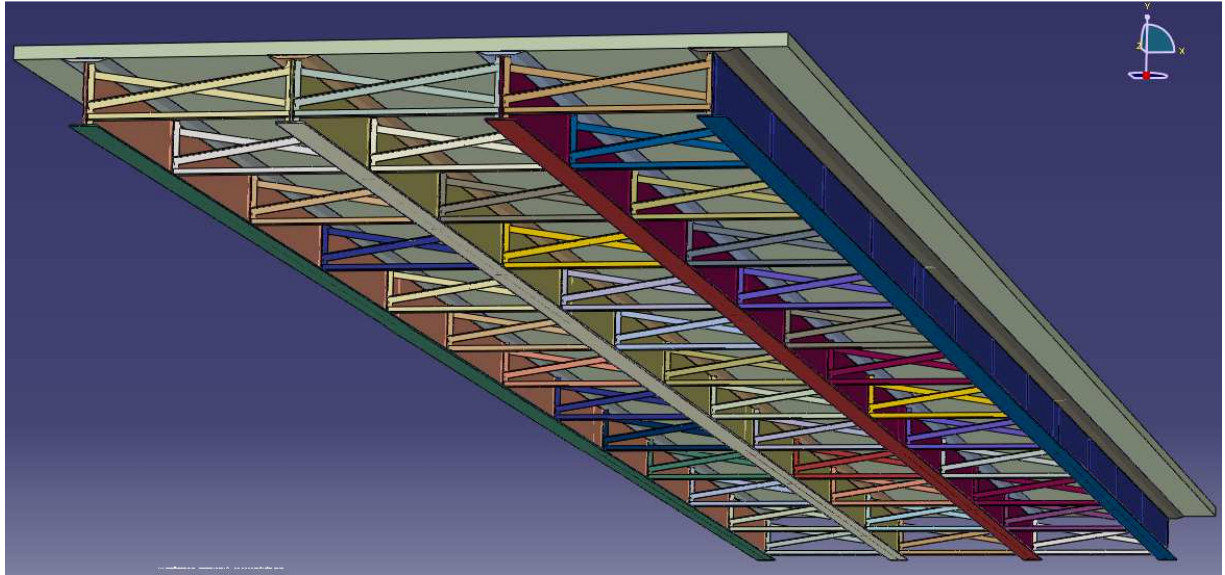
Figure 1-1: Bottom view of bridge model from simulation (Hassel, 2011)
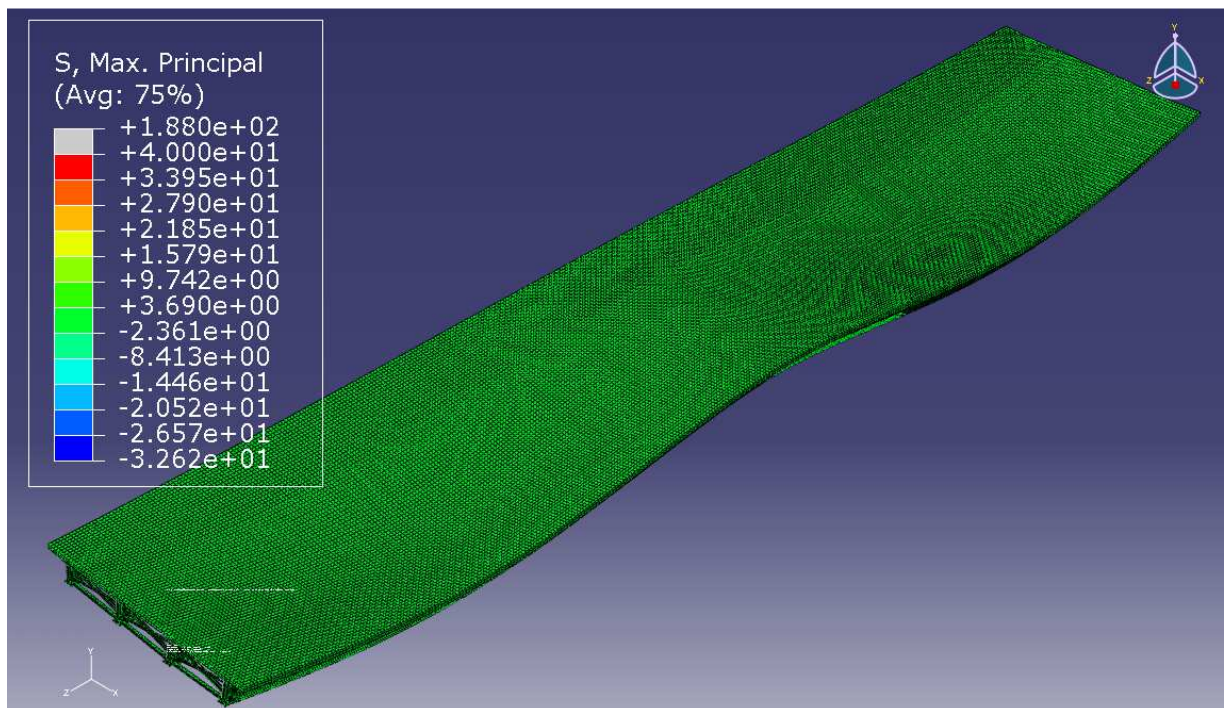
Figure 1-2: Deflected shape of the bridge model under truck load (Hassel, 2011)

4
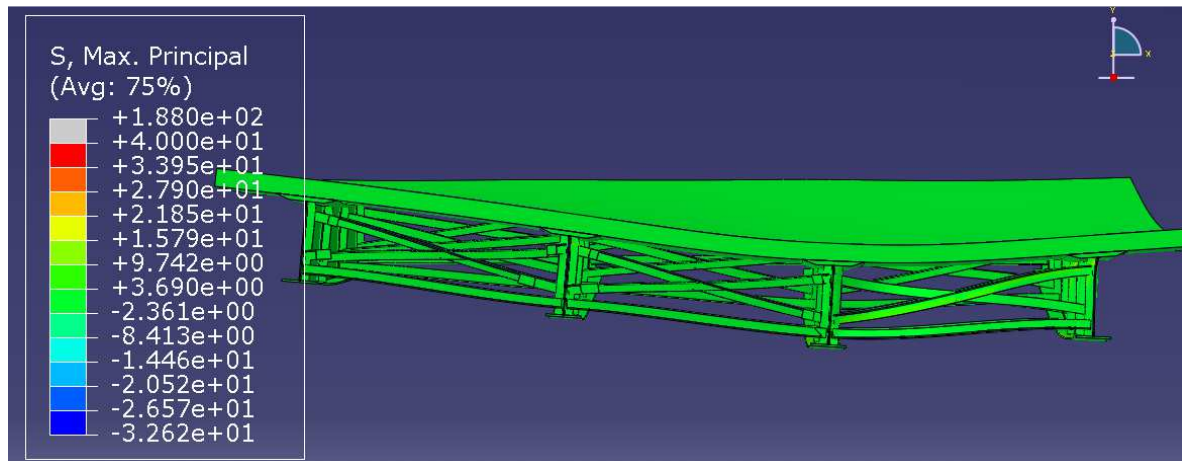
Figure 1-3: Deflected shape of bridge section in a region of positive moment (Hassel, 2011)

S, Max. Principal
(Avg: 75%)
+1.880e+02
+4.000e+01
+3.395e+01
+2.790e+01
+2.185e+01
+1.579e+01
+9.742e+00
+3.690e+00
-2.361e+00
-8.413e+00
-1.446e+01
-2.052e+01
-2.657e+01
-3.262e+01
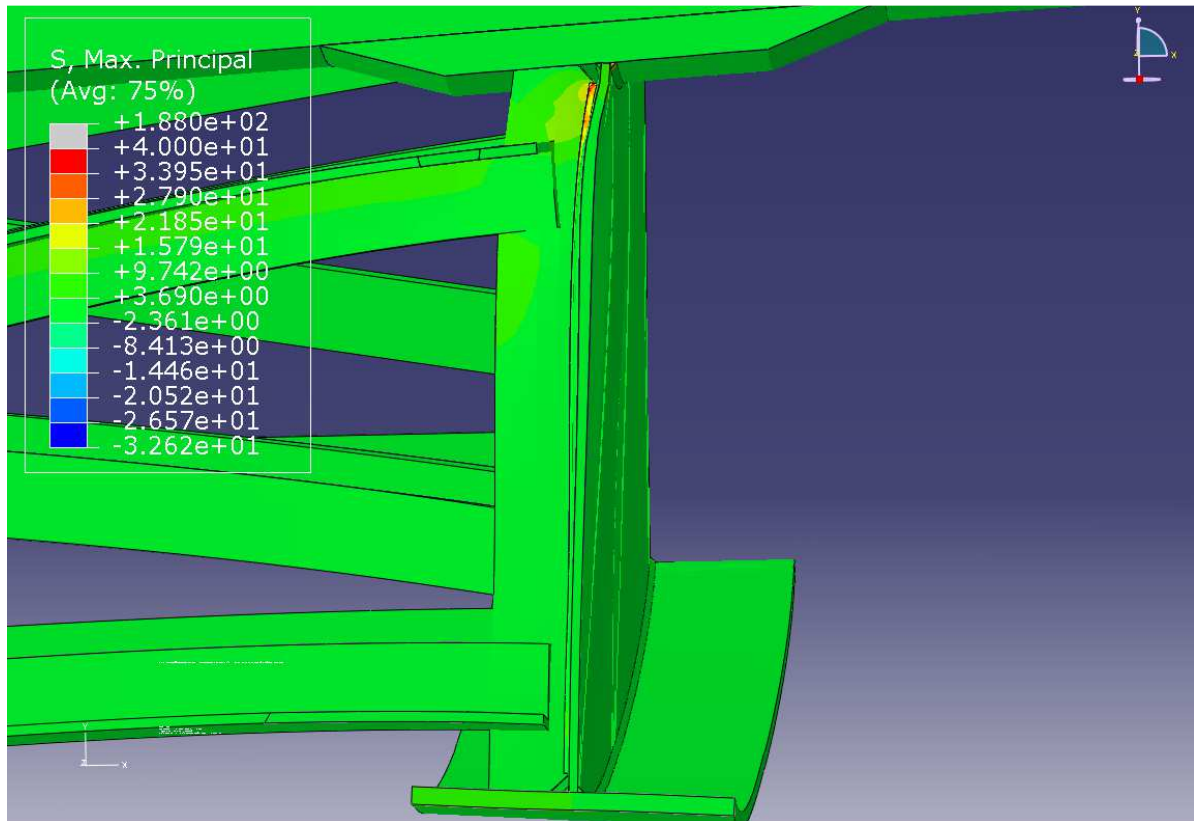
Figure 1-4: Close-up showing stress demand at the web gap region of the deflected girder (Hassel,

2011)
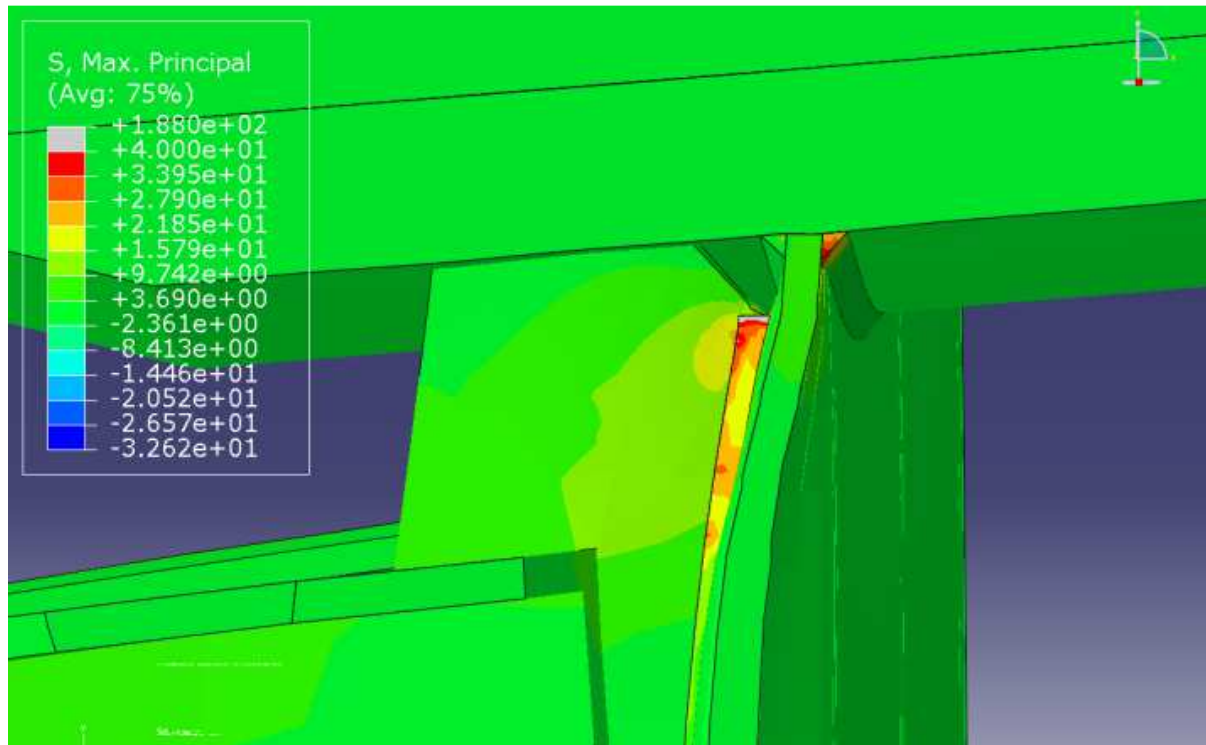
Figure 1-5: Detailed view of the stress demand at the web gap region of the an external bridge

girder (Hassel, 2011)

CHAPTER 2.   REPAIR OF DISTORTION INDUCED-FATIGUE CRACKS IN STEEL BRIDGE GIRDERS

Abstract

Several studies have identified distortion-induced fatigue as the leading cause of cracks in steel bridges built prior to the mid 1980s.   Experimental and computer simulations of a 914-mm (36-in.) deep girder-cross frame subassembly subjected to cyclic loading were carried out to study the effects of distortion-induced fatigue and to evaluate the effectiveness of various retrofits. Previous repair methods for distortion-induced fatigue damage have attempted to increase the flexibility of the web-gap region or to restrain the lateral motion by fixing the connection plate to the top flange. A new approach was investigated in this study based on reducing the web gap stress demand by re-distributing the force at the girder-cross frame connection over a larger area.

A new retrofit detail is proposed based on this approach, which consists of adding steel angles connecting the girder web and the connection plate, and a steel bar on the back side of the girder web to distribute the lateral force over a wider region of the web. Experimental and computer simulation results are presented showing that this repair method is very effective in preventing the growth of horseshoe-shaped cracks around the web-cross frame connection and of horizontal cracks near the junction between the flange and web.

Introduction and background

Fatigue cracks in steel girders are frequently found during inspections of older bridge structures (Lindberg and Schultz, 2007). These cracks generally initiate in areas of a bridge that

contain large stress concentrations induced by geometric discontinuities. A national survey on the types of fatigue cracks observed in steel bridges was performed as part of a study on distortion-induced fatigue sponsored by the Minnesota Department of Transportation (Mn/DOT) (Lindberg and Schultz, 2007). In response to the survey, DOT engineers from various states reported 11 different types of commonly observed fatigue cracks. One of the most frequently reported areas exhibiting fatigue damage were transverse stiffener web gaps in positive and negative moment regions of girders (Keating, 1994). This is consistent with a study by (Roddis and Zhao, 2001) which states that out-of-plane distortion was one of the main reasons for fatigue cracks in nationwide bridges. Roddis and Zhao, (2001) also stated that the positive moment region is more vulnerable to fatigue cracks than the negative moment region Roddis and Zhao, (2001). Deformations induced by out-of-plane distortion are illustrated in Figure 2-1. When adjacent girders experience different vertical deflections due to passing traffic, transverse stiffeners can cause out-of- plane distortion on the girder web. Out-of-plane distortion of the web gap region and the high localized deformations caused by it induce large stress demands in the web and the connection welds, which dramatically decrease the fatigue life of bridges (Jajich and Schultz, 2003).
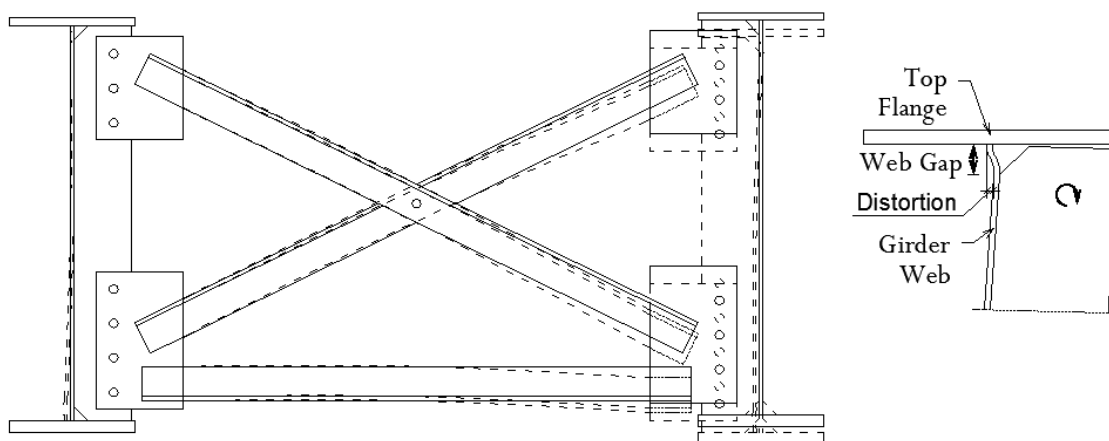
Figure 2-1 : Out of plane distortion in bridge girder

A web gap region is created when a connection plate is clipped at the top or bottom, leaving a gap between the edge of the connection plate and the unconnected girder flange (Fig. 2-1). This type of connection detail was widely used in the United States before the mid 1980s. The connection detail was implemented in this manner because it is very difficult to achieve a good quality weld at the intersection of the web and flange (Castiglioni et al., 1988), and because of fears that welding the connection plate to the tension flange would lead to fatigue damage in the flange similar to that observed in European bridges early in the last century (Roddis and Zhao, 2001). Roddis and Zhao (2001) indicate that it was common practice not to weld connection plates to the compression flange also to avoid the introduction of AASHTO fatigue category E connection details.

Retrofit techniques documented in the literature attempt to reduce the high localized stress demand by making the plate-to-web connection more flexible or by adding connectivity and increasing the stiffness. The flexibility of the web gap region can be increased through several alternatives, including the introduction of a slot at the edge of the connection plate, cropping the stiffener, and removing diaphragms. Adding connectivity to increase the stiffness of the connection is commonly implemented by welding or bolting angles to the flange. Performing this type of repair often requires removal of the concrete deck (Keating and Fisher, 1987; Fisher, 1990; Cousins and Stallings, 1998) to access the top flange. The drilling of crack-stop holes is the most commonly applied retrofit discussed in the literature, and can be used in combination with the retrofits listed previously.

Objective and scope

The main objective of this study was to investigate repair methods for distortion-induced fatigue cracks in the web gap region of bridge girders. The study included a suite of Finite Element (FE) analyses to investigate the effect of various retrofit measures and crack geometries on the stress distribution in the web gap region. The performance of two repair methods was investigated experimentally: 1) drilling of crack-stop holes and 2) providing connectivity by attaching angles to the connection plate and the girder web, and bolting the angles to a steel bar on the opposing side of the girder web (referred to as angles with plate repair).

Computer simulations

The computer models were created to resemble as closely as possible the girder-cross frame subassemblies that were tested (Fig. 2-2). Computer simulations of a full bridge with similar girder dimensions carried out for a different study (Hassel, 2011) showed good agreement between the stress fields computed at the web gap region of the model bridge and those computed for the specimens evaluated in this study. The dimensions of the specimens and the measured material properties are described in the experimental program section. Linear-elastic FE models were created using 8-node brick elements, each with 24 degrees of freedom. The number of elements ranged from 1 to 2 million, depending on the retrofit measure that was modeled. An 813-mm (32-in.) wide strip with a reduced mesh size was defined in the girder web, centered on the cross-frame connection plate, spanning from the bottom to the top flange. The size of the elements in this strip was set as 3 mm (0.10 in) to improve the accuracy of the calculated stress field in this region. A 76-mm (3-in.) wide vertical strip of tetrahedral elements

was used to transition from the fine mesh to a 10-mm (0.38-in.) coarser mesh used to model the web of the girder in locations away from the cross frame.
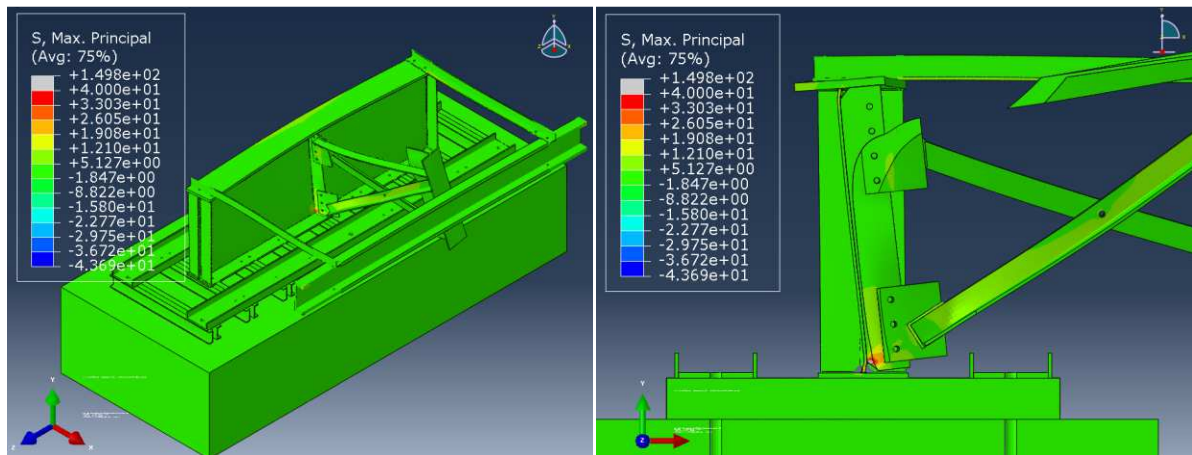
Figure 2-2: Deformed configuration of girder specimen: a) aerial view b) center cut

The connection plate was partitioned to allow for varying element types and mesh sizes around the bolt holes and the 32-mm (1.25-in.) clipped ends. A swept hexagonal mesh with 5-mm (0.19-in.) elements was used around the bolt holes and tetrahedral elements were used on the clipped ends. Everywhere else in the connection plate, 5-mm (0.2-in.) hexagonal elements were used. A similar meshing technique was used to model the end stiffeners. The hexagonal element size used away from the clipped edges was 8 mm (0.3 in.).

All four web-to flange fillet welds which were 5 mm (3/16 in.) were modeled with a triangular cross section using structured hexagonal elements. All five web-to-connection plate fillet welds were also modeled with a triangular cross section but in this case using tetrahedral elements. The fillet welds were placed all around the connection plate, including the top and the bottom. All welds had a maximum element size of 3 mm (0.1 in.). The modulus of elasticity of the A36 grade steel members was defined as 200 GPa (29,000 ksi) and Poisson's ratio was defined as 0.3.

The steel girder was connected to the reaction floor of the laboratory through a series of channels so that the flange would be restrained from out-of-plane motion in the same manner that the axial stiffness of the concrete deck restrains the out-of-plane motion of a girder in an actual bridge. The concrete floor was simulated in the computer model as an elastic material with a modulus of elasticity of 27,780 MPa (4,030 ksi) and Poisson's ratio equal to 0.2. The concrete mesh consisted of 102-mm (4-in.) brick elements with 16 nodes. Analyses were performed in which the tension force in the bolts was simulated explicitly, but it was found that the computed stress fields at the web gap region were very similar to those obtained with models in which the bolt force was neglected and the bolts were connected to the steel members with tie constraints, with the latter requiring a much lower computational cost. For the same reason, connections between the channels and the bottom flange of the girder were simulated using tie constraints.

The model was loaded with a single 22,240 N (5 kip) force, applied to a WT section that was used to connect the cross braces to the actuator. The bottom of the concrete block below the specimen was modeled as fully fixed, and so were both ends of a channel connecting the two end angles to the reaction frame (Fig. 2-3). The WT section connected to the actuator was restrained from moving along the direction parallel to the longitudinal axis of the girder. Figures 2-3 and 2-4 show the girder specimen and the experimental setup.

Figure 2-3: Experiment setup.
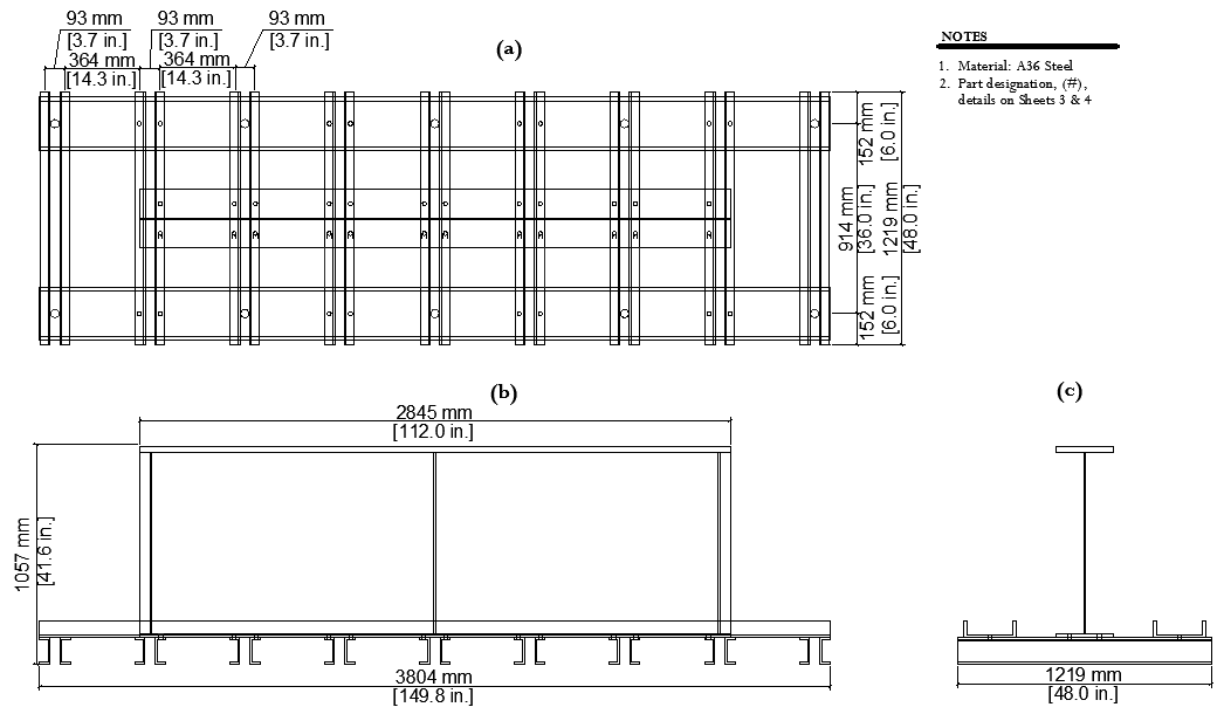
Figure 2-4: Girder specimen a) plan b) elevation c) section

Computed stresses from models with different retrofit measures were compared using the

hot spot stress (HSS) technique. The HSS technique was adopted to obtain a more reliable

measure of demand in areas of the web gap region where there were large stress gradients, such as near welded or bearing connections. Maximum principal stresses were used as a measure of vulnerability to fatigue damage because areas with the largest maximum principal stress demands in the model correlated well with locations were cracks formed in the specimens (Fig. 2-5).
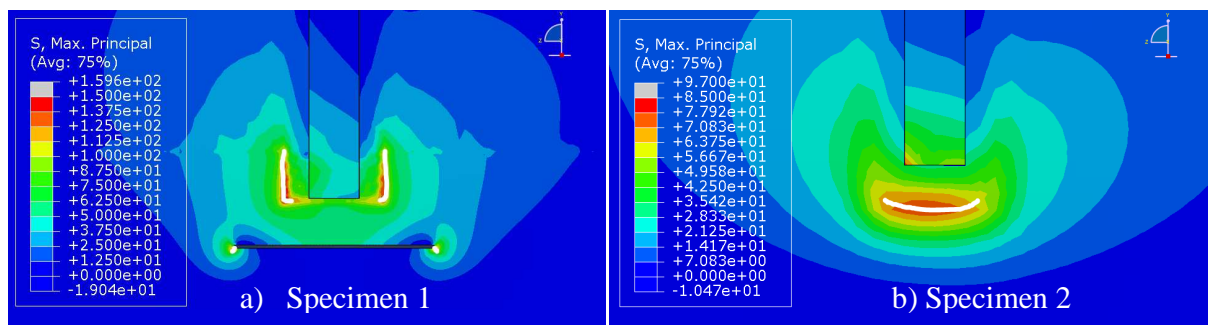
Figure 2-5: Observed crack patterns superimposed on the results from the simulation models for web gap regions of specimens 1 and 2.

In accordance with the definition of HSS used in this study, paths for sampling the stresses were defined at a distance of 5 mm (0.19 in.) away from the weld, equivalent to half the thickness of the web (10 mm, $^3/_8$ in.) (Fig. 2-6). HSS sampling paths were defined only at locations where cracks were observed in the specimens. HSS Path #1 Bottom was defined as a horseshoe-shaped path in the bottom web gap of the subassembly. HSS Path #2 Bottom was defined as a horizontal path above the crack that formed in the web-to-flange weld in the bottom web gap of the subassembly. Similar paths were defined and sampled in the top web gap of the subassembly when cracks were observed in the experiment. The J-Integral and stress intensity factors (SIF) at the tip of simulated cracks were computed as a measure of propensity for crack growth. A total of 5 contours were evaluated in the calculations, at points evenly spaced through the thickness of the web.
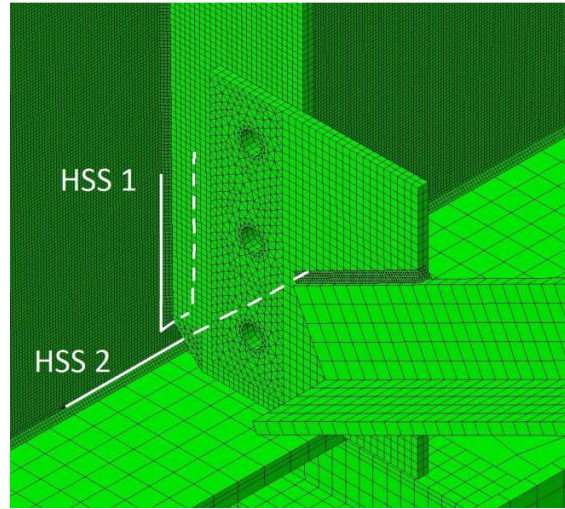
Figure 2-6: Pre-defined paths for sampling of stress demands in the various FE models.

Crack stop Holes

Crack-stop holes were placed in the FE models in the same locations that they were drilled

in the specimen. The location of the crack stop holes is shown in Figure 2-15. Holes were

placed at the tips of the 102-mm (4-in.) horseshoe crack and the 203-mm (8-in.) horizontal crack

in the bottom web gap of the subassembly. Holes were also drilled at the tips of the cracks in the

top web gap of the subassembly. The diameter of the holes was 19 mm (0.75 in.). Not all holes

shown in Fig. 2-7b are crack-stop holes. Four of the holes were used to attach angles to the web.

Figure 2-7 shows the computed stress fields with and without crack-stop holes. The comparison

shows that the stress demands were virtually the same.

The HSS sampling paths in the model with crack stop holes were defined at a distance of

half the thickness of the web away from the web-to-connection plate weld. Simulations were

performed to establish a comparison between an unretrofitted model with two cracks in the

bottom web gap region and a model with the same crack pattern but with crack-stop holes (Fig.

2-7). The maximum HSS value at Path#1 decreased by 27% with the drilling of the crack stop

holes, while the maximum HSS along Path #2 decreased by 16%. The stress fields presented in Fig. 2-7 show that the drilling of crack-stop holes did not significantly reduce the stress demand, and that the reduction was not likely sufficient to prevent the existing cracks from propagating.
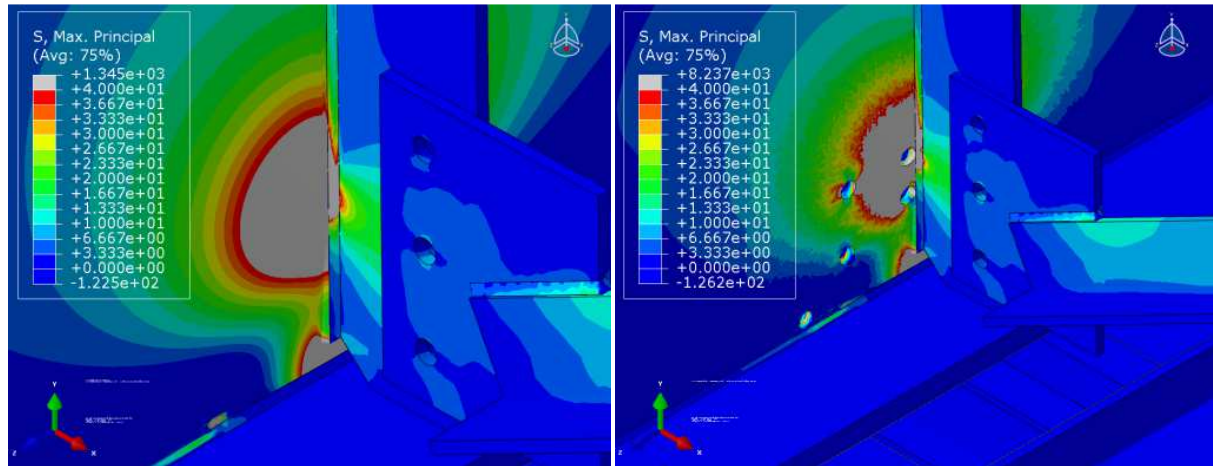
Figure 2-7: Stress field comparison a) No retrofit b) Crack stop hole retrofit

Angles-with-plate repair

This repair was developed based on experimental observations from simple three-point bending specimens with welded connections repaired with composite overlays. Test results showed that providing an alternate load path around the weld was a highly effective method to reduce the stress demand at the weld which led to a negligible rate of crack growth (Alemdar et al., 2011). Although the shape of the three-point bending specimens was different, there was a strong similarity in that computer and experimental simulations showed that horseshoe cracks originated near the weld between the connection plate and the web. Computer simulations in which the connection plate-to-web connection was repaired with composite materials were evaluated as part of this study, and this method proved to be highly effective. A simpler solution in terms of fabrication and installation in the field, which constitutes the focus of this study, was

17

also explored by using steel angles instead of composite blocks to reduce the stress demand at the welded connection.

The configuration of this retrofit measure is shown in Fig. 2-7a, Fig. 2-13 and Fig. 2-14. Parametric analyses of the angles-with-plate retrofit measure were performed to determine the optimal back plate and angle dimensions. The first parametric study involved varying the angle and back plate thicknesses, while the other dimensions were kept constant. The crack pattern in the model was the same used to evaluate the performance of the crack-stop hole retrofit, with a 102-mm (4-in.) tall horseshoe crack and a 203-mm (8-in.) horizontal crack in the bottom web gap of the subassembly. The horseshoe-shaped crack followed the toe of the CP-to-web fillet weld, while the horizontal crack was placed along the web-to-bottom flange weld. The back cover plate and angle thicknesses evaluated were 6 mm ($^1/_4$ in.), 13 mm ($^1/_2$ in.), and 25 mm (1 in.). Computed stress demands are summarized in Table 2-2. All values in Table 2-2 correspond to reductions in the calculated elastic stress demand with respect to the unretrofitted configuration ranging from 93 to 98%, which clearly shows that this retrofit significantly reduced the computed stress demand in the bottom web gap region. Although variations in the stress demands were found to be small, some trends can be discerned that are helpful in choosing an optimum configuration for the retrofit measure.

The stress demands in Table 2-2 show that for all back plate configurations, increasing the thickness of the angles led to a reduction in the peak stress demand at the path near the horseshoe crack. Increasing the stiffness of the back plate also led to a reduction in the peak stress at the path near the horseshoe crack. The effect of element stiffness on the peak stress demand at the path near the horizontal crack was the opposite. Increasing back plate and angle stiffness led to increases in stress demand, with the exception of the configuration with the most

18

flexible back plate, for which the stress demands were comparable for the stiff and flexible angle configurations. When the peak demand at the two paths is averaged, the configurations with the lowest stress demands are those with the thickest back plate (42 MPa, 6 ksi), with the lowest among those being the configuration with the thickest angles. Configurations with the highest average stress demand were those with the thinnest back plate (52 MPa, 7 ksi), with the highest among those being the configuration with the thinnest plate and the thinnest angles (62 MPa, 9 ksi). These results suggest that because the stiffness of the retrofit elements (angles and back plate) had a greater effect on the stress demand near the horseshoe crack than on the stress near the horizontal crack, stiffer configurations were most effective. However, it is noted that stiffer configurations resulted in slightly higher stress demands at the path near the horizontal crack. While stress demands near the horseshoe crack were inversely proportional to the stiffness of the retrofit elements, the relationship was much more complex for the case of the horizontal crack. In general, configurations with intermediate back plates had lower stress demands, with the lowest demand being obtained for a combination of intermediate angle and thinnest back plate.

In general, the parametric study showed that increasing the stiffness of the retrofit elements reduced the fraction of the connection force being transmitted through the connection plate (CP)-to-web fillet weld, which caused an increase in the stress demand at the web-to-flange weld. More flexible retrofit elements made the retrofit measure less effective for the crack at the CP-to-web and more effective for the crack at the web-to-flange weld. It is important to emphasize that although the stiffness of the angles and the plate did have an effect on the calculated stress demand, this effect was relatively small, and in all instances the calculated stress demands were much lower than the values computed for the unretrofitted configuration.

A second parametric study was performed in which the angle and back plate thickness were kept constant at 13 mm ($^1/_2$ in.), while the length of the back plate was changed. The length of the back plate was set to 305, 457, 610, and 914 mm (12, 18, 24, and 36 in.). The results are also summarized in Table 2-2. Again the results were contradictory in terms of the effect of the retrofit measure on the stress demand near the two cracks. While increasing the length of the back plate had the effect of reducing the peak stress demand near the CP-to-web weld, it increased the peak stress demand at the web-to-flange weld. Of the two critical locations, the length of the back plate had the largest effect on the stress demand near the web-to-flange weld. If the average peak stress is used as a measure of demand, configurations with 305- and 457-mm (12- and 18-in.) plate lengths had the lowest demands, with very similar averages of 54 MPa and 53 MPa (8 and 7 ksi), respectively.

Table 2-1: Maximum HSS for retrofitted model with 2 cracks in the bottom web-gap region. Parametric studies 1 and 2.

Designation	Plate Length, mm (in)	Plate Thickness, mm (in)	Angle Thickness, mm (in)	HSS Path #1 Bottom, MPa (ksi)	HSS Path #2 Bottom, MPa (ksi)
*s*A-*s*BP18	457 (18)	25 (1)	25 (1)	23 (3.4)	58 (8.3)
*m*A-*s*BP18	457 (18)	25 (1)	13 ($^1/_2$)	30 (4.3)	55 (8.0)
*f*A-*s*BP18	457 (18)	25 (1)	6 ($^1/_4$)	30 (4.4)	54 (7.9)
*s*A-*m*BP18	457 (18)	13 ($^1/_2$)	25 (1)	39 (5.6)	55 (7.9)
*m*A-*m*BP18	457 (18)	13 ($^1/_2$)	13 ($^1/_2$)	60 (8.6)	45 (6.5)
*f*A-*m*BP18	457 (18)	13 ($^1/_2$)	6 ($^1/_4$)	51 (7.4)	47 (6.9)
*s*A-*f*BP18	457 (18)	6 ($^1/_4$)	25 (1)	41 (5.9)	52 (7.6)
*m*A-*f*BP18	457 (18)	6 ($^1/_4$)	13 ($^1/_2$)	51 (7.3)	43 (6.2)
*f*A-*f*BP18	457 (18)	6 ($^1/_4$)	6 ($^1/_4$)	68 (9.8)	55 (8.0)
*m*A-*m*BP12	305 (12)	13 ($^1/_2$)	13 ($^1/_2$)	59 (8.5)	49 (7.1)
*m*A-*m*BP18	457 (18)	13 ($^1/_2$)	13 ($^1/_2$)	60 (8.6)	45 (6.5)
*m*A-*m*BP24	610 (24)	13 ($^1/_2$)	13 ($^1/_2$)	56 (8.2)	74 (10.7)
*m*A-*m*BP36	914 (36)	13 ($^1/_2$)	13 ($^1/_2$)	45 (6.5)	77 (11.2)

A third parametric study was conducted to evaluate the effect of crack length on the likelihood of fatigue damage for the angles-with-plate retrofit measure. Hot spot stress (HSS) values were extracted from analyses of models with varying lengths of the horseshoe-shaped and horizontal cracks. Configurations evaluated had horseshoe-shaped and horizontal crack lengths of 0.5 and 0.5 in., 1 and 1 in., and 4 and 8 in., respectively. The last crack configuration, with lengths of 4 and 8 in., corresponded to the observed crack configuration at the end of the first trial for specimen 2 (Table 2-3, Fig. 2-13a), and was the same crack configuration used in the first and second parametric studies. All models had the angles-with-plate retrofit measure implemented with angle and cover plate thicknesses of 6 mm ($^1/_4$ in.), 13 mm ($^1/_2$ in.), and 25 mm (1 in.) evaluated for each crack configuration. In all the models of the third parametric study the length of the back plate was 457 mm (18 in.). Companion models with the angle-with-plates retrofit measure but without cracks were also analyzed to provide a basis for comparison.

The peak HSS exhibited different trends with respect to crack length along Path #1 (horseshoe-shaped crack) than it did along Path #2 (horizontal crack). For HSS Path #1 (horseshoe-shaped crack) configurations with the thickest angles and/or back plate (stiff configurations, Fig. 2-9a) the maximum stress demand corresponded to the retrofitted specimen without cracks (shown in the graphs in Fig. 2-9 as zero length). The peak HSS decreased with increasing crack length, stabilizing at approximately 75% of the peak demand computed with the unretrofitted model. The crack length at which the peak stress demand stabilized was lowest for the model with the stiffest angles. For the configuration with the thinnest angles (flexible configuration, Fig 9b) and back plate the HSS values decreased with crack length for very short lengths, approximately less than 12 mm (0.5 in.). For crack lengths longer than 12 mm (0.5 in.) the peak stress demand increased with crack length for the configurations with the two thinnest

angles. These results showed that the best alternative to reduce the stress demand near the horseshoe-shaped crack was to use the stiffest angle and backplate combination, and that the effectiveness of the retrofit measure was nearly independent of crack length.

Table 2-2: Maximum HSS for retrofitted model in the bottom web-gap region. Parametric study 3.

Designation	Plate Thickness, mm (in.)	Angle Thickness, mm (in.)	HSS Path #1 MPa (ksi)		HSS Path #2 MPa (ksi)		
sA-sBP18	25.4 (1)	25.4 (1)	60.0 (8.7)		102.0 (14.8)		No Cracks
mA-sBP18	25.4 (1)	12.7 (0.5)	65.0	9.4	103.9	15.1	
fA-sBP18	25.4 (1)	6.35 (0.25)	67.8	9.8	103.0	14.9	
sA-mBP18	12.7 (0.5)	25.4 (1)	73.1	10.6	106.2	15.4	
mA-mBP18	12.7 (0.5)	12.7 (0.5)	86.2	12.5	111.1	16.1	
fA-mBP18	12.7 (0.5)	6.35 (0.25)	95.5	13.9	110.5	16.0	
sA-fBP18	6.35 (0.25)	25.4 (1)	81.7	11.8	107.4	15.6	
mA-fBP18	6.35 (0.25)	12.7 (0.5)	99.7	14.5	114.4	16.6	
fA-fBP18	6.35 (0.25)	6.35 (0.25)	115.8	16.8	127.0	18.4	
sA-sBP18	25.4 (1)	25.4 (1)	48.7	7.1	115.0	16.7	0.5-in. horseshoe crack 0.5-in. horizontal crack
mA-sBP18	25.4 (1)	12.7 (0.5)	54.5	7.9	117.6	17.1	
fA-sBP18	25.4 (1)	6.35 (0.25)	66.7	9.7	116.8	16.9	
sA-mBP18	12.7 (0.5)	25.4 (1)	58.0	8.4	116.5	16.9	
mA-mBP18	12.7 (0.5)	12.7 (0.5)	68.8	10.0	123.6	17.9	
fA-mBP18	12.7 (0.5)	6.35 (0.25)	94.6	13.7	124.4	18.0	
sA-fBP18	6.35 (0.25)	25.4 (1)	60.2	8.7	115.6	16.8	
mA-fBP18	6.35 (0.25)	12.7 (0.5)	72.2	10.5	125.6	18.2	
fA-fBP18	6.35 (0.25)	6.35 (0.25)	94.2	13.7	138.1	20.0	
sA-sBP18	25.4 (1)	25.4 (1)	42.8	6.2	127.2	18.5	1.0-in. horseshoe crack 1.0-in. horizontal crack
mA-sBP18	25.4 (1)	12.7 (0.5)	48.8	7.1	129.5	18.8	
fA-sBP18	25.4 (1)	6.35 (0.25)	59.1	8.6	127.5	18.5	
sA-mBP18	12.7 (0.5)	25.4 (1)	53.1	7.7	128.5	18.6	
mA-mBP18	12.7 (0.5)	12.7 (0.5)	67.0	9.7	135.0	19.6	
fA-mBP18	12.7 (0.5)	6.35 (0.25)	82.6	12.0	133.4	19.3	
sA-fBP18	6.35 (0.25)	25.4 (1)	57.8	8.4	126.4	18.3	
mA-fBP18	6.35 (0.25)	12.7 (0.5)	71.1	10.3	134.9	19.6	
fA-fBP18	6.35 (0.25)	6.35 (0.25)	91.4	13.3	137.7	20.0	
sA-sBP18	25.4 (1)	25.4 (1)	38.0	5.5	60.7	8.8	4.0-in. horseshoe crack 8.0-in. horizontal crack
mA-sBP18	25.4 (1)	12.7 (0.5)	48.3	7.0	54.2	7.9	
fA-sBP18	25.4 (1)	6.35 (0.25)	49.2	7.1	52.2	7.6	
sA-mBP18	12.7 (0.5)	25.4 (1)	56.4	8.2	53.5	7.8	
mA-mBP18	12.7 (0.5)	12.7 (0.5)	76.1	11.0	64.4	9.3	
fA-mBP18	12.7 (0.5)	6.35 (0.25)	96.6	14.0	91.0	13.2	
sA-fBP18	6.35 (0.25)	25.4 (1)	53.7	7.8	50.2	7.3	
mA-fBP18	6.35 (0.25)	12.7 (0.5)	77.2	11.2	69.5	10.1	
fA-fBP18	6.35 (0.25)	6.35 (0.25)	119.7	17.4	109.2	15.8	

For HSS Path #2 (horizontal crack near the web-to-flange weld), all combinations of angle and plate thicknesses followed a trend different from that observed for HSS Path #1. For short crack lengths, between 0 and 25 mm (1 in.), the peak stress demand increased with crack length. For crack lengths larger than that, peak HSS values decreased with increasing crack length, with the magnitude of the decaying slope being a function of the stiffness of the retrofit components. For retrofit configurations with the thickest back plate or the thickest angle (Fig. 2-7a), the reduction in stress demand with respect to crack length was nearly the same regardless of the stiffness of the other retrofit component. For retrofit configurations with the thinnest back plate or angle (Fig. 2-7b) the effect of the stiffness of the other retrofit component was very significant. The HSS values tended to diverge for very long cracks with the stress demands being significantly highest for the configuration with the thinnest angles and plate.

Similar trends were observed for computed J-Integral values from contours surrounding the tip of the horizontal crack, at the tension face of the web (Fig. 2-7c). Calculated J-Integral values for retrofitted models with 0.5-in. cracks fell between those calculated for models with 1- and 8-in. cracks, with the highest value corresponding to the models with 1-in. cracks. This trend was similar to that observed in Fig. 2-7a and 7b for the HSS, and suggests that the potential for crack growth increased with crack length for relatively short cracks (less than 25 mm or 0.5 in. long). For longer cracks, the computed J-Integral values suggest that the potential for crack growth decreased with increasing crack length, and was lowest for the configuration with the longest crack and thinnest angles and plate. This was an important finding considering that the angles-with-plate retrofit measure does not provide any direct connectivity between the connection plate (CP) and the flange. The main driving force for the horizontal crack (HSS Path

24

#2) is induced by bending stresses in the vertical direction that are caused by the distortion of the web gap region. The addition of the angles and back plate in the web gap region drastically reduces the distortion and consequently the distortion-induced stresses in the vertical direction of the web gap. The stiffness of the back plate results in a more uniform distribution of stresses over a much larger region, which causes a drastic reduction in the driving force in the horizontal crack.

The results from the parametric study show that the effectiveness of the angles-with-plate retrofit measure quantified in terms of the HSS and the J-Integral was not very sensitive to crack length. Of the two types of crack studied, the effectiveness of the retrofit measure was most sensitive to crack length for the horizontal crack near the web-to-flange weld. These results indicate that this type of repair should be equally effective for cracks with various lengths, and that the most effective configurations are likely to be those with very stiff elements.
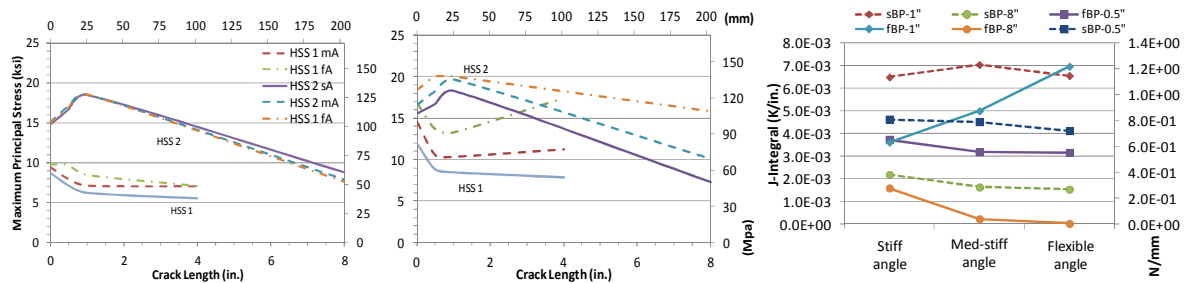
Figure 2-8: Peak demand at web gap region vs. crack length for retrofitted specimens a) HSS for stiff back plate configurations b) HSS for flexible back plate configurations, c) J-Integral for various back plate configurations.
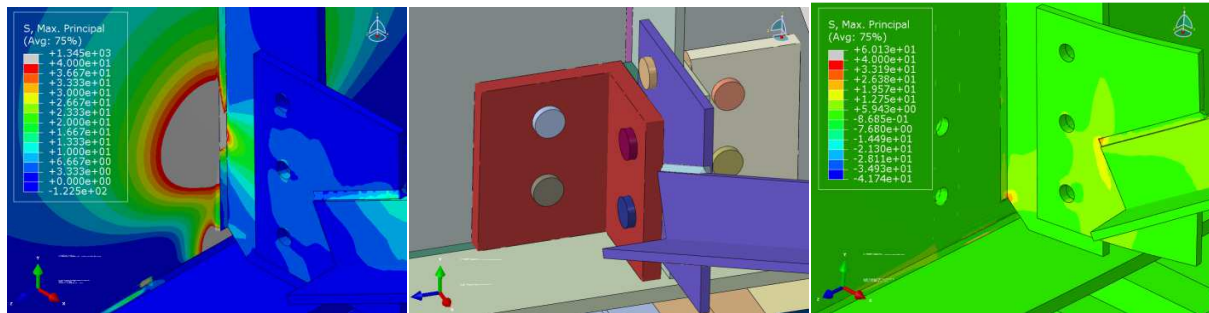
Figure 2-9: a) computed stresses without retrofit b) angle retrofit configuration c) computed stresses with retrofit.

Experimental program

The goal of the experimental study was to confirm the findings of the finite element simulations by evaluating the fatigue-crack propagation life of steel girders repaired using two different retrofit measures. The two retrofits evaluated experimentally in this study were crack stop holes, and the angles-with-plate repair.

In the web gap region of an existing bridge, the top flange of a girder is restrained from lateral motion by the bridge deck, while the bottom flange is free or nearly free to move in the out-of-plane direction. In the laboratory, it is difficult to replicate the same boundary conditions that exist in a bridge when performing a component test. The subassemblies evaluated in this study were placed upside down (Fig. 2-3) meaning that the unrestrained flange was at the top of the subassembly. One of the effects of attaching the specimen to the reaction floor in this manner is that the bending stresses are eliminated from the girder web, leaving only the out-of-plane demands imposed by the cross-frame. Consequently, the stress field imposed on the specimens was more representative of the behavior expected near inflection points of bridges. An experimental investigation with the combined effects of bending and out-of-plane stresses using full bridge specimens is the subject of a companion study.

The web gap region of the girder subassembly was loaded under a constant stress range while the propagation of fatigue cracks was monitored. Given the characteristics of the stress field at the web-gap region, experimental results provided insight about crack propagation behavior under the combined effects of fracture modes 1 and 3 (opening and shear). The experimental results also allowed for direct comparisons between the two repair methods.

Specimen Dimensions

The girder subassemblies were built-up I shape sections with a height of 918 mm (36.13 in.). The thickness of the web was 10 mm ($^3/_8$ in.) and web height was 876 mm (34.5 in.). The top and bottom flanges had a width of 279 mm (11 in.), and thicknesses were 25 mm (1.0 in.) and 16 mm (0.63 in.), respectively. The connection stiffener (CS) in the middle of the girder was attached to the web with a 5-mm (3/16 in.) weld. The CS had a thickness of 10 mm ($^3/_8$ in.), a width of 127 mm (5 in.), and a height of 873 mm (34.4 in.). The CS had a cropped end of 32 mm (1-$^1/_4$ in.). There was a 3-mm (1/8 in.) gap between the CS and bottom flange. At the top of the girder, the CS was bearing against the inside face of the top flange, without any welded connection. At each end of the girder, on both sides of the web, stiffeners were welded to the web and both flanges. The stiffener dimensions at the ends of the girder were 10x876x127 mm ($^3/_8$ x 34-½ x 5 in.). The girder subassembly was attached to the laboratory floor with C5x9 channels (Fig. 2-3). The channels were connected to the girder through fully-tightened 19-mm ($^3/_4$-in.) diameter A325 structural bolts. The bottom flange was connected to the channels with bolts at a spacing of 1 ft. A cross-frame connected the specimen to the actuator. The cross-frame consisted of three L76x76x10-mm (L3x3x$^3/_8$-in.) angles, with an X-shape configuration and a horizontal member. The cross frame was connected to a WT section used to stabilize the

free end of the cross frame and to prevent warping and bending of the frame while loading the specimen.

Material properties

All the plates used to fabricate the built-up section were grade A36 steel. Coupons were taken from the web, flange and stiffeners after the test was concluded, and measured yield strengths will be summarized in the table.

Instrumentation

The specimens were instrumented with linear variable differential transformers (LVDTs) and with strain gages, in locations shown in Figure 2-10. Two strain gages were located behind the connection plate at the top and bottom of the web (Gages 5-7). Another two were located on the right side of the connection plate (Gages 4-6) (Fig. 2-10). The stress range was defined on the basis of the readings from strain gage 4, located 17 mm (0.65 in.) to the right of the CS. This location was selected because the computer simulations showed that the stress field was nearly constant in this region and the stress was considered to be representative of the bending stress induced by the out-of-plane motion in the web gap. The measured stress range under the applied load recorded by gage 4 was 196 MPa (28.5 ksi).

The LVDTs were placed to measure the out-of-plane deflections at three different locations on the center line of the girder. The first LVDT was placed at the top flange, the second at the midsection of the web, and the third directly behind the bottom end of the CS. Good agreement was found between the deflected shapes computed in the simulations and the experimental measurements (Fig. 2-11). As shown in Fig. 2-11, the computed deflections for the nominal force range were lower in magnitude than those measured, but when scaled to match the

measured deflection range at the top of the girder the slope of the deflected shape at the center of

the girder matched the measured deflected shape very closely.
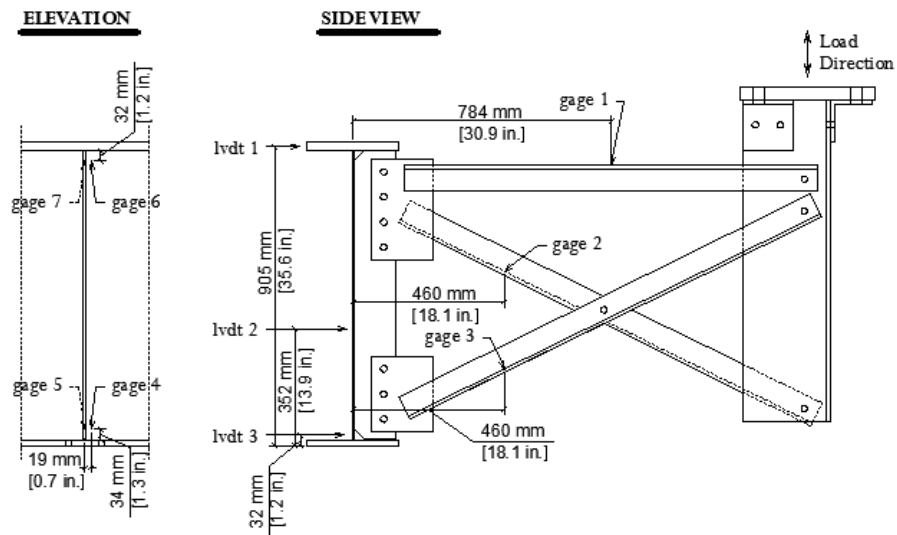
Figure 2-10: Instrumentations on 9-ft girder specimen.
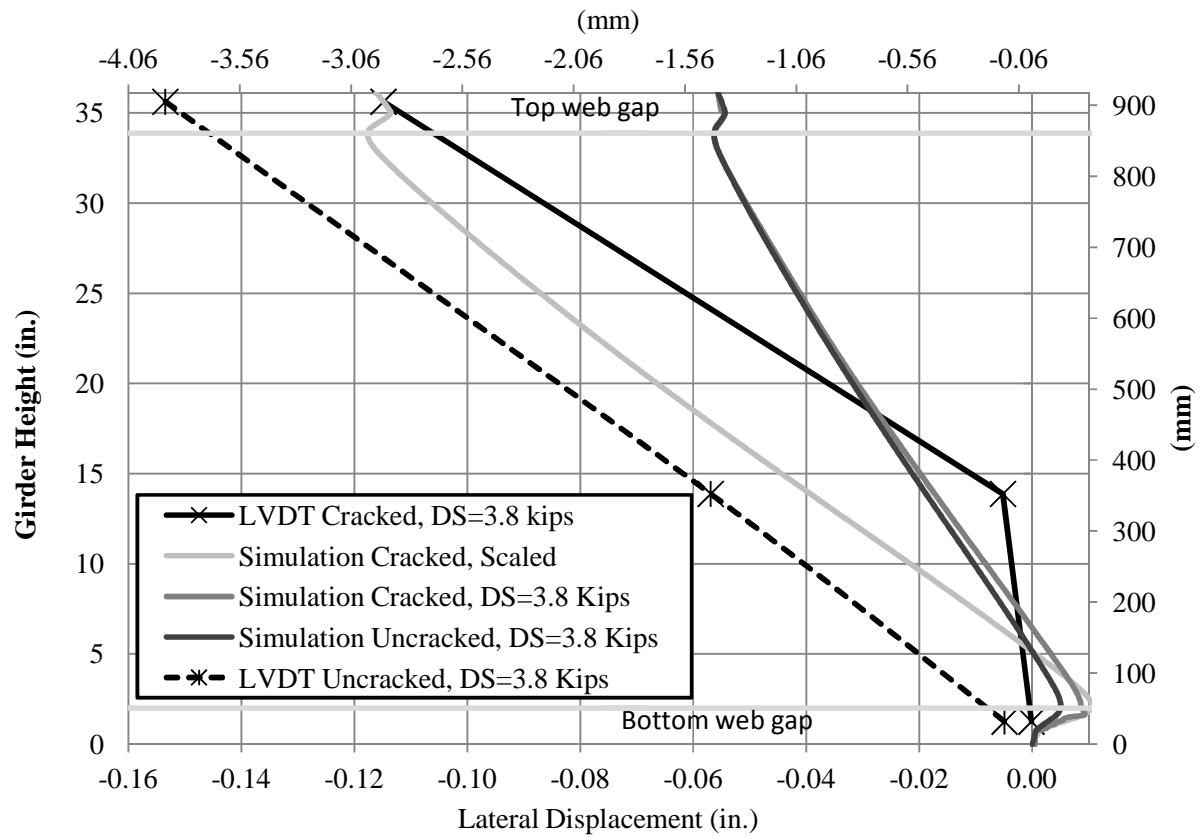
Figure 2-11: Comparison between LVDT readings and computed deformations

Gages Reading Comparison with Simulation Model

Figure 2-12 shows a comparison between strain gage readings and simulation results. The computed strains shown in the figure represent average values over the area occupied by the gages. The gage readings were slightly higher than the simulation values, which is consistent with the results for the deflected shapes.
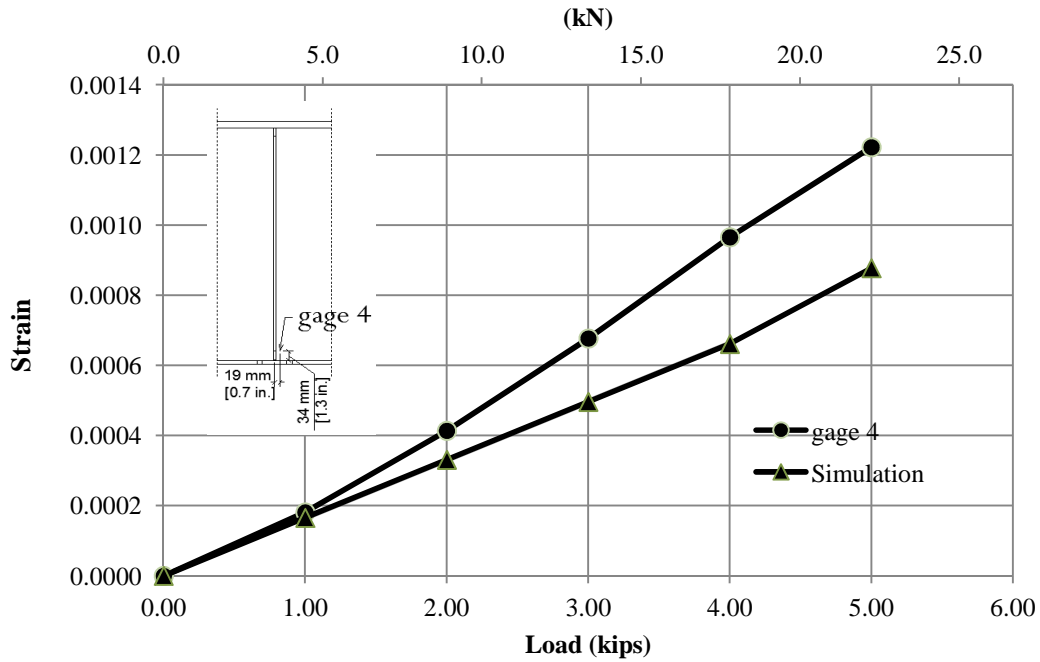
Figure 2-12: Strain gage readings compared with simulation model results.

Test Procedure

Specimens were subjected to cyclic loading in distortion induced fatigue. The maximum

load applied was 20 kN (4.6 kip) and the minimum was 3.6 kN (0.8 kip). The tests were

performed using two different actuators, and the frequency of loading was limited by the

capacity of the servovalve of the hydraulic actuator that was employed. The two loading rates

were 0.5 and 2 Hz. Crack growth was monitored periodically. Tests were stopped when a large

crack size was reached or when repaired specimens were considered to have exceeded the

equivalent of infinite fatigue life without a measurable increase in the size of the fatigue cracks

(Fig. 2-16). In this study infinite fatigue life of a repaired specimen was defined as the number

of cycles in the S-N curve of the AASHTO LRFD Bridge Design Specification (AASHTO,

2007) corresponding to a Category A detail (approximately 1.2 million cycles) for the experimentally measured stress range 197 MPa, (28.5 ksi).

The experimental program is summarized in Table 2-3. Two specimens were evaluated with several test trials per specimen. Specimen 1 had a pre-drilled horizontal crack with a length of 38 mm (1.5 in.) at a distance of 17 mm (0.65 in) from the top of the bottom flange. Specimen 1 was subjected to cyclic loading to monitor the crack progression.

Table 2-3: Experimental Program

Specimen	Test Trial	Configuration
1	1	Pre-Cracked, Unretrofitted
2	1	Un-cracked, Unretrofitted
2	2	Cracked, Angles with Plate Retrofit Bottom Web Gap
2	3	Cracked, Angles with Plate Retrofit Bottom and Top Web Gap
2	4	Cracked, Crack-Stop Hole Retrofit

Specimen 2 was first tested in the uncracked configuration. The first trial consisted of loading the specimen while periodically monitoring the crack progression without any type of retrofit measure. After significant damage had been sustained, a second test trial was conducted in which the angles with plate retrofit measure was applied to the bottom web gap while monitoring crack growth periodically. During trial 2 for Specimen 2, a crack was observed at the top web gap. A third test trial was conducted in which the specimen was repaired with the angles with retrofit repair at the top and bottom web gaps. A fourth trial was conducted in Specimen 2 in which crack-stop holes were drilled and the angles with plate repair was removed to determine the number of cycles to crack re-initiation under the same loading range.

Retrofit Measures

As indicated, two different retrofit measures were evaluated experimentally. The first was the angles-with-plate retrofit, and the second consisted of drilling crack-stop holes at the tips of the cracks, a retrofit measure that is widely employed in steel bridges.

Angles with Plate Retrofit Measure

The angles with plate retrofit measure was devised with the intention of reducing the stress demand at the welded connection between the Connection Plate (CP) and the web of the girder, preventing further growth of horseshoe-shaped cracks around the CP. The back plate was added with the goal of distributing the out-of-plane force transferred by the cross frame over a larger area of the web, reducing the stress demand at the connection between the web and the flange of the girder, preventing further growth of the horizontal crack commonly found at that location.

The angle and cover plate dimensions evaluated experimentally were L152x152x19-mm (L6x6x$^3/_4$-in.) and 457x457x19-mm (18x8x$^3/_4$-in.), respectively (Fig. 2-11). Angles were connected to the web and the connection plate with two bolts on each leg (Fig. 2-12). A 10-mm ($^3/_8$-in.) thick shim plate was placed between the CP and the angle to prevent any chamfering or grinding of the edge of the angles. The angles and the back plate were removed every 250,000 cycles to inspect the web gap region and measure crack growth.
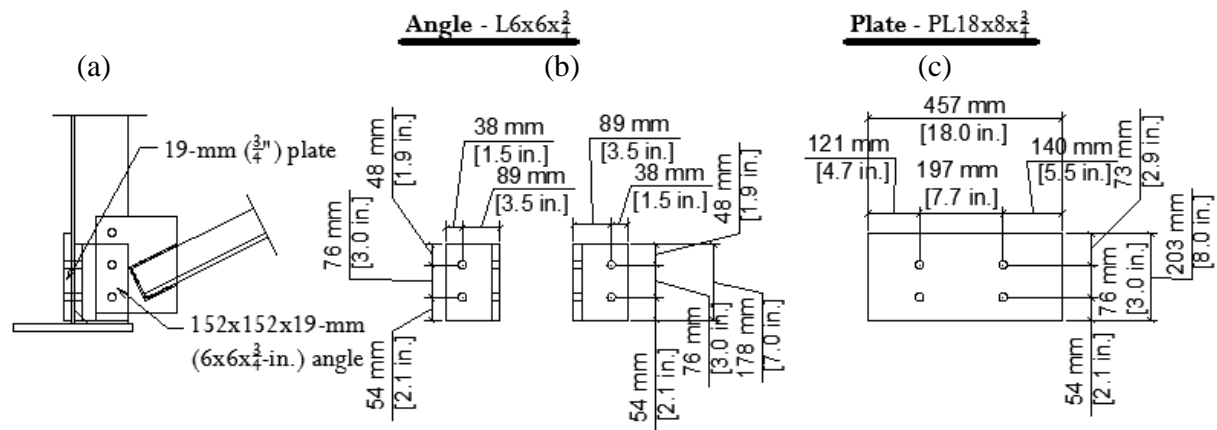
Figure 2-13: Dimensions of angles and plate evaluated experimentally. a) side view, b) angle dimensions, c) plate dimension

Figure 2-14: Angle retrofit with plate a) back plate, b) angles

Crack Stop Holes

Crack stop holes were selected to have a diameter of 21 mm ($^{13}/_{16}$ in.), similar to the hole size used for the angles with retrofit repair. This diameter was chosen given the severe level of damage at the web-gap region when the holes were drilled. Drilling holes with the same diameter as those commonly drilled in bridge girders under the circumstances would have resulted in excessive weakening of the web gap region. Furthermore, there are many situations in which the constraints imposed by the geometry of the web-cross frame connection or the

location of the cracks present a similar problem to engineers in charge of repairing fatigue damage.

The crack-stop holes were drilled so that the edge of the hole would coincide with the corresponding crack tip. When two cracks were found closely located to each other a single crack stop hole was drilled to encompass both crack tips. Crack stop holes were not drilled at cracks that had stabilized in the unretrofited configuration. The hole placement in the bottom and top web gaps of specimen 2 are shown in Fig. 2-15. As shown in Fig. 2-15 some cracks intersected others; for example, horizontal cracks on the front and back of the web. In that case, crack stop holes were placed on the longer cracks and the smaller diameter holes were drilled at the tips of the shorter cracks. The smaller holes had a diameter of 6 mm ($^{1}/_{4}$ in.). The diameter of the crack stop holes was 21 mm ($^{13}/_{16}$ in.) and they were drilled using a hole saw with guide.
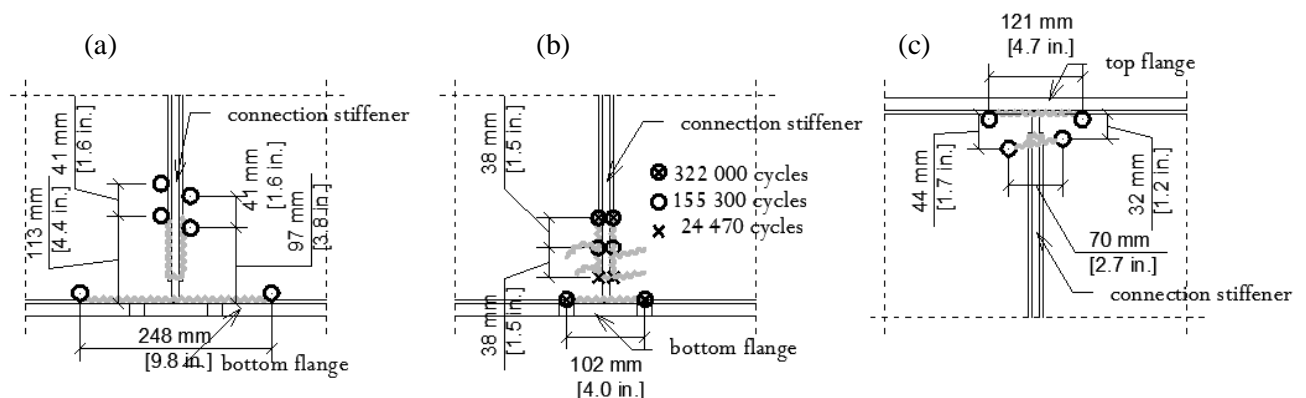
Figure 2-15: a) Crack stop holes in bottom web-gap region specimen 2, b) Crack progression at the bottom web gap region of specimen 2, un-retrofitted, c) Crack stop holes at the top web gap region

Experimental results

As described in the experimental program section a total of five test trials were performed on the beam subassemblies. Crack progression for the various test trial is summarized Table 2-3.

Prior to loading Specimen 1 a 38-mm (1.5-in.) horizontal crack was pre-cut in the web gap region, between the edge of the connection plate and the flange weld. The main purpose of the trial conducted with this specimen was to explore the evolution of the crack propagation pattern and to provide data for calibrating the FE models. Test trial 1 was concluded after 740,000 cycles, and no retrofit measures were evaluated in this specimen. The crack pattern, shown in Fig. 2-5a, was similar to that found in Specimen 2. A fatigue crack developed at the toe of the CP-to-web fillet weld, similar to the crack that developed at the fillet weld of Specimen 2 (Fig. 2-5b, and 2-13b). Consistent with the results from the FE simulation (Fig. 2-5a), the ends of the pre-cut horizontal crack grew towards the bottom flange.

Five different test trials were conducted using Specimen 2. The first trial was without any retrofit or pre-existing crack, and crack growth was monitored for a total of 490,000 cycles. The crack progression is illustrated in Fig. 2-15b. As shown, the first crack in the specimen was noted at 22,700 cycles, located at the toe of the weld in the bottom web gap region. Cracks continued to grow as shown in Fig. 2-15b with a second crack developing at the web-to-flange connection, in the horizontal direction. At the conclusion of the first trial the specimen had the crack pattern shown in Fig. 2-15b with a few secondary cracks radiating from the CP-to-web weld in the horizontal direction. At 490,000 cycles the main crack along the CP-to-web weld had a length of approximately 101 mm (4 in.) in the vertical direction, while the horizontal crack along the web-to-flange connection had a length of 203 mm (8 in.).

The remaining trials conducted with the second specimen were carried out to evaluate the performance of retrofit measures. During the second trial, which extended for a total of 1,225,860 cycles, two angles and a cover plate were used to reinforce the bottom web gap region. During this trial two new cracks initiated in the top web gap region. At the end of the trial, an

83-mm (3.25-in.) long horizontal crack had formed at the top web gap, following the tip of the flange-to-web weld, and a 29-mm (1.13-in.) vertical crack had propagated down from the top of the connection plate-to-web weld.

During the third trial, angles and a connection plate were attached to the top web gap region. The specimen underwent a total of 1,250,740 cycles in this configuration. At the end of the third trial the cracks in the bottom web gap exhibited no additional crack growth, but the horizontal crack at the top web gap region extended an additional 25 mm (1 in.) and the vertical crack gave rise to a secondary crack behind the stiffener. The orientation of the secondary crack was almost horizontal and the length at the end of the trial was approximately 51 mm (2 in.).

A fourth trial was carried out to evaluate the performance of crack-stop holes compared with that of the "angles and plate" repair. A total of 10 holes with a diameter of 19 mm ($^3/_4$ in.) and 4 holes with a diameter of 6 mm ($^1/_4$ -in.) were drilled. At the end of this test trial, which lasted a total of 39,720 cycles, the bottom horseshoe crack to had grown an additional 70 mm (2.75 in.) and the bottom horizontal crack to extend an additional 13 mm (0.50 in.). Experimental results from the various test trials are compared on the basis of the AASTHO S-N Curve in Figure 2-16.

AASHTO S-N Curve for 9-ft Specimen
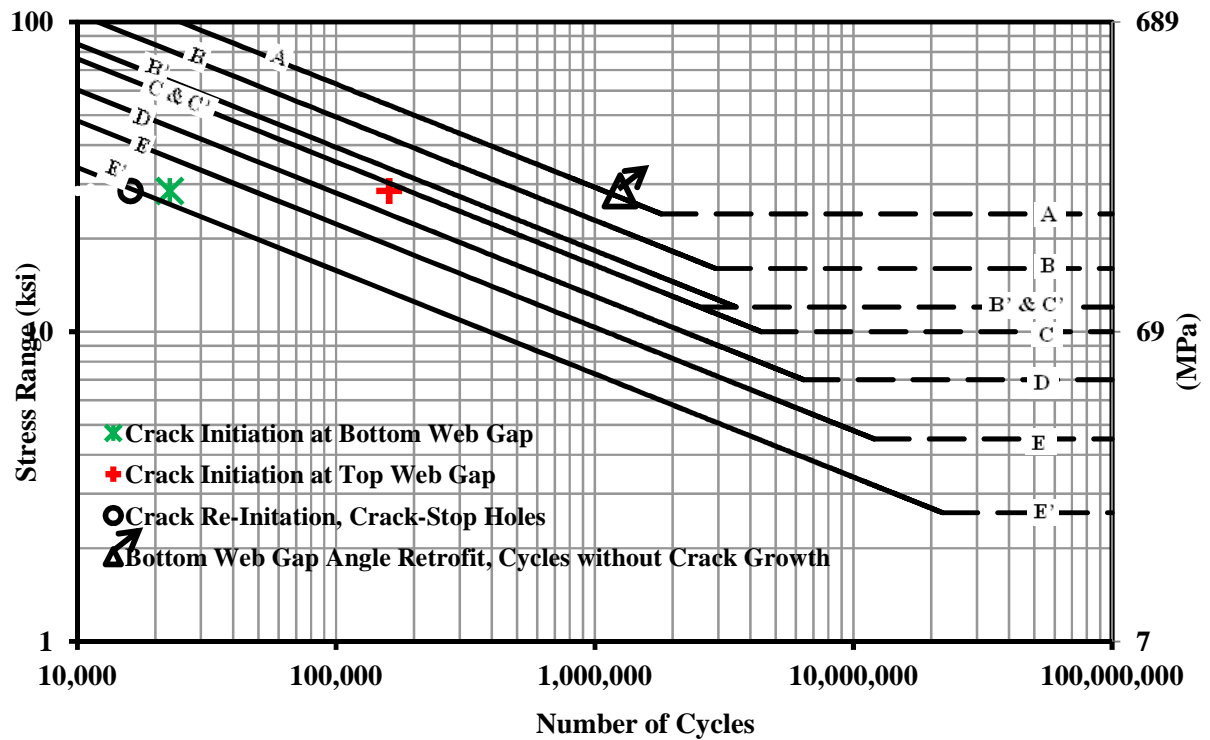
Figure 2-16: Experimental results for specimen 2 trials.

Table 2-4: Crack growth

Specimen / Trial	Retrofit Measure / Observation	Number of Cycles	Crack Location and growth, mm (in.)			
			Bottom Horizontal	*Bottom Horseshoe*	*Top Horizontal*	*Top Horseshoe*
1/1	*No retrofit / Crack initiation*	250,000	0 (0)	6 (0.3)	0 (0)	0 (0)
1/1	*No Retrofit / Crack growth*	740,000	6 (0.3)	25 (1)	0 (0)	0 (0)
2/1	*No Retrofit / Crack initiation*	24,460	0 (0)	6 (0.3)	0 (0)	0 (0)
2/1	*No Retrofit / Crack growth*	490,460	203 (8)	127 (5)	0 (0)	0 (0)
2/4	*Crack Stop Holes / Crack growth*	39,720	13 (0.5)	70 (2.8)	0 (0)	0 (0)
2/2	*Angles Bottom / Crack growth*	1,225,860	0 (0)	0 (0)	57 (2.3)	25 (1)
2/3	*Angles Bottom & Top / Crack growth*	1,250,740	0 (0)	0 (0)	25 (1)	0 (0)
2/5	*Angles Bottom & Top / Crack growth*	1,238,300	0 (0)	0 (0)	0 (0)	0 (0)

Conclusions

The research study conducted showed that the angles-with-plate repair was a very effective method to reduce the fatigue crack propagation rate in beams damaged by distortion-induced fatigue. Computer simulations of girder subassemblies tested under fatigue loading showed that areas in the web gap region of the model exhibiting the highest maximum principal stress demands correlated closely with the locations of fatigue cracks observed in the experiments. Both computer simulations and girder tests showed that there were two primary cracks that formed in the web gap region: a horseshoe-shaped crack along the toe of the weld between the CP and the girder web, and a horizontal crack along the toe of the weld between the web and the flange of the girder. The performance of two different retrofit measures intended to arrest the growth of these two fatigue cracks was evaluated experimentally.

The angles-with-plate retrofit measure was effective in preventing the distortion of the web gap region, drastically reducing the stress demands calculated at the critical points. Finite element simulations showed that stress demands at the critical points of the web gap region reinforced with the angles-with-plate repair were on the order of 5% of those in the unreinforced configuration. The manner in which fatigue cracks propagated during experimental simulations of beam subassemblies was consistent with the results from the computer simulations. Beams in which the angle-with-plates retrofit measure was implemented experienced negligible crack growth under the same load range that caused severe fatigue damages to the web gap region of unretrofitted specimens.

Crack-stop holes were effective in removing the sharp crack tips, preventing crack growth in the specimens by the number of cycles corresponding to fatigue crack initiation. Because crack stop holes had a negligible effect on the stress demand, and given the relatively

small size of the holes evaluated, the number of cycles to crack reinitiation was comparable to the number of cycles to fatigue crack initiation in the unretrofited configuration, and an order of magnitude lower than the number of cycles imposed on the retrofitted specimens without any measurable crack growth.

The angles-with-plate retrofit measure developed was shown to be very effective, simple, economical, and does not require any field welding, which constitutes a great advantage in terms of the reliability of the retrofit measure.

References

AASHTO, (2007). "AASHTO LRFD Bridge Design Specifications (2007)." American Association of State Highway and Transportation Officials.

Alemdar, F., A. Matamoros, C. Bennett, R. Barrett Gonzalez, and S.T. Rolfe. 2011. Use of CFRP Overlays to Strengthen Welded Connections under Fatigue Loading. *Journal of Bridge Engineering* 1:191.

Castiglioni, CA, JW Fisher, and BT Yen. 1988. Evaluation of fatigue cracking at cross diaphragms of a multigirder steel bridge. *Journal of Constructional Steel Research* 9 (2):95-110.

Cousins, TE, and JM Stallings. 1998. Laboratory Tests of Bolted Diaphragm-Girder Connections. *Journal of Bridge Engineering* 3:56.

Fisher, JW. 1990. *Distortion-induced fatigue cracking in steel bridges*: Transportation Research Board.

Hassel, H.L. 2011. An Analytical Evaluation of Distortion-Induced Fatigue in Steel Bridges.

Jajich, D, and AE Schultz. 2003. Measurement and Analysis of Distortion-Induced Fatigue in Multigirder Steel Bridges. *Journal of Bridge Engineering* 8:84.

Keating, P.B. 1994. Focusing on fatigue. *Civil Engineering—ASCE* 64 (11):54-57.

Keating, PB, and JW Fisher. 1987. Fatigue behavior of variable loaded bridge details near the fatigue limit. *Transportation Research Record* (1118).

Lindberg, A., and A. Schultz. 2007. Incorporation of Fatigue Detail Classification of Steel Bridges into the Minnesota Department of Transportation Database.

Roddis, K, and Y Zhao. 2001. Out-of-plane fatigue cracking in welded steel bridges. *Welding Innovations* 27 (2):2-7.

CHAPTER 3. USE OF CFRP OVERLAYS TO REPAIR FATIGUE DAMAGE IN STEEL PLATES UNDER TENSION LOADING

Abstract

A total of 17 specimens with pre-existing fatigue cracks were tested under cyclic loading to evaluate the performance of composite overlays when used to repair fatigue damage in steel structures. Two control specimens were tested without overlays and the remaining 15 were repaired with Carbon Fiber Reinforced Polymer (CFRP) overlays of various thicknesses. In some of the specimens, composite overlays were removed for inspection and re-attached every million cycles to track the propagation of fatigue cracks in the steel. It was found that specimens repaired with composite overlays had fatigue-crack propagation lives exceeding 3 million cycles, while the observed propagation life of untreated specimens was less than 60,000 cycles. Results from a series of Finite Element (FE) Analyses showed that the peak stress demand was reduced by approximately 80% with the addition of composite overlays when compared with untreated specimens, which is consistent with the observed change in fatigue-crack propagation rate observed in the experiments.

Introduction and Background

A significant number of aging steel bridge structures experience structural problems due to fatigue cracks. After fatigue cracks become large enough to be detected, some repair measure must be undertaken to prevent structural failure of the member and potentially serious damage to the bridge. Methods that have been used in the past to repair fatigue cracks in metal structures

42

include drilling of crack-stop holes, grinding and re-welding, ultrasonic impact treatment, bolting, and the attachment of fiber reinforced polymer (FRP) overlays. FRP overlays may be used as a preventive measure to enhance the fatigue life of a bridge or as a repair method to arrest cracks and prevent further crack growth.

This study investigates the use of carbon fiber reinforced polymer (CFRP) overlays to repair fatigue cracks that have already been detected. The main advantage of CFRP overlays is that, if proportioned and bonded properly to the steel, the stress demand in a vulnerable element or connection can be reduced significantly, drastically reducing the rate of crack growth. One of the most important concerns when implementing this repair method is to achieve adequate bond between the steel and the composite overlay. Voids or imperfections in the layer of resin used to attach the composite overlay to the underlying metal can lead to the formation and propagation of fatigue cracks within the resin. Preventing the initiation of fatigue cracks within the bond layer is of paramount importance because these cracks can eventually cause debonding of the overlay, rendering the repair ineffective.

A significant amount of research on the use of composite materials to repair fatigue cracks has been carried out in the field of aerospace engineering to address fatigue problems in the fuselages of airplanes (Mall and Conley 2009); Umamaheswar and Singh 1999); Schubbe and Mall 1999); Naboulsi and Mall 1996); Lee and Lee 2004); Liu, Xiao, et al. 2009). The most recent research performed on this topic in the aerospace field has focused on the use of FRP patches to repair fatigue damage in aluminum plates (Liu, Xiao, et al. 2009).

Bonding of CFRP patches to aluminum panels in the aforementioned studies is an elaborate process. For example, in an experimental study performed by Sabelkin et al, (2006), a grit blast/silane (GBS) surface preparation technique was used that involved grit blasting the

aluminum surface, applying a hydrolyzed silane solution that was cured at 104 °C (219 °F) for

one hour after being applied, and later sprayed with a corrosion inhibiting primer.

In general, researchers in the aerospace field classify aluminum plates in terms of

thickness, with a thickness of 6 mm ($^1/_4$ in.) considered to be the threshold between thin and

thick plates (Sabelkin et al. 2006). A commonly used parameter for proportioning composite

patches for the purpose of repairing fatigue damage is the ratio of axial stiffness of the composite

patch to the axial stiffness of the plate (Sabelkin et al. 2006). The ratio is defined as:

$$SF = E_{FRP}\, t_{FRP}/\, E_s\, t_s \qquad\qquad\qquad\qquad (3.1)$$

where SF is the stiffness ratio, E_{FRP} is the modulus of elasticity of the FRP, t_{FRP} is the thickness

of the FRP patch, E_s is the modulus of the steel, and t_s is the thickness of the steel plate. The SF

parameter is used to determine the number of layers needed to repair fatigue damaged plates by

assuming that the driving force is redistributed in proportion to the relative axial stiffness of the

two materials. For aerospace structures the recommended stiffness ratio is 1.0 (Schubbe et al.

2009). Schubbe et al. (1999) performed experimental tests on aluminum plates that were

repaired with a bonded composite patch. They found that as the stiffness ratio of the repair to

plate increased, so did the fatigue life of both thin and thick plates. Stiffness ratios of 1.0 and 1.3

were evaluated in that study.

Studies evaluating the use of FRP patches for repairing fatigue damage in the aerospace

field have generated very positive results. An experimental study by Mall and Conley (2009)

investigated the behavior of aluminum plates reinforced with unidirectional boron fibers. The

thickness of the aluminum plate was 6.35 mm ($^1/_4$ in.) and the thickness of the fiber patch was

1.14 mm (45 mils). The load ratio r for the specimens was 0.1, and the maximum stress was 240

MPa (39 ksi) in tension. Mall and Conley (2009) concluded that crack size played an important

role on the fatigue-crack propagation life of specimens repaired with FRP patches, and they found good agreement between the results from Finite Element (FE) models and experimental results. The authors reported that bonding an FRP patch to only one side of the aluminum specimen increased the fatigue-crack propagation life of the specimen between four and 10 times with respect to the propagation life of the untreated specimen. Wang et al. (2002) also found an increase in fatigue-crack propagation life on the order of 10 times in aluminum plates repaired with FRP patches.

Several studies have investigated the use of composite overlays to repair fatigue-related damage in steel structures. (Tavakkolizadeh and Saadatmanesh 2003) studied the effectiveness of CFRP sheets to improve the fatigue strength of steel girders. In this study, flanges of small I-shaped steel beams (S3226x114 (S127x4.5)) were cut to create a notch crack. Unidirectional CFRP sheets were bonded over the area of the notch and the beams were tested under various stress ranges ranging from 138 MPa (20 ksi) to 345 MPa (50 ksi). Surface preparation of the steel flanges consisted of sandblasting, washing with saline solution, and rinsing. A total of six specimens were repaired with CFRP sheets and tested. Observed crack growth rates for the retrofitted beams ranged between 25% and 40% of the growth rate for unretrofitted beams. The authors reported that the fatigue-crack propagation life of the specimens with CFRP sheets was extended by a factor of approximately three compared with that of control specimens.

Liu, Al-Mahaidi, et al. (2009) studied the tensile fatigue behavior of notched steel plates strengthened with single-ply CFRP patches. One of the parameters studied was the modulus of elasticity of the carbon fiber used to manufacture the CFRP patch. One set of patches, designated high modulus, had carbon fibers with a modulus of elasticity of 640 GPa (93,000 ksi), while the other set, designated normal modulus, had carbon fibers with a modulus of elasticity of

240 GPa (35,000 ksi). Another parameter in the study was the area over which the CFRP

patches were attached. Various placements were studied, including attachment over the crack,

two separate attachment areas, either covering or not covering the crack, and double or single-

sided attachment of the patch (the double sided attachment consisted of bonding CFRP patches

to both sides of the specimen). Specimens with double-sided patches were symmetric, which

prevented the introduction of any secondary stresses associated with the CFRP repair. The

authors reported that the single-sided repair extended the fatigue-crack propagation life of the

specimen by a factor ranging between 2.2 and 2.7, whereas the double sided repair extended the

fatigue-crack propagation life by a factor ranging between 4.7 and 7.9. Roy et al. (2009)

performed a study using the same type of materials and procedure used by Liu et al. (2009), but

focused the study on the single sided repair because of the inherent asymmetry. Roy et al.

(2009) reported that the fatigue-crack propagation life was increased by a factor of 2.2 compared

with that of the control specimens. Both Liu et al. (2009) and Roy et al. (2009) showed similar

increases in fatigue-crack propagation life of steel plates repaired with single-sided CFRP

patches.

Analytical modeling of CFRP repairs using the Finite Element method is also very

important to develop efficient retrofit schemes. To properly determine the effects of the repair

through use of computer models it is important to define the materials properties of the specimen

as accurately as possible. Liu et al. (2009) and Lee and Lee (2004) developed analytical models

that included nonlinear material properties, and reported that such level of refinement was

unnecessary if the steel plate thickness was greater than 6 mm ($^1/_4$ in.). Material nonlinearities

only played an important role when the thickness of the steel plate was less than 6 mm ($^1/_4$ in.),

due to the stress intensity factor.

Several researchers (Liu, Xiao, et al. 2009); Lee and Lee 2004) have shown good agreement between the change in stress demand estimated using FE models and experimentally observed changes in fatigue-crack propagation life.   The aforementioned researchers defined the material properties in their FE models as linear elastic. One of the limitations of linear elastic models is that although such models are capable of providing a good representation of the stress field in most of the element being analyzed, limited information can be obtained about the potential for debonding of the composite, which has been shown to be a critical mode of failure in fatigue tests. In FE models that include a layer of resin between the CFRP overlay and the underlying metal, the potential for debonding can be assessed by comparing the stress demand in the resin with a limiting value. The limiting stress, for example, can be taken as a fraction of the shear strength of the adhesive. This approach was adopted in the FE simulations conducted in this study.

Objective and Scope

The primary objective of the study described in this paper was to investigate the use of composite materials to repair fatigue damage in steel structures. Bonding of CFRP overlays was performed using simpler techniques than those used in the aerospace field (Sabelkin et al., 2006), so that repairs would be more representative of the kind of work that can practically be performed under field conditions on bridge structures. Experiments were conducted to evaluate if fatigue-crack propagation under constant amplitude tensile load was similar in steel specimens repaired with two different types of composite overlays adhered to the steel using different bonding techniques, and to evaluate if the observed performance was similar to that reported in previous studies on aluminum plates reinforced with composite patches. Additionally, the

thickness of the composite overlays was varied to determine the effect of the axial stiffness parameter *SF* on the effectiveness of CFRP overlays.

The study also comprised a suite of Finite Element simulations to investigate the validity of using the axial stiffness parameter *SF*, frequently referenced in studies on aluminum plates, to estimate the reduction in stress demand. The FE simulations were intended to evaluate the correlation between fatigue-crack propagation rates and computed values of Hot Spot Stress (HSS). The use of HSS as a design parameter was evaluated because it is a versatile parameter that may be used for various types of geometric configurations, materials, and loading conditions.

Finite Element Simulations

Finite element simulations of the specimens tested during the experimental program (Fig. 3-1) were carried out using the commercially-available Finite Element analysis software ABAQUS version 6.8.2 (Simulia, 2009).
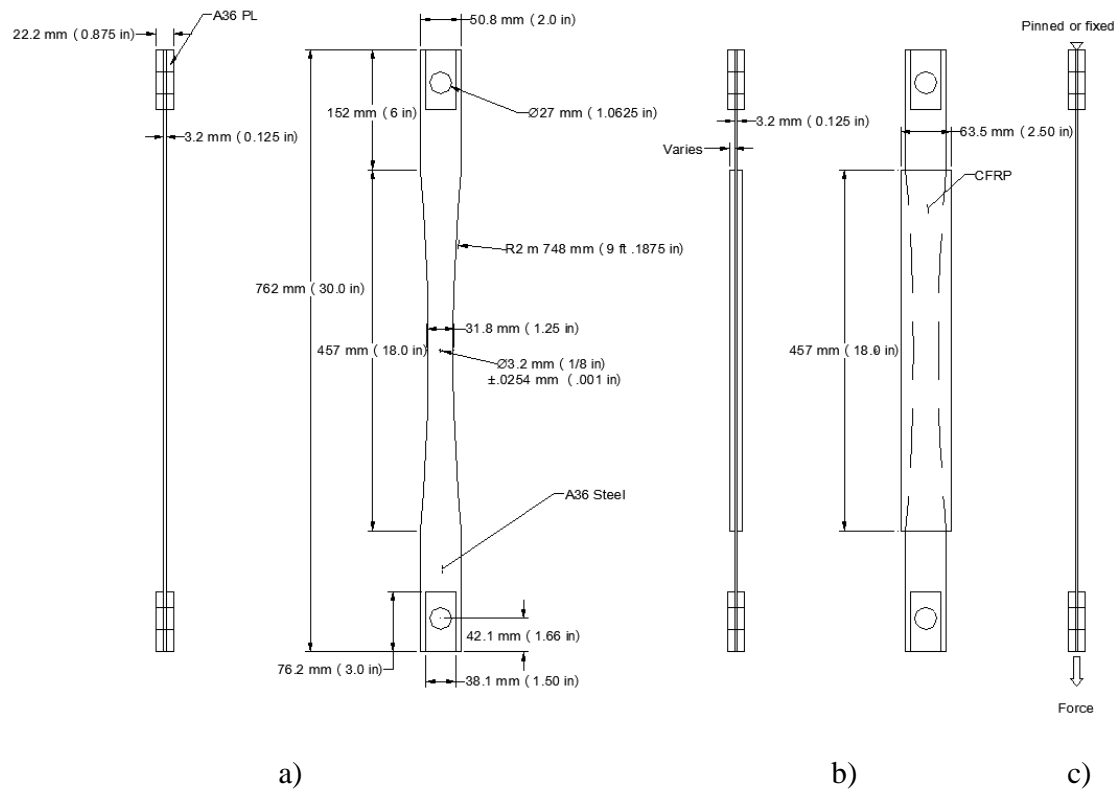
Figure 3-1 : Tension specimen: a) bare steel b) specimen with CFRP overlay attached c) boundary and loading conditions imposed on the FE model.

The FE models were developed using linear elastic material models and meshes were assembled using 8-node brick elements. The modulus of elasticity for the steel, composite overlay, and resin were selected as 200, 83, and 2 GPa (29,000, 12,000, and 300 ksi), respectively. The mesh density was defined such that elements would be 0.30 mm (0.01 in.)

within a region 51 mm (2.0 in.) from the center hole, and 2.5 mm (0.1 in.) in all other parts of the specimen. Interfaces between the steel and composite parts of the model were defined using tie constraints. Motion was restrained at one end of the model while the other end was free to move only in the vertical direction (Fig. 3-1c). Two concentrated loads were applied in the vertical direction at the unrestrained end, one on each face of the model. Fig. 3-2 shows maximum principal stresses for models with and without CFRP overlays attached. These maximum principal stresses were extracted along a path starting at the center of the steel plate and ending at the edge (Fig. 3-3) for comparison with other model results.

a)   b)
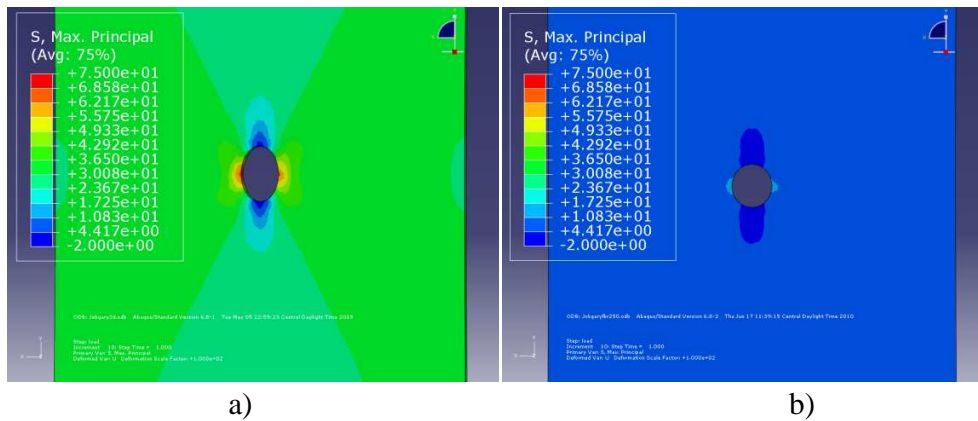
Figure 3-2 : Maximum principal stresses at the center of the specimen for the a) unreinforced configuration, and b) reinforced configuration
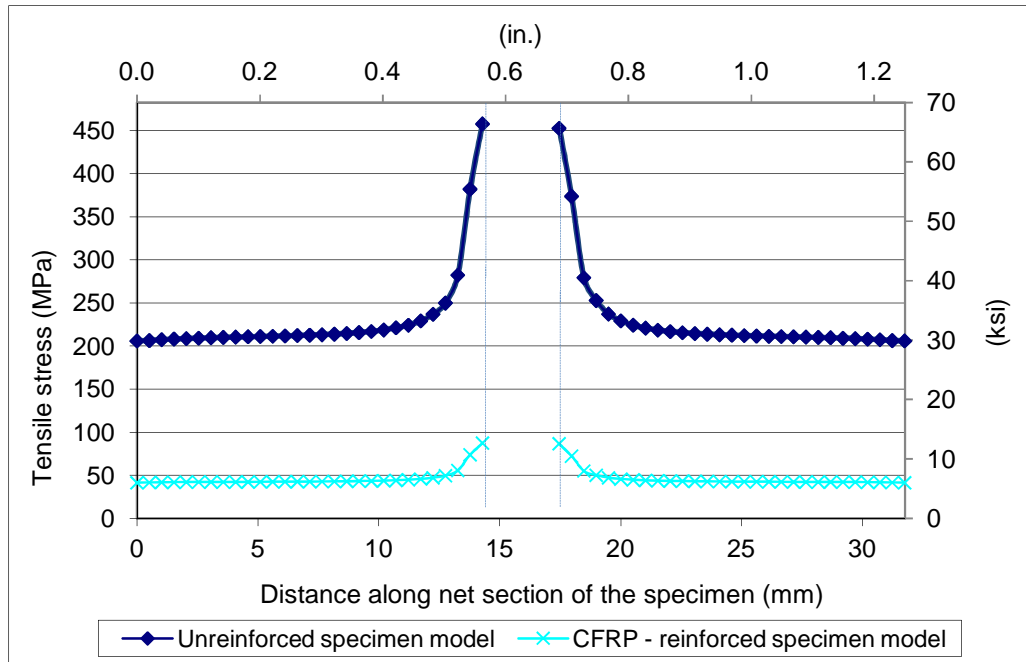
Figure 3-3 : Maximum principal stresses at the location of net cross-section for CFRP-reinforced and unreinforced specimens

The path was defined through points located at the mid-thickness of the steel plate, along the cross-section through the net section of the steel. The magnitude of the stress demand along the path is shown for the unreinforced and CFRP-reinforced conditions in Fig 3. A comparison of the stresses presented in Fig 3 indicates that reinforcing the steel specimen with composite overlays resulted in a reduction of the peak stress demand of approximately 80%.

Although maximum principal stresses shown in Fig 3 were extracted along the entire path through the steel net section, further comparisons were performed on the basis of the Hot Spot Stress (HSS). In this paper, HSS was defined as the stress at a distance half the thickness of the steel plate away from point of peak stress, which occurred at the edge of the hole in this case (Marquis and Kaehoenen 1995). Hot Spot Stress analysis was used as an indicator of stress

51

range, and consequently, as a measure of the effectiveness of various composite overlay configurations.

The suite of finite element simulations performed in this study were intended to investigate the effects of four different parameters on the fatigue performance of the retrofit scheme: modulus of elasticity of the CFRP, thickness of the CFRP overlay, length of the CFRP overlay, and thickness of the interface layer used to bond the CFRP overlay to the steel. The effect of the four parameters investigated is discussed in the following.

Effect of the Modulus of Elasticity of the CFRP

Six different models were developed to investigate the effect of the modulus of elasticity of the CFRP on stress demand imposed on the steel specimen. Each of the models discussed in this section had identical properties with the exception of the modulus of elasticity of the CFRP, which was varied between 27 GPa (3,860 ksi) and 138 GPa (20,000 ksi), in increments of 28 GPa (4,000 ksi). Thickness of the composite overlays was maintained as 6.4 mm ($^1/_4$ in.), the length of the CFRP patch was maintained as 458 mm (18 in.), and the thickness of the interface layer was held at 0.6 mm (25 mils). The effect of CFRP modulus of elasticity on hot spot stress in the steel specimen is shown in Fig 4. The point corresponding to a modulus of elasticity of zero represents results from the analysis of the specimen without an overlay. As the results show, the relationship between axial stiffness of the CFRP patch and HSS was parabolic in nature, indicating that there was a significant advantage associated with using an overlay, even if the modulus of elasticity of the composite material was relatively low. As Fig. 3-4 shows, HSS dropped by 58% with the introduction of an overlay with a very low modulus (26,600 MPa,

3,860 ksi) when compared with the unreinforced case. Increasing the modulus of elasticity of the CFRP by a factor of five, from 26,000 MPa (3,860 ksi) to 138,000 MPa (20,000 ksi), led to a reduction in HSS by a factor of approximately three. This data shows that increasing the modulus of elasticity of the CFRP material exhibits diminishing returns, which is important to consider when determining optimal configuration of the overlay. If infinite fatigue or propagation life can be achieved with a relatively inexpensive overlay, there is no economic incentive for using stiffer, and often much more expensive, fibers.
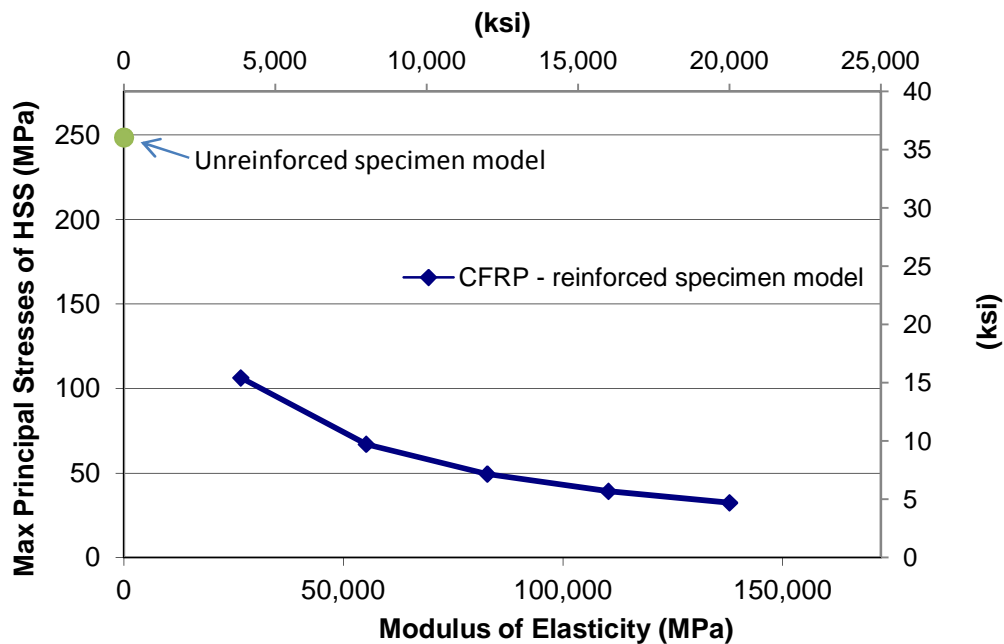
Figure 3-4 : Effect of the stiffness of the CFRP overlays on maximum principal Hot Spot Stresses in the steel specimen

Effect of the Thickness of the CFRP Overlay

The effect of the CFRP overlay thickness on HSS was evaluated using five different FE models. In these models all parameters were kept constant while the thickness of the CFRP

overlay on each side was varied using values of 1.6, 2.4, 3.2, 6.4, and 12.7 mm (63, 94, 125, 250, and 500 mils). For all models discussed in this section, the modulus of elasticity of the overlay was maintained at 83 GPa (12,000 ksi), the length of the CFRP overlay was kept as 457 mm (18 in.), and the thickness of the interface resin layer was held at 0.6 mm (25 mils). Results are presented in Fig. 3-5. The relationship between the CFRP overlay thickness and the maximum principal HSS was found to be inversely proportional. Similar to the behavior found when the CFRP modulus of elasticity was varied, increasing the thickness of the overlay exhibited diminishing returns, with the largest change in HSS observed between the unreinforced case and the case in which a 1.6-mm (63-mil) thick overlay was utilized.

Figure 3-5 : Effect of the CFRP overlay thickness on maximum principal Hot Spot Stresses in the steel specimen (update graph)

Effect of the Length of the CFRP Overlay

Six different configurations were defined to investigate the effect of the length of the CFRP overlay on the HSS along the critical path in the steel substrate. This effect was evaluated in terms of the total length of the CFRP overlay, with the overlay centered with respect to the center of the hole of the steel specimen. A total of six models were developed, with overlay lengths varied from 152 mm (6 in.) to 457 mm (18 in.), which is a dimensional range equivalent to 24-72 hole diameters. For all models, the modulus of elasticity of the overlay was held at 83 GPa (12,000 ksi), the thickness of the CFRP overlay was maintained as 6.4 mm ($^1/_4$ in.), and the thickness of the interface layer was kept as 0.6 mm (25 mils). The results, presented in Fig. 3-6, show that there was a very small reduction in HSS in the steel substrate when the CFRP overlay length was changed from 152 mm (6 in.) to 203 mm (8 in.). For overlay lengths greater than 203 mm (8 in.) the effect of the overlay length on maximum principal HSS was found to be negligible.
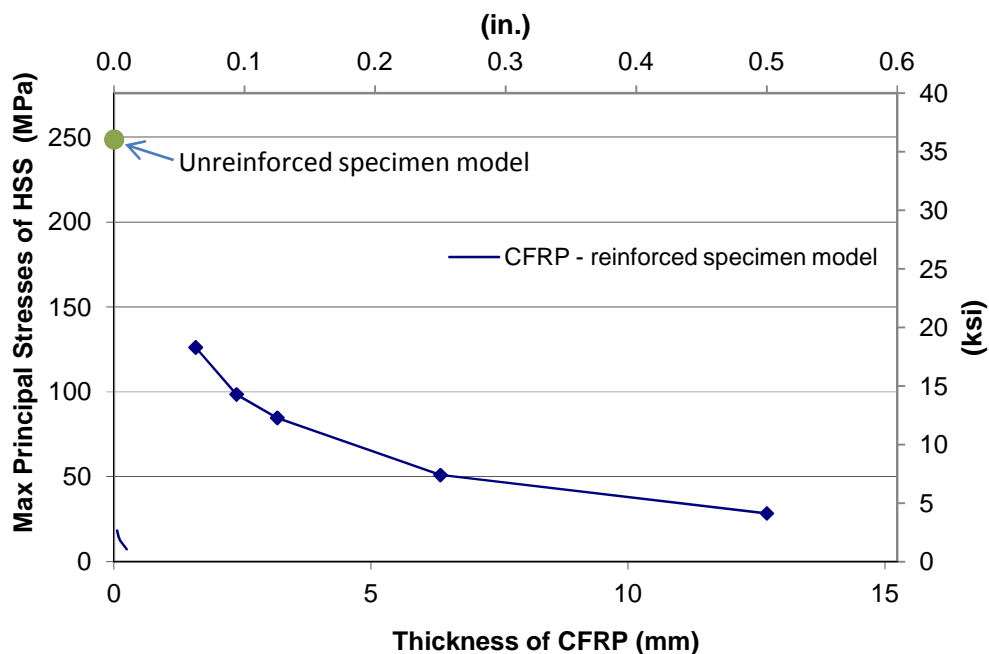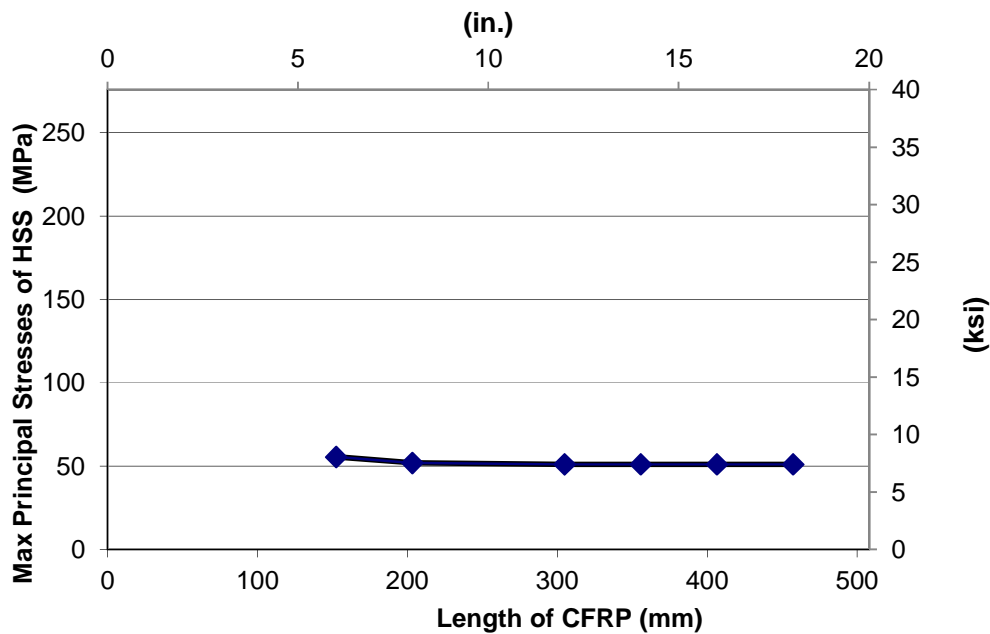
Figure 3-6 : Effect of the CFRP overlay length on maximum principal Hot Spot Stresses in the steel specimen

Effect of Thickness of Bond Layer

One of the parameters often neglected in FE simulations of retrofit measures with composite overlays is the flexibility inherent to the adhesive resin used to bond the overlay to the metal substrate. To achieve adequate bond, a resin with demonstrated acceptable adherence to steel must be employed. In most analyses found in the literature (Sabelkin et al. 2006); Liu, Xiao, et al. 2009); Mall and Conley 2009), it was assumed that the thickness of such a layer was very small, and that there was perfect bond between the composite and the substrate. Explicit modeling of this layer provides an indication of the average shear demand on the resin and the tensile demand on the resin-steel interface, which can be used to gage the potential for debonding. Because the shear and tensile demands on the resin are affected by the thickness of

56

the resin layer, this is an important parameter to consider in terms of fatigue and fatigue crack propagation life.

A total of five different models were defined to investigate the effect of the thickness of the interface bond layer between the CFRP overlay and the steel substrate, with the interface layer thickness ranging from 0.6 mm (20 mils) to 5 mm (200 mils). For all models discussed in this section, the modulus of elasticity of the overlay was maintained as 83 GPa (12,000 ksi), the thickness of the CFRP overlay was kept as 6.4 mm ($^1/_4$ in.), the length of the CFRP overlay was held at 457 mm (18 in.), and the modulus of elasticity of the bond layer maintained as 2 GPa (300 ksi). The analyses results presented in Fig. 3-7 indicate that the maximum principal HSS was not affected by the thickness of the resin layer, suggesting that an increase in the thickness of the resin layer has a negligible effect on the effectiveness of the retrofit measure.
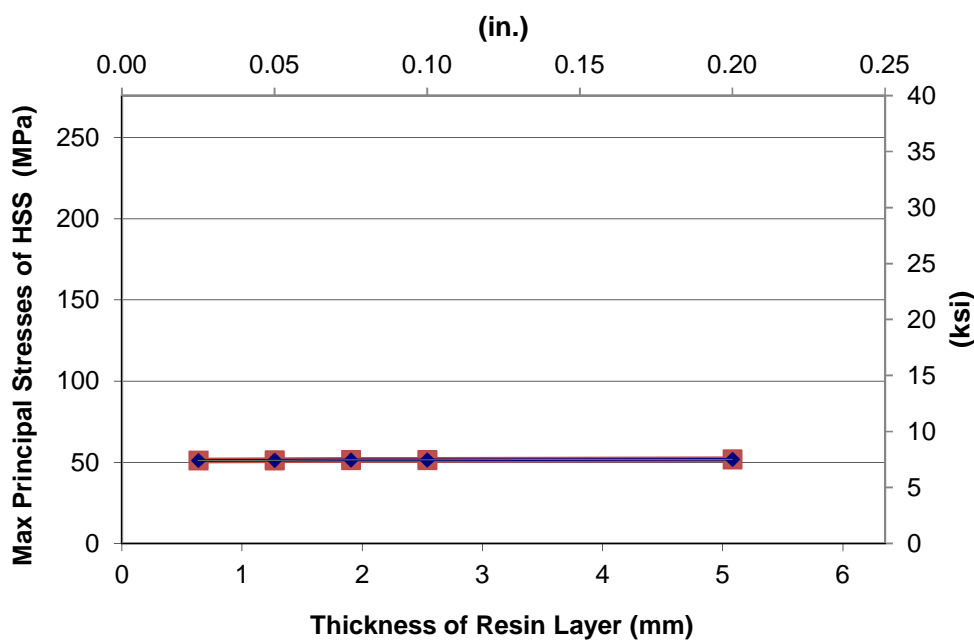
Figure 3-7 : Effect of the resin bond layer thickness on maximum principal Hot Spot Stresses in the steel specimen
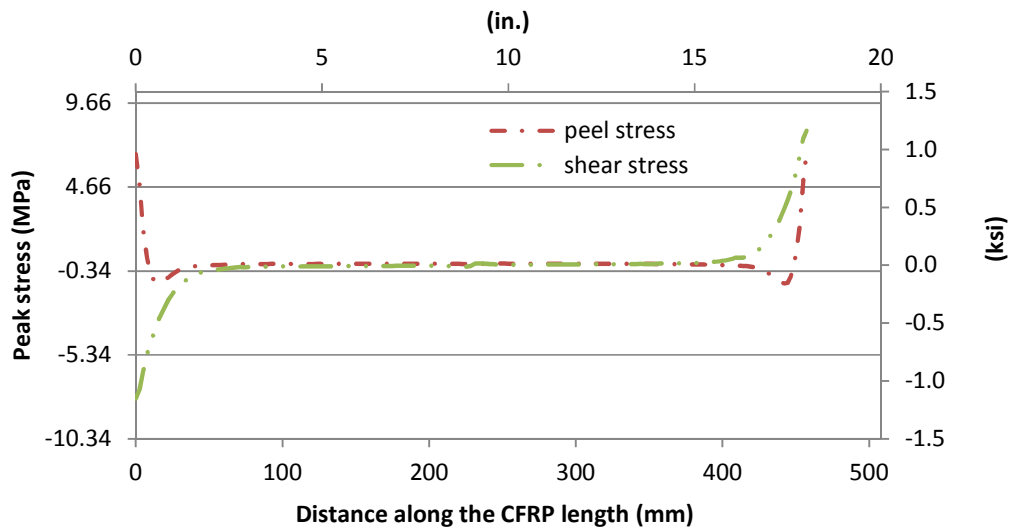
Figure 3-8 : Peak stresses along the CFRP overlay on resin layer end of hole
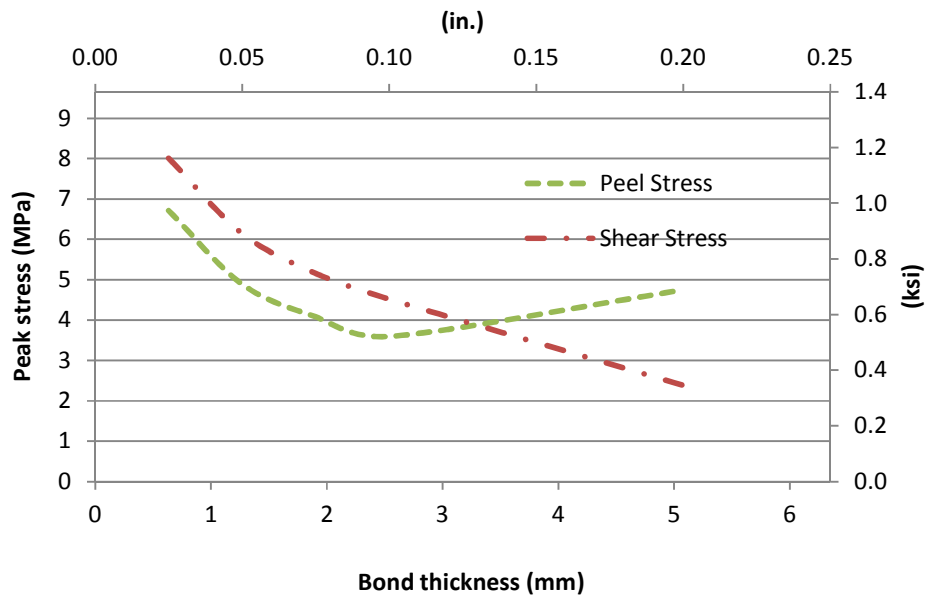
Figure 3-9 : Peak stress demands on the CFRP layer as a function of resin layer thickness

Although the FE analyses showed that the thickness of the resin layer had a negligible effect on the HSS, another important design consideration is the effect of the thickness of the resin layer on the stress demand at the resin layer itself. This is important because maintaining bond between the composite and the steel is critical to the successful performance of the retrofit scheme, and higher stress demands increase the probability of fatigue failure at the interface. Fig. 3-8 shows the stress demand along the resin layer for a model with a layer thickness of 0.6 mm (20 mils). As Fig. 3-8 presents, the shear and peel stress (out of plane stress) demands are relatively low along most of the interface. Stress demands are greatest at both ends of the interface, and this is the location considered to be the most susceptible to fatigue failure.

Figure 3-9 presents the variation of peak shear and peel stresses as a function of the thickness of the resin layer. The results show that increasing the interface layer thickness from 0.6 mm (20 mils) to 5.0 mm (200 mils) caused a reduction in peak shear demand by approximately 66%. Figure 3-9 also presents that the same increase in the thickness of the interface layer led to a reduction in peak peel stresses by approximately 40%. The trend observed for the peel stress was different from that observed for the shear stress in that the lowest peel stress demand was observed when an interface thickness of 2.5 mm (100 mils) was used, and any further increases in the thickness of the interface layer led to an increase in the peel stress. Figures 3-7, 3-8, and 3-9 show that although the thickness of the interface layer may not be relevant to fatigue-crack propagation life due to the negligible effect on the stress range, it is a very important parameter in terms of the bond performance of the interface layer under cyclic loading.

Results from the suite of FE analyses showed that that the effect of the thickness of the interface resin layer and the length of the CFRP overlay on the maximum principal HSS were

much less significant than the effects of the thickness of the overlay and the modulus of elasticity of the CFRP, with the modulus of elasticity of the CFRP being the most significant of all four parameters.

Ratio of Overlay Axial Stiffness to Steel Axial Stiffness

As discussed in Section 1, one of the design parameters referenced in the literature for proportioning FRP patches is the ratio of axial stiffness of the composite patch to the axial stiffness of the underlying plate (Eq.3.1). As Eq. 3.1 shows, this ratio may be modified by changing the modulus of elasticity of the FRP, the thickness of the FRP, or both. The results referenced in Sections 2.1 and 2.2 were used to derive two curves showing the effect of the stiffness ratio *SF* on the maximum principal HSS in the steel substrate. For each curve, one of the two parameters (modulus of elasticity of the FRP and thickness of the overlay) was varied while maintaining the other constant. In all models discussed in this section, the length of the overlay was 457 mm (18 in.) and the thickness of the interface layer was 0.6 mm (25 mils). When calculating the stiffness for the thickness of FRP curve the modulus of elasticity was taken to me 83 GPa (12,000 ksi).

The results presented in Fig 10 show that changing the stiffness ratio *SF* by changing the modulus of elasticity of the CFRP had consistent results with changing the *SF* ratio by altering overlay thickness. There was a common trend, in that sequential increments in the thickness of the overlay and the modulus of elasticity of the CFRP resulted in similar reductions on the HSS. These results suggest that in terms of improving fatigue-crack initiation life and fatigue-crack

propagation life, the configuration of the overlay is just as important as ensuring that the overlay remains bonded to the steel.
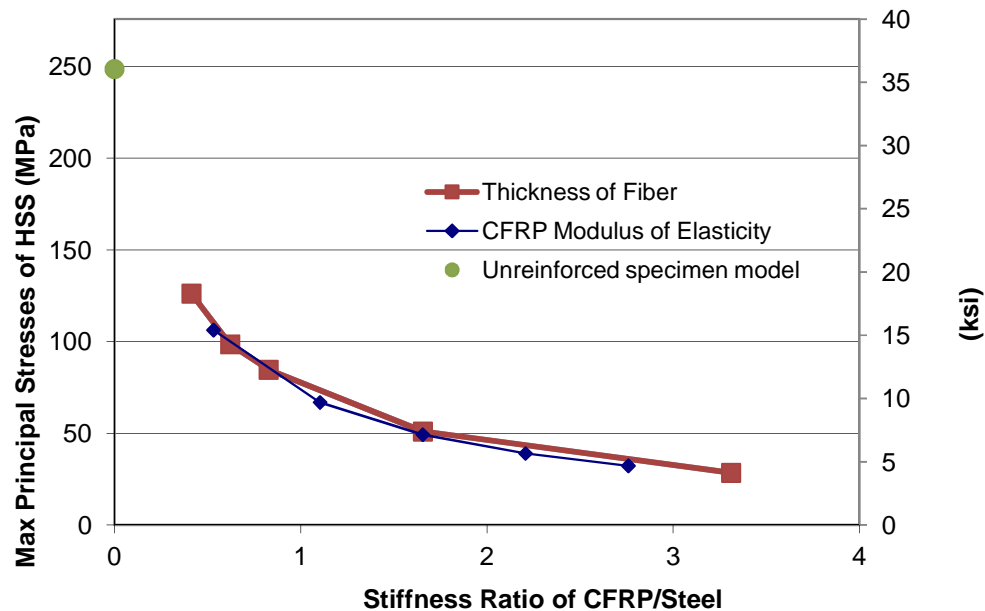
Figure 3-10 : Effect of the stiffness ratio on stress demand

Experimental Program

The goal of the experimental program was to evaluate the fatigue-crack propagation life of steel specimens with pre-existing fatigue cracks repaired using CFRP overlays under cyclic loading. The text matrix for the experimental program is summarized in Tables 3-1 and 3-2. Two unreinforced control specimens were tested with nominal stress ranges of 166 MPa (24 ksi) and 221 MPa (32 ksi). Two specimens were repaired with CFRP overlays with dimensions shown in Fig.1 (specimen thickness of 3mm, $^1/_8$ in., and overlay thickness of 6mm, ¼ in.). The specimens were tested at two different stress ranges, 166 MPa (24 ksi) and 221 MPa (32 ksi). A

third specimen was repaired using CFRP chopped fibers and was tested at 166 MPa (24 ksi).

Chopped fiber length was 38 mm (1.5 in.). These five specimens were used to determine the

relative effectiveness of the two types of CFRP repairs in extending fatigue life. The behavior of

these steel specimens was also compared with that of aluminum specimens.

Table 3-1: Specimen test matrix

Specimen Designation	Overlay Type	CFRP Overlay Thickness mm (in.)	Stress Range *MPa (ksi)*	Number of Cycles	Final Crack Size mm (in.)
Control 1	None		221 (32)	18,000	Total Failure
Control 2	None		166 (24)	55,000	Total Failure
F 9	14-Layer CFRP	6.4 ($^1/_4$)	221 (32)	3,000,006	5.08 (0.20)
F 10	Chopped-CFRP	6.4 ($^1/_4$)	166 (24)	1,084,699	2.79 (0.11)
F 12	14-Layer CFRP	6.4 ($^1/_4$)	166 (24)	4,059,048	5.08 (0.20)

The12 remaining tensile specimens were testing using varying thicknesses of CFRP

overlays and varying stress ranges to determine the effect of stiffness ratio on fatigue-crack

propagation life. Each of these specimens was tested until the fatigue crack had completely

propagated through the width of the specimen or until infinite fatigue life was reached. The test

matrix for these 12 specimens is shown in Table 3-2. In all cases the composite overlays were

attached to both sides of the specimen and the thickness of the bond layer was 0.6 mm (25 mils).

Table 3-2: Specimen test matrix

Specimen Designation	Specimen Thickness mm (in.)	CFRP Overlay Thickness mm (in.)	Stress Range MPa (ksi)	Number of cycles
F15	3.0 ($^1/_8$)	1.6 ($^1/_{16}$)	263 (38)	18,900
F3	3.0 ($^1/_8$)	1.6 ($^1/_{16}$)	221 (32)	60,000
F6	3.0 ($^1/_8$)	1.6 ($^1/_{16}$)	166 (24)	340,700
Pick 12	3.0 ($^1/_8$)	2.4 ($^3/_{32}$)	221 (32)	271,100
Pick11	3.0 ($^1/_8$)	3.2 ($^1/_8$)	263 (38)	95,100
F14	3.0 ($^1/_8$)	3.2 ($^1/_8$)	221 (32)	313,050
F2	3.0 ($^1/_8$)	3.2 ($^1/_8$)	166 (24)	1,450,095
Pick10	3.0 ($^1/_8$)	6.4 ($^1/_4$)	263 (38)	282,550
Pick13	3.0 ($^1/_8$)	6.4 ($^1/_4$)	221 (32)	*IFL
Pick7	3.0 ($^1/_8$)	6.4 ($^1/_4$)	166 (24)	*IFL
F4-25	6.0 ($^1/_4$)	1.6 ($^1/_{16}$)	221 (32)	15,600
F4-21	6.0 ($^1/_4$)	3.2 ($^1/_8$)	221 (32)	160,150
F4-23	6.0 ($^1/_4$)	6.4 ($^1/_4$)	221 (32)	571,650
F4-20	6.0 ($^1/_4$)	12.8 ($^1/_2$)	221 (32)	*IFL
IFL* Infinite Fatigue Life				

Measured material properties are presented in Table 3-3. Coupon tests (ASTM 2000) from single-layered specimens showed that the modulus of elasticity of the CFRP was approximately 83 GPa (12,000 ksi). Liu et al. (2009) observed in their experiments that successive layers of CFRP in a repair patch experienced diminishing strain demands. For example, their measurements showed that the third layer of a composite overlay experienced 17 % of the strain of the first layer. Because measurements by Liu et al. (2009) showed that after the second layer the strain demand quickly dropped, the modulus of elasticity of the composite used for the computer simulations was selected to be between measured values for one and three layers.

The modulus of elasticity of the 9412 Hysol resin was also measured using coupon tests

(Table 3-3) performed as prescribed by (ASTM 2000). The measured modulus of elasticity of

the Hysol resin was 2.1 GPa (300 ksi).

Table 3-3: Measured material properties

Continuous CFRP

No. of Layers in Coupon	No. of Coupons	Avg. Modulus of Elasticity	Standard Deviation
		GPa (ksi)	*GPa (ksi)*
1	3	85.8 (12,440)	10.0 (1,450)
3	4	75.3 (10,930)	10.9 (1,580)
5	3	61.7 (8,940)	0.3 (42.0)

9412 Hysol Resin

Coupon Thickness *mm (in.)*	No. of Coupons	Avg. Modulus of Elasticity *GPa (ksi)*	Standard Deviation *GPa (ksi)*
6.4 (0.25)	6	2.1 (303)	0.2 (25)

Chopped-CFRP Composite

Coupon Thickness *mm (in.)*	No. of Coupons	Avg. Modulus of Elasticity *GPa (ksi)*	Standard Deviation *GPa (ksi)*
4.8 (0.19)	7	14.1 (2,052)	6 (866)

Specimen Properties

The specimens were fabricated using grade A36 steel and were either 3 mm ($^1/_8$ in.) or 6

mm ($^1/_4$ in.) thick. The stress-strain relationship obtained for the steel is presented in Fig. 3-11.

The measured yield strength of the steel was 303 MPa (44 ksi), and the tensile strength was 460

MPa (67 ksi).
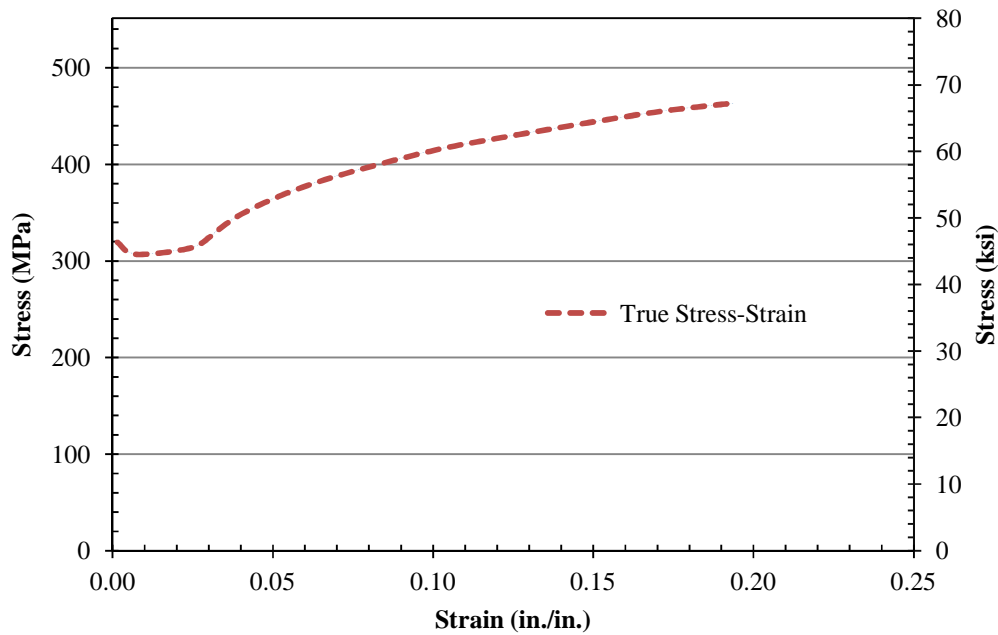
Figure 3-11 : Stress strain curve for steel

Specimen dimensions are shown in Fig. 3-1. Each specimen had a drilled and reamed hole at the center of the specimen with a diameter of 3 mm ($^1/_8$ in.). Both sides of the hole had pre-existing fatigue cracks. The specimens summarized in Table 3-1 had a pre existing fatigue crack of approximately 2.5 mm (0.1 in.). The specimens summarized in Table 3-2 had a preexisting fatigue crack of approximately 7.6 mm (0.3 in.). These initial fatigue cracks were created by loading the specimens under repeated cycles at stress ranges varying from 166 MPa (24 ksi) to 263 MPa (38 ksi).

Surface preparation

Maintaining bond under cyclic loading is critical to the successful performance of the repair methods discussed in this paper. To develop adequate bond, the steel surface was prepared by a process of abrading and cleaning. Abrading consisted of roughening of the surface with a hand

grinder to achieve a surface roughness of approximately 0.8 mm (30 mils).   After abrading,

cleaning of the surface was performed using acetone and methanol.

Fabrication of the Multi-Layered CFRP Overlays

The multi-layered CFRP overlays were pre-fabricated and subsequently attached to the

steel specimens. Each CFRP overlay consisted of single layers of CFRP bi-directional pre-

impregnated carbon fiber ply. Scotch-Weld Epoxy adhesive (1838 B/A Green) was used

between certain layers to ensure that there was a sufficient amount of resin to prevent voids from

occurring between resin layers during the curing process. Table 3-4 summarizes the amount of

single carbon fiber plys and Scotch Weld Epoxy adhesive layers used in each CFRP overlay.

Table 3-4: Fabricaton of Multi-Layered CFRP Ocerlays

Overlay Thickness mm (in.)	Number of Single Carbon Fiber Plies	Number of Layers of Scotch Weld Epoxy Adhesive	Placement of Scotch Weld Epoxy Adhesive
1.6 ($^1/_{16}$)	2	1	After 1st ply
2.4 ($^3/_{32}$)	3	1	After 2rd ply
3.2 ($^1/_8$)	4	2	After 2rd ply
6.4 ($^1/_4$)	8	3	After 3rd and 5th ply
12.8 ($^1/_2$)	16	4	After 4th, 8th, and 12th ply

Although previous experimental results (Liu et al. 2009) showed that the strain demand in

the CFRP plies after the third layer were small compared with those in the first and second

layers, the overlay was fabricated with additional layers to test and evaluate varying thicknesses

and to facilitate removal for inspection and reuse. The thickness of the overlay was controlled

during the fabrication process by using a mold consisting of aluminum plates placed between

bolted steel plates, as shown in Fig. 3-12. The fabrication process is described in the following.

First, the pre-impregnated CFRP plies were cut to dimensions of approximately 457 x 152 mm (18 x 6 in.), which was double the size of the overlays. The CFRP sheets were placed on the bottom steel plate of the mold, and were added one layer at a time. A single sheet of Scotch-Weld Epoxy adhesive (1838 B/A Green) resin with the same dimensions was added according to the schedule presented in Table 3-4.

The CFRP was surrounded by an aluminum spacer with a thickness of 6 mm ($^1/_4$ in.). Due to voids in the interfaces between layers of CFRP plies, the total thickness of the overlay was greater than the intended target thickness after all of the CFRP plies were placed in the mold. The top steel plate of the mold was then placed on top of the CFRP stack, and pressure was applied by tightening the bolts around the perimeter of the mold to reach the target thickness. At this point, the overlay was placed in the oven for curing. The curing oven was preheated to a temperature of 175 C (347 *F)*. The CFRP overlays were cured inside the metal mold for three hours, and subsequently allowed to cool to room temperature for 48 hours. After the curing process was completed, the CFRP overlays were taken out of the metal molds and cut to final dimensions of 457 x 64 mm (18 x 2.5 in.) using a diamond saw. Sand paper (grade 400) was used to smooth the edges of the CFRP. For specimens summarized in Table 3-1, a hole was drilled in the middle of the CFRP overlays with a diameter of 3 mm ($^1/_8$ in.) to facilitate alignment with the steel specimen.
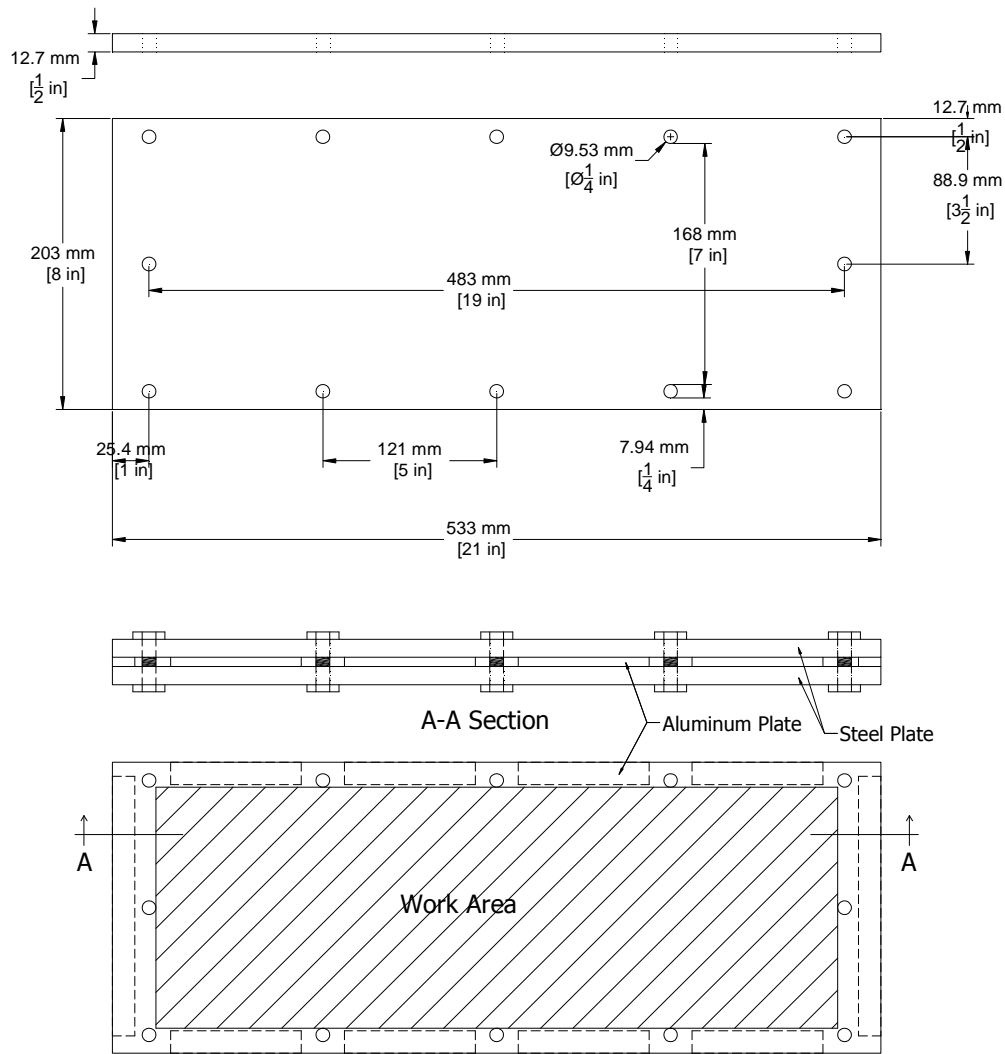
Figure 3-12 : Steel plates for making FRP plate

The CFRP overlays were attached to the steel specimen using Hysol® 9412 epoxy resin, which has a nominal shear strength of 28 MPa (4 ksi) (Hysol®). The thickness of the Hysol® layer was 0.6 mm (24 mils), maintained during fabrication by using six spacers evenly distributed throughout the interface. Drafting tape surrounding the steel plate was used to prevent leaking of the Hysol® resin by creating a resin pool. For the specimens summarized in Table 3-1 only, a bolt was used to align the steel plate and the two CFRP overlays at the center

hole. Hysol® resin was poured inside the taped-off area, and pressure was applied using grips to maintain the thickness of the interface layer at 0.6 mm (24 mils). After two days of curing the interface bond layer, final preparation was performed by cleaning the specimen of remnant resin using a chisel and a heat gun.

Fabrication of CFRP Chopped-Fiber Overlays

Use of chopped-CFRP overlays was also investigated to evaluate the performance of this type of composite material in terms of fatigue-crack propagation life; this was an attractive alternative to consider, due to simpler composite fabrication. The chopped fiber overlays were fabricated using an external mixing spray machine (a non-atomized resin lel chopper system commercialized by BINKS). The spray machine used a vinyl-ester resin with Norox MEKP-925 catalyst and graphite fiber yarn. The surface preparation performed was the same as that described in Section 3.2. After surface preparation and subsequent cleaning, the fiber-resin mix was sprayed on steel substrate in layers approximately 3-mm (130-mil) thick, and was compacted using a hand tool until the average thickness of the composite overlay was 6 mm ($^1/_4$ in.). The specimen was cured at room temperature for two days, after which the remnant resin was cleaned from the specimen.

Test procedure

A cyclic tensile load was applied at the ends of the specimen using an MTS closed-loop servo-controlled loading system. The applied load was determined on the basis of the nominal stress demand at the net section of the steel specimen, calculated using the actual (measured) net

cross sectional area without any adjustments for stress concentration in the area surrounding the hole. These values, although not representative of the peak stress demand, were adopted to simplify the comparison between various specimens. The ratio of minimum to maximum stress was maintained constant at R=0.1. The rate of fatigue-crack propagation was evaluated at three different stress ranges, 262 MPa (38 ksi), 221 MPa (32 ksi) and 166 MPa (24 ksi). A maximum tension load of 14 kN (4.4 kips) corresponded to a stress range at the middle section of 221 MPa (32 ksi) for a 3 mm ($^{1}/_{8}$ in.) thick specimen. Upon loading of specimens F9, F10, and F12, crack growth was monitored periodically. Every million cycles, the CFRP overlays were removed to measure the crack size and subsequently reattached for additional loading cycles. The reattachment procedures were the same as described in Section 3.3.

During cyclic loading of the remaining CFRP repaired specimens, those summarized in Table 3-1, the percent change in stiffness was monitored. In this case, percent change in stiffness was measured using the following equation:

% change in $K=(\delta L/\delta P)/K_{max}$ 　　　　　　　　　　　　(3.2)

where δ is the stiffness of the combined steel and CFRP overlays, L is the load placed on the specimen, P is the position reading from the testing machine, and K_{max} is the maximum stiffness recorded during testing.

Experimental Results

The propagation life of the steel specimens used in this study was calculated for different stress range demands based on established theoretical expressions, as presented in Fig. 3-13.

The relationship between crack length and number of cycles was calculated using the following expression (Barsom and Rolfe, 1999):

$$\frac{da}{dN} = A(\Delta K)^m \qquad\qquad (3.3)$$

where a is crack length, N is the number of cycles, A and m are material constants, and ΔK is a stress intensity factor range. Material constants of A=3.6E-10 and m=3 were adopted, which correspond to values for ferrite-pearlite steel (Barsom and Rolfe, 1999). The stress intensity factor depends on the ratio of crack length to plate width (a/b) and the ratio of crack length to hole radius (a/r) (Barsom and Rolfe, 1999). Stress intensity factors for various a/b and a/r ratios listed by Barsom and Rolfe (1999) were used.

As shown in Fig. 3-13, the parameters in the expression provided a close correlation between the fatigue-crack propagation life of unrepaired specimens and the theoretical propagation life for the corresponding stress range.
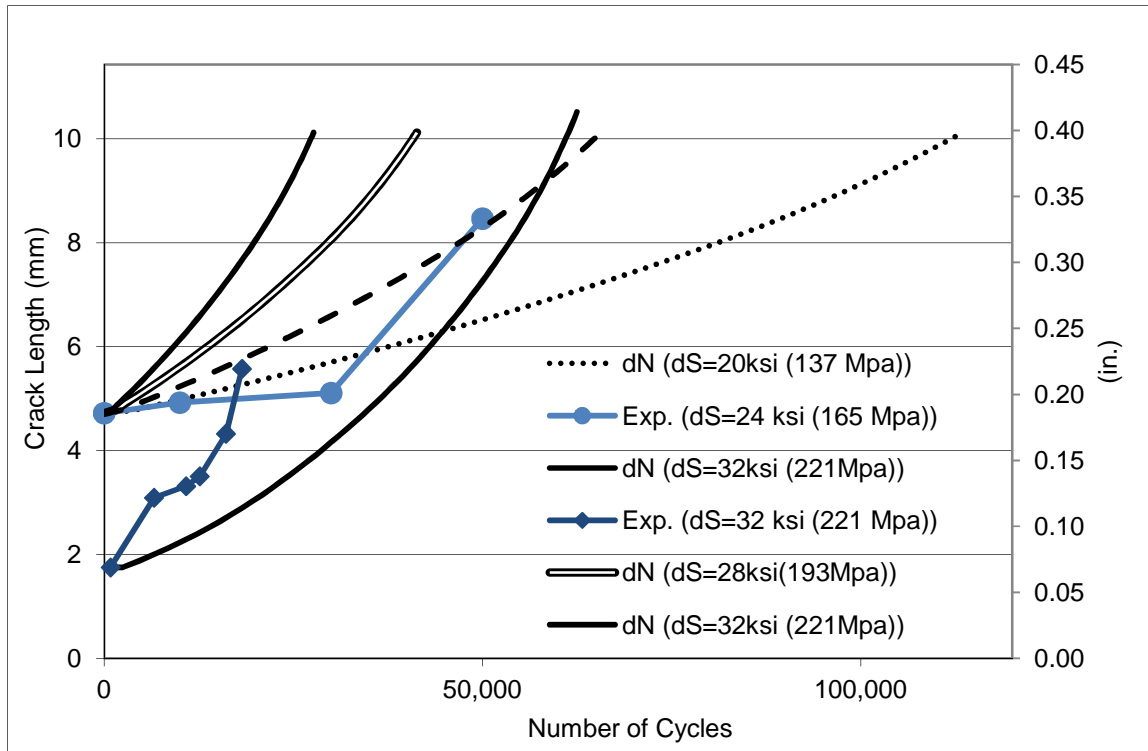
Figure 3-13 : Comparison between theoretical and experimental values for the fatigue-crack propagation life of unreinforced specimens

As indicated in Section 3, the Three nominal stress ranges ΔG, that the specimens were tested at were166 MPa (24 ksi), 221 MPa (32 ksi) and 263 MPa (38 ksi) . These values were computed by dividing the applied force by the cross sectional area at the net section of the specimen, which was approximately 90 mm^2 (0.14 in^2). A comparison between observed fatigue-crack propagation rate of the specimens with CFRP overlays summarized in Table 3-1 and the calculated fatigue-crack propagation rate in unreinforced specimens with low stress demands is presented in Fig. 3-14.
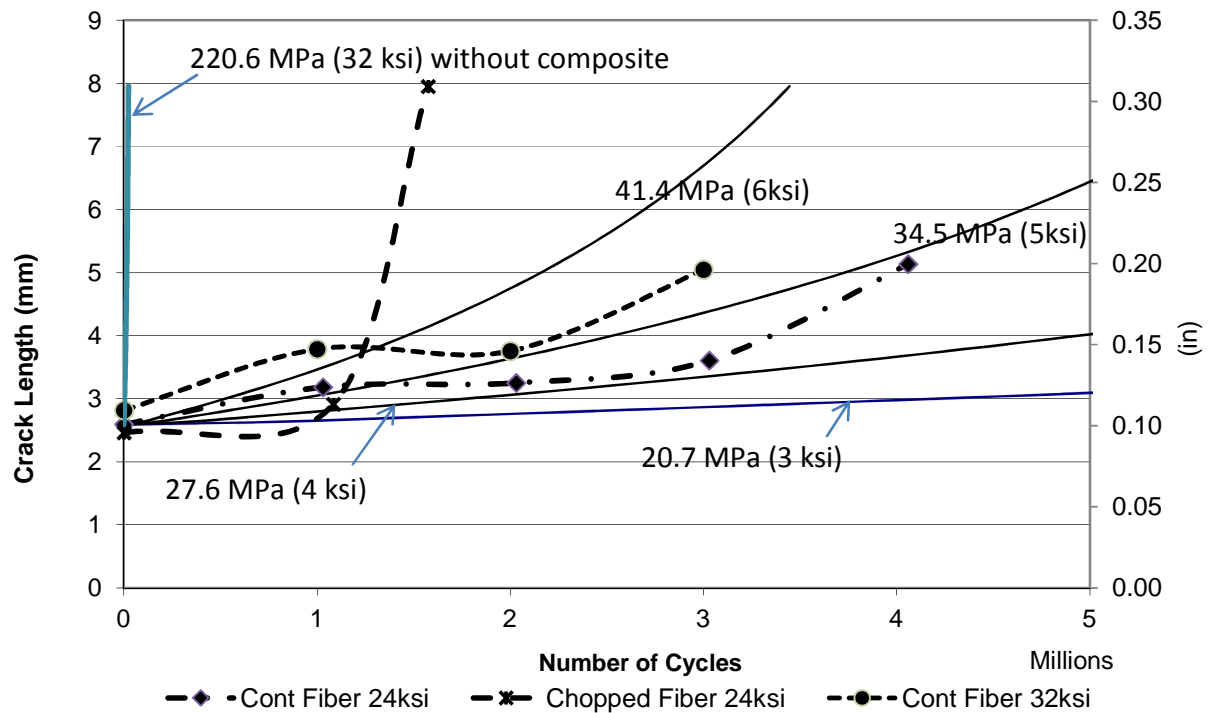
Figure 3-14 : Crack propagation in specimens with CFRP overlays and theoretical values calculated for specimens without overlays

As shown in Fig. 3-14, the crack propagation rate of a specimen repaired with continuous CFRP fibers subjected to a stress range of 166 MPa (24 ksi) was similar to that of an unrepaired specimen subjected to a stress range of 35 MPa (5 ksi) based on theoretical values. These results indicate that the presence of the overlay resulted in a reduction of approximately 80% in the stress range. The test of the specimen repaired with multi-layered CFRP overlay subjected to a stress range of 166 MPa (24 ksi) was stopped after 4 million cycles, after crack growth started to become noticeable. Had the fatigue crack in this specimen continued to propagate at the theoretical rate for an unreinforced specimen under a stress range of 35 MPa (5 ksi), it would have reached a crack length of 7.6 mm (0.3 in.) at approximately 6 million cycles. A similarly

loaded unrepaired steel specimen reached a crack length of 7.6 mm (0.3 in.) at only 50,000

cycles (Fig. 3-13).

The remaining tensile specimens repaired with CFRP overlays, summarized in Table 3-2,

also exhibited a significant improvement in fatigue-crack propagation life. The overlays in these

specimens were not debonded for inspection periodically so that any cumulative damage to the

interface layer due to fatigue could be factored in the test results. The behavior of these

specimens was monitored using the change in stiffness as an indicator of crack growth. The

change in stiffness of all specimens as a function of the number of cycles is shown in Figs. 15-

18.

For all specimens the change in stiffness showed a significant increase in compliance at a

distinct point during testing (Fig. 3-15-18). The maximum stiffness referred to in Eq. 3.2 is a

constant for each specimen, and because testing was performed under load control, the change in

load remained constant. Therefore, according to Eq. 3.2, any decrease in the stiffness (or

increase in compliance) would be a direct result of an increase in the extension of the specimen.

Increases in compliance under a constant load range are caused by softening of the

specimens, which is indicative of damage. An increase in compliance could be caused by loss of

bond, damage in the composite overlays, or a reduction in the net cross sectional area of the steel

specimen. Because the composite overlays showed no signs of damage or distress, except for

specimen F4-25, which will be discussed later, it is hypothesized that gradual increases in

compliance were caused primarily by the reduction of the net cross sectional area of the steel

specimen. Propagation of the fatigue crack through the entire cross section of the specimen led

to 100% of the load being transferred through the composite overlays. This new load path

caused a rapid increase in the damage to the overlays in the vicinity of the fatigue crack and to

74

local loss of bond, leading to a large increase in compliance (or reduction in stiffness) in comparison to that observed during propagation of the crack through the steel. The number of cycles at which a significant change in compliance was observed was adopted as the fatigue propagation life for the specimen.

Upon the conclusion of testing, the CFRP overlays were removed to inspect the steel specimen and it was confirmed that in all specimens shown in Fig.15-18 the fatigue crack had in fact propagated through the entire net section of the steel.
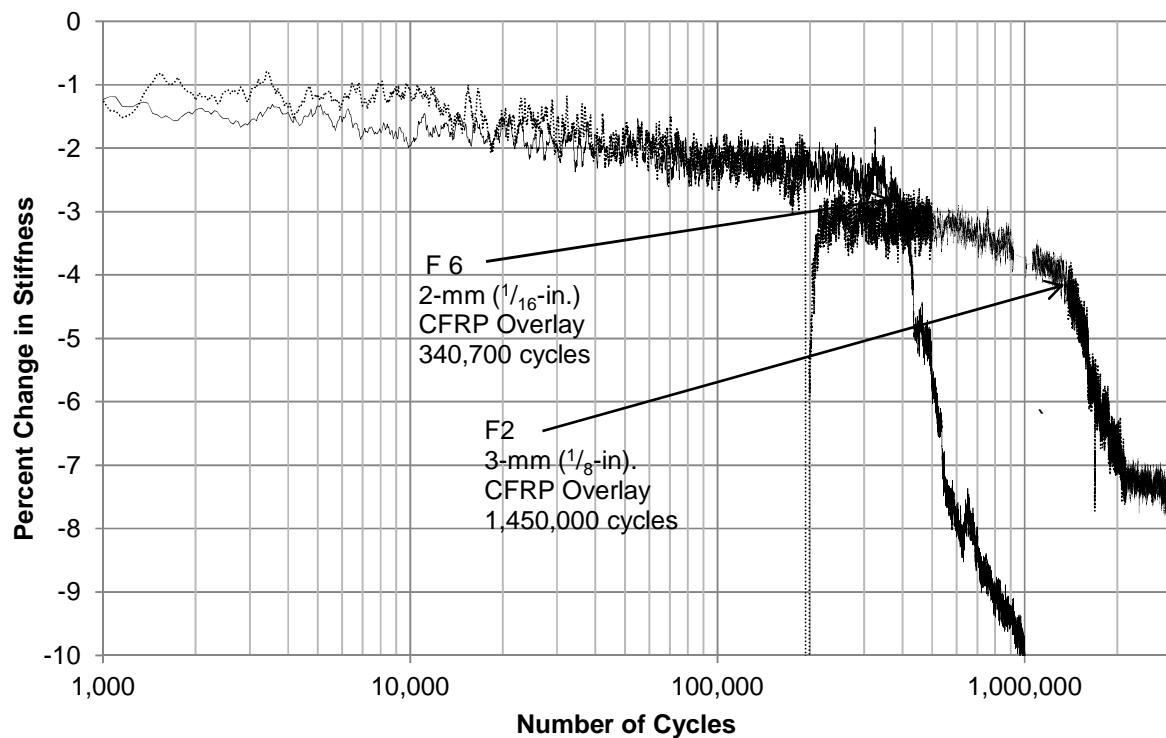
Figure 3-15 : Percent change in stiffness of 3-mm ($^1/_8$-in.) thick specimens tested at 166 MPa (24 ksi)
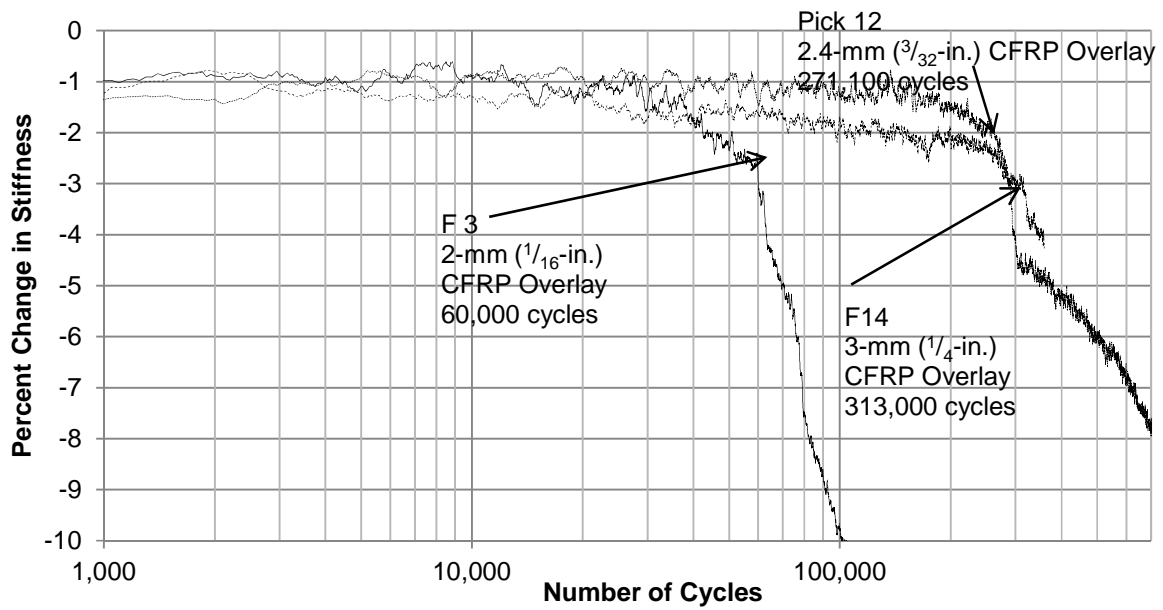
Figure 3-16 : Percent change in stiffness of 3-mm ($^1/_8$-in.) thick specimens tested at 221 MPa (32 ksi)
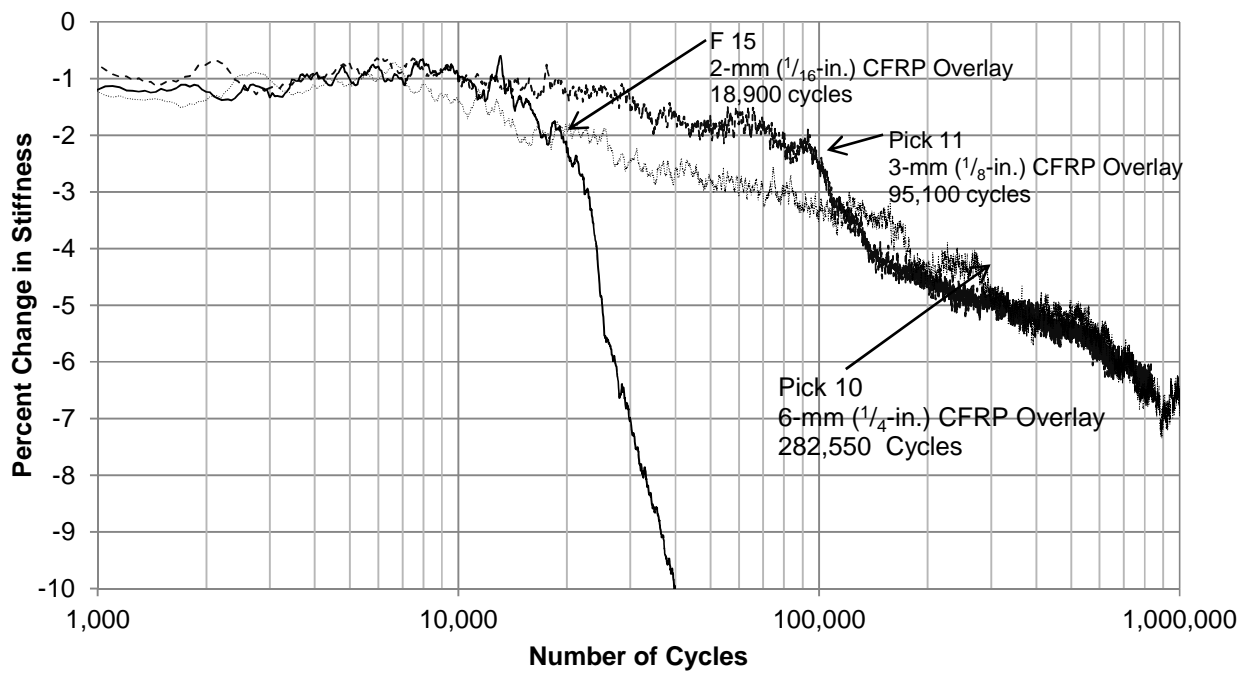
Figure 3-17 : Percent change in stiffness of 3-mm ($^1/_8$-in.) thick specimens tested at 263 MPa (38 ksi)
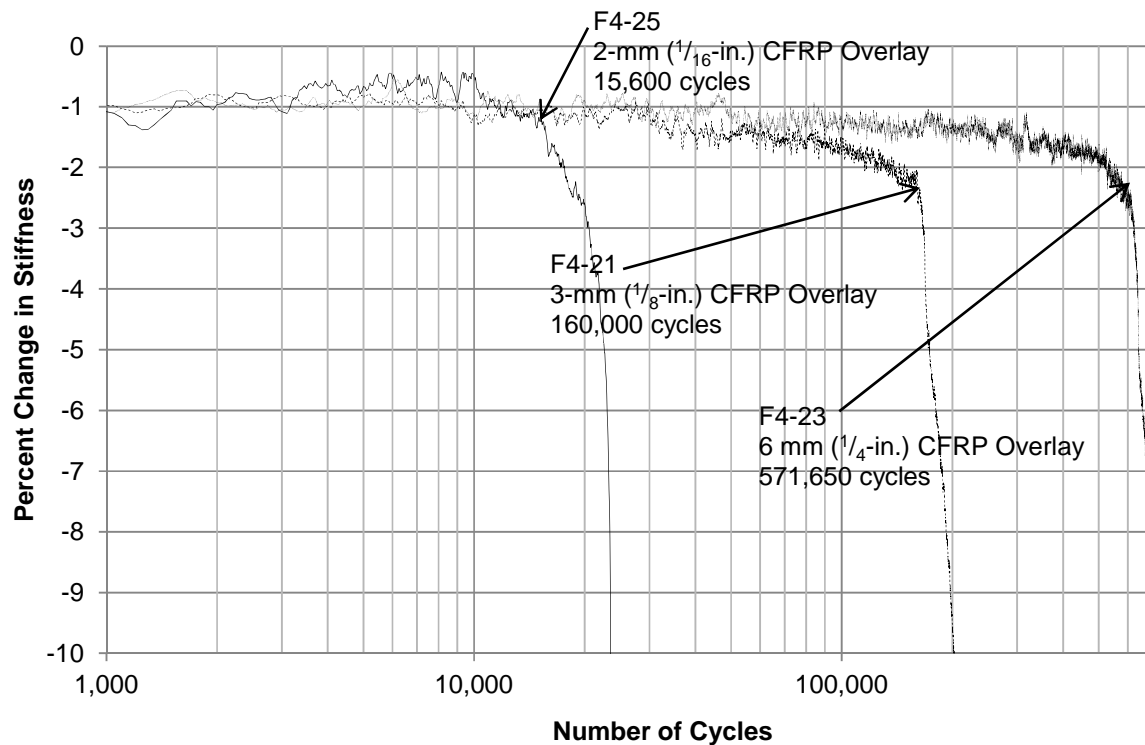
Figure 3-18 : Percent change in stiffness of 6-mm ($^1/_4$-in.) thick specimens tested at 221 MPa (32 ksi)

Of the 14 specimens tested with initial crack lengths of 0.3 in., only one specimen, F4-25, had complete debonding between the steel and CFRP overlays. This is attributed to the combination of thin (2-mm, $^1/_{16}$-in. thick) CFRP overlay and high stress range (221 MPa, 32 ksi). Although there were specimens subjected to a higher stress range (263 MPa, 38 ksi), the steel cross section of specimen F4-25 was 6-mm ($^1/_4$-in.) thick, so the maximum load on the specimen was much higher that the load placed on thinner steel specimens tested at the higher stress range. After full propagation of the fatigue crack through the steel, the higher load demand imposed a higher shear demand on the transfer layer which was attached over the same length in all specimens.

Test Specimens Pick 13, Pick 7 and F4-20 were not included in Fig. 3-15, 3-18. For these three specimens a significant change in compliance was never observed after the number of cycles exceeded the infinite fatigue threshold corresponding to the nominal stress range established in the AASHTO bridge specifications (AASHTO 2004). The stress reduction in the steel due to the alternate load path provided by the CFRP overlay was sufficient to drive the demand below the fatigue-crack-propagation threshold (Barsom and Rolfe, 1999) as shown in Fig. 3-19. After the number of cycles associated with infinite fatigue life in the AASHTO LRFD Bridge Design Specification (2007) was surpassed in these three specimens, the composite overlays were removed for inspection and it was confirmed that the fatigue crack had not propagated fully through the steel cross section.

Figures 19 and 20 show the fatigue-propagation life for all specimens summarized in Table 3-2. S-N curves for the various fatigue categories in the AASTHO Bridge Specifications (AASHTO 2007)are presented for reference. For specimens that were 3-mm ($^1/_8$-in.) thick (Fig 19), doubling the thickness of the CFRP increased propagation life approximately by the number of cycles corresponding to one AASHTO fatigue category. For specimens that were 6-mm ($^1/_4$-in.) thick (Fig. 3-20), doubling the thickness of the CFRP increased propagation life approximately by the number of cycles corresponding to two or more AASHTO fatigue categories. Regardless of the thickness of the steel, all specimens with CFRP overlays with a thickness of 6.4 mm ($^1/_4$ in.) had fatigue-propagation lives exceeding the initiation life of a Category B detail.
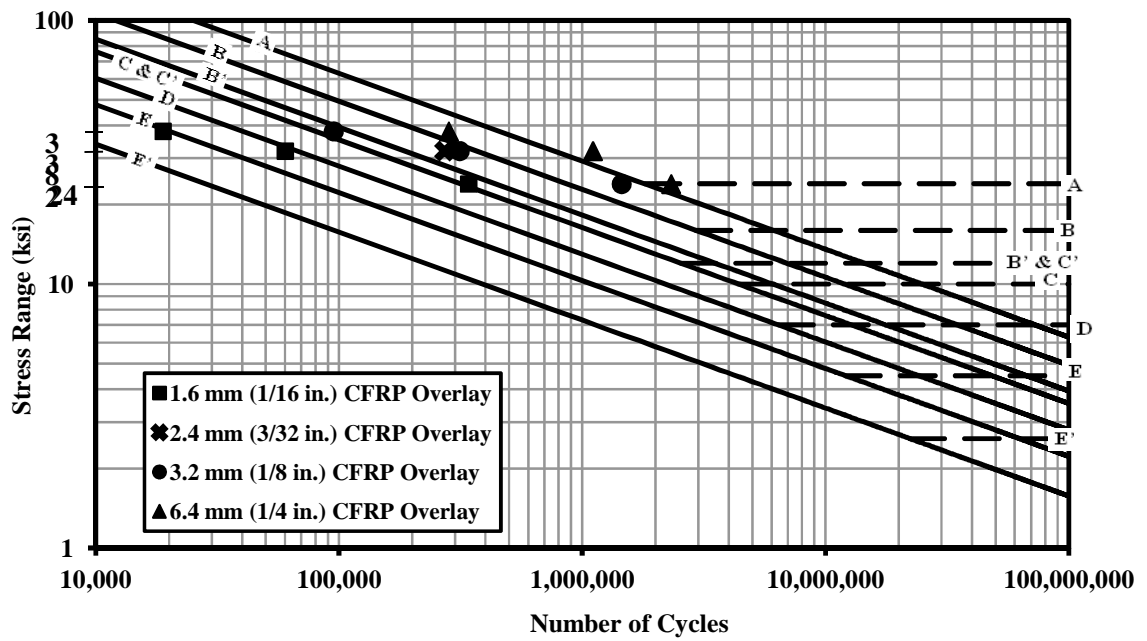
Figure 3-19 : S-N diagram for 3-mm ($^1/_8$-in.) thick specimens showing fatigue-crack propagation life
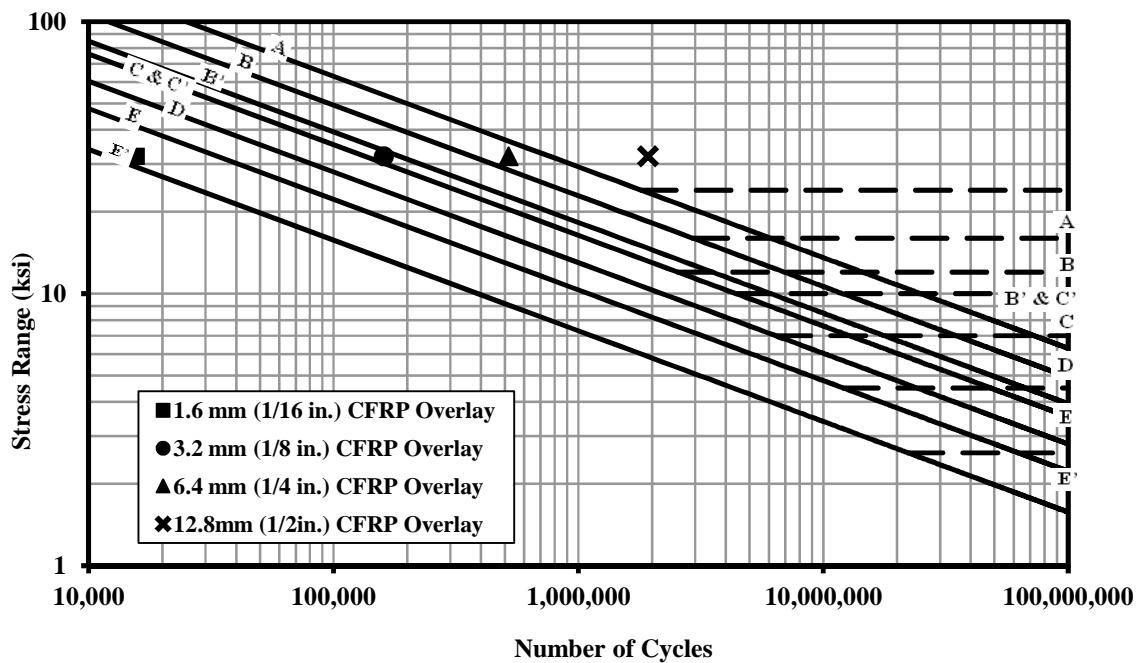
Figure 3-20 : S-N diagram for 6-mm ($^1/_4$-in.) thick specimens showing fatigue-crack propagation life

The fatigue-crack propagation life of all specimens with a pre-existing fatigue crack of 7.6 mm (0.3 in.) that were repaired with continuous-fiber CFRP overlays and were subjected to a stress range of 221 MPa (32 ksi) is summarized in Table 3-1. In all cases, the propagation life of the specimens was greater than 3 million cycles. At this point the test was stopped after noticing measurable crack growth. The comparison between unrepaired and continuous-fiber CFRP repaired cases shows that the fatigue-crack propagation life of continuous-fiber CFRP repaired specimens was more than 50 times greater that the propagation life of unreinforced specimens. The repaired specimen subjected to a stress range of 221 MPa (32 ksi) had a nominal maximum stress of 235 MPa (34 ksi), which was close to the measured yield stress of 303 MPa (44 ksi) for the steel. The results show that the behavior of the continuous-fiber CFRP repaired specimen was similar to that of an unrepaired specimen subjected to a nominal stress range between 35 (5 ksi) and 41 MPa (6 ksi), which indicates that the CFRP repair was very effective at that high stress range as well.

The experimental fatigue-crack propagation curves shown in Fig. 3-14 also indicate that rate of crack growth in repaired specimens had a greater tendency to increase with crack size than the theoretical relationship for unreinforced specimens (Eq. 3.3). This could be an indication that as the fatigue crack grows, the bond between the composite and the steel in the area surrounding the crack is reduced, making the repair less effective. It is hypothesized that this detrimental effect could be lessened by drilling a hole at the tip of the crack, to remove the sharp crack tip and the process zone. The combination of the stress reduction due to the alternate load path provided by the composite and the repair of the tip of the crack may be sufficient to

drive the stress demand below the fatigue-crack-propagation threshold (Barsom and Rolfe, 1999). This is a combination of techniques that warrants future study.

Average crack propagation rates are presented in Table 3-5. The experimental curves were divided into two regions. During early fatigue crack growth the propagation rate was nearly constant. Average rates of crack growth for the nearly constant region are presented in the third row of Table 3-3. After significant crack growth, the crack propagation rate increased as the specimens approached failure and, in the case of specimens with overlays, the bond between the overlay and the steel degraded. The values in Table 3-5 show that for specimens with a stress range of 166 MPa (24 ksi) the effect of the overlays was to decrease the crack growth rate by a factor of approximately 45, and the reduction in the rate of crack growth was similar for both types of composite overlays. For the specimen subjected to a stress range of 221 MPa (32 ksi), the bonding of the overlays resulted in a reduction in the crack growth rate by a factor of approximately 300.

Table 3-5 : Average crack propagation growth rates

$\Delta\sigma$ *MPa (ksi)*	166 (24)	221 (32)	166 (24)	166 (24)	221 (32)
Type of Overlay	None	None	Multi-Layered	Chopped Fiber	Multi-Layered
Average Crack Propagation Rate, Stable growth, μ m/cycle (μ in./cycle)	0.0147 (0.58)	0.1575 (6.19)	0.00025 (0.01)	0.0005 (0.02)	0.0005 (0.02)

The final goal of this study was to determine the relative fatigue life improvements of CFRP with varying stiffness ratios according to Eq.3.1. The modulus of elasticity of the CFRP overlay was taken to be 83 GPa (12,000 ksi) regardless of overlay thickness, as mentioned in Section 4. The stiffness ratio was determined base on the measured thickness (t) of the steel and

CFRP overlays, and the modulus of elasticity of steel (200 GPa, 29,000 ksi). Fig 21 shows the fatigue-crack propagation life of each specimen vs. the stiffness ratio. For specimens that reached infinite fatigue life, the number of cycles to failure was extrapolated using accepted models of theoretical crack propagation presented by Barsom and Rolfe (1999).

Figure 3-21 shows that for a specific stiffness ratio, as the stress range at which the specimen was tested increased the fatigue life decreased, as expected. However, this trend was not proportional. A much greater improvement was observed when the stress range decreased from 221 MPa (32 ksi) to 166 MPa (24 ksi) than when the stress range decreased from 263 MPa (38 ksi) to 221 MPa (32 ksi).

Figure 3-21 also shows a bilinear relationship between propagation life and the stiffness ratio. For each stress range there was a stiffness ratio at which the slope of the curve had a sudden increase, trending towards infinity. Past this point, small increases in the stiffness ratio resulted in propagation lives that vastly exceeded the infinite life threshold in the AASHTO specifications (AASHTO 2004). It is clear from Fig.21 that the critical stiffness ratio at which each set of data trended towards infinity increased with the stress range. The critical stiffness ratios for specimens tested at stress ranges of 166 MPa (24 ksi) and 221 MPa (32 ksi) were approximately 0.8 and 1.0 respectively. These results indicate that as the stress range increases, the stiffness ratio must be increased in order to achieve infinite fatigue life. According to Eq.3. 2 the thickness of the steel specimen should not have any effect on fatigue-crack propagation life shown in Fig. 3-17. Because the critical width of the 6-mm (¼-in.) thick specimens differed from that of the 3-mm ($^1/_8$-in.) thick specimens, failure of the former specimens was taken as the number of cycles at which the crack reached a length of 14 mm ($^9/_{16}$ in.). Therefore, the propagation life used in the comparisons corresponds to the same crack growth for all specimens,

82

regardless of specimen size, allowing a direct comparison between the two. A direct comparison

between the 3-mm ($^{1}/_{8}$-in.) thick and the 6-mm (¼-in.) thick specimen tested 221 MPa (32 ksi) in

Fig. 3-21, shows that for the same stiffness ratio the thicker specimen had the larger propagation

life. However, both specimens had approximately the same critical stiffness ratio.
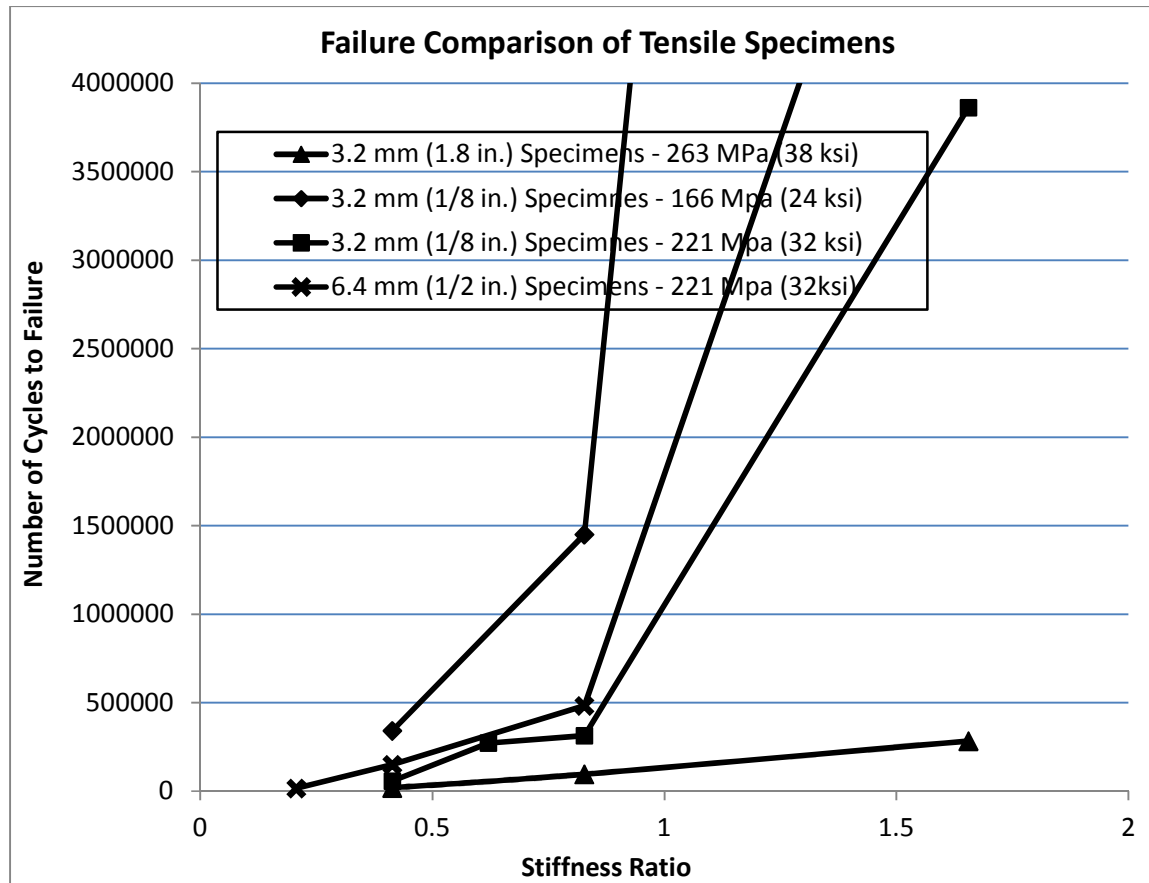
Figure 3-21 : Fatigue-crack propagation life for all specimens treated with CFRP overlays and an initial crack length of 7.7 mm (0.3 in.)

Conclusions

The results of the experimental and analytical studies on the use of CFRP overlays to repair fatigue cracks in steel plates resulted in the following conclusions:

- Experimentally observed reductions in stress range demand associated with the bonding of overlays were consistent with those observed in FE simulations.

- Experimental results showed that bonding of pre-fabricated multi-layered CFRP overlays extended the fatigue-crack propagation life of the steel specimens by more than 50 times. The observed increase in fatigue-crack propagation life was significantly higher than values ranging between 4.7 and 7.9 reported in previous studies on aluminum plates, steel plates, and steel beams. The main difference between the overlays used in this study and those used in other studies found in the literature is that the stiffness ratio *SF* was significantly higher.

- Experimental results showed that as the stress range was increased, a larger stiffness ratio was needed for the specimen to reach infinite fatigue life. At 166 MPa (24 ksi) and 221 MPa (32 ksi), the number or cycles to failure tended towards infinity at a stiffness ratios of 0.8 and 1.0 respectively.

- Computer simulations showed that the parameters that have the most significant effect on fatigue-crack propagation life were the modulus of elasticity of the CFRP and the thickness of the overlay.

- Maintaining adequate bonding between the CFRP overlay and the steel is critical. Significantly better performance was obtained by using a high-quality bonding resin over direct spraying of the composite on the steel.

- Although the increase in fatigue-crack propagation life was less for the sprayed overlay, the increase was on the order 30 times the propagation life of an unreinforced composite.

The research conducted showed that use of CFRP overlays to repair cracks in steel members can be a highly effective means of reducing the stress demand and greatly prolonging the fatigue-crack propagation life. This technique can be used with the goal of avoiding the need for drilling large-diameter crack-stop holes. When composite overlays are used in combination with crack-stop holes, the overlay can effectively reduce the stress demand, allowing the use of crack-stop holes with a much smaller diameter, sufficient to only to remove the tip of the crack and the fracture-damaged zone.

References:

AASHTO, L. 2007. Bridge Design Specifications (2007). *American Association of State Highway and Transportation Officials*.

ASTM, D. 2000. 3039/D 3039M,". *Standard Test Method for Tensile Properties of Polymer Matrix Composite Materials*.

Lee, W. Y., and J. J. Lee. 2004. Successive 3D FE analysis technique for characterization of fatigue crack growth behavior in composite-repaired aluminum plate. *Composite Structures* 66 (1-4):513-520.

Liu, H. B., R. Al-Mahaidi, and X. L. Zhao. 2009. Experimental study of fatigue crack growth behaviour in adhesively reinforced steel structures. *Composite Structures* 90 (1):12-20.

Liu, H. B., Z. G. Xiao, X. L. Zhao, and R. Al-Mahaidi. 2009. Prediction of fatigue life for CFRP-strengthened steel plates. *Thin-Walled Structures* 47 (10):1069-1077.

Mall, S, and DS Conley. 2009. Modeling and validation of composite patch repair to cracked thick and thin metallic panels. *Composites Part A: Applied Science and Manufacturing* 40 (9):1331-1339.

Mall, S., and D. S. Conley. 2009. Modeling and validation of composite patch repair to cracked thick and thin metallic panels. *Composites Part a-Applied Science and Manufacturing* 40 (9):1331-1339.

Marquis, G, and A Kaehoenen. 1995. Fatigue testing and analysis using the hot spot method.

Naboulsi, S, and S Mall. 1996. Modeling of a cracked metallic structure with bonded composite patch using the three layer technique. *Composite Structures* 35 (3):295-308.

Sabelkin, V, S Mall, and JB Avram. 2006. Fatigue crack growth analysis of stiffened cracked panel repaired with bonded composite patch. *Engineering Fracture Mechanics* 73 (11):1553-1567.

Schubbe, JJ, and S Mall. 1999. Modeling of cracked thick metallic structure with bonded composite patch repair using three-layer technique. *Composite Structures* 45 (3):185-193.

Tavakkolizadeh, M, and H Saadatmanesh. 2003. Fatigue strength of steel girders strengthened with carbon fiber reinforced polymer patch. *Journal of Structural Engineering* 129 (2):186-196.

Umamaheswar, TVRS, and R Singh. 1999. Modelling of a patch repair to a thin cracked sheet. *Engineering Fracture Mechanics* 62 (2-3):267-289.

ABAQUS, Version 6.8-2, Simulia, 2009, http://www.simulia.com.

Barsom, J.M., and Rolfe, S.T. (1999). "Fatigue and fracture behavior of welded components." *Fracture and Fatigue Control in Structures*, 3rd ed., (10), American Society for Testing and Materials, West Conshohocken, PA, 35-53.

Roy, M., Lang, C., & May, I. (2009). Modelling composite repairs to cracked metal structures. Proceedings of the Institution of Civil Engineers. *Structures and Buildings*, 162(2), 107-113.

Hysol® 9412, Loctite 9412 Hysol Epoxy Adhesive, 2001, http://www.henkelna.com.

CHAPTER 4. FINITE ELEMENT MODELING TECHNIQUES FOR ESTIMATING FATIGUE CRACK PROPAGATION IN STEEL BRIDGE GIRDERS

Abstract

This paper describes finite element modeling techniques used to evaluate the potential for fatigue cracks in steel girders subjected to distortion-induced fatigue. The modeling techniques employed in this study were intended to identify areas near welded connections in bridge girders with the highest potential for developing fatigue cracks, and to evaluate the effectiveness of retrofit measures in reducing the potential for crack propagation near welded connections with existing fatigue cracks. Because of the complex stress fields associated with distortion-induced fatigue areas susceptible to this type of damage in girders are subjected to 3D mixed-mode fracture.

Computer simulations were performed using the analysis program ABAQUS 6.10. Modeling techniques employed in this study included the extended finite element method (X-FEM), used for simulating existing cracks and for investigating crack propagation paths, and for quantifying the potential for crack propagation in terms of the J-integral. Other tools used to quantify the potential for fatigue damage include the Hot Spot Stress (HSS).

Results from computer simulations were compared with experimental measurements from 9-ft long steel girder assemblies subjected to out-of-plane cyclic loading. The girders had typical connection plate-to-girder web connections found in bridges with documented damage due to distortion-induced fatigue. The girder sub-assemblies were evaluated in their original and

retrofitted conditions. Retrofit measures studied computationally and experimentally include bolted steel angles, plates, and composite blocks.

The modeling techniques implemented in the study were very effective in identifying locations where fatigue cracks developed in the girder sub-assemblies. The HSS technique provided an adequate measure of the potential for fatigue cracks, while computed values of the J-integral provided were good indicators of the potential for crack propagation in retrofitted specimens.

Introduction

Fatigue damage affects steel bridges in areas with very complex stress fields often induced by abrupt changes in geometry brought about by connections between structural components. Given the level of complexity involved in simulating the flow of forces in these areas the finite element method is one of the best analytical tools available to quantify the stress demands and investigate the potential for fatigue damage. The main difficulty associated with using the finite element method is that the results are sensitive to the approach followed in developing the model. Important assumptions and modeling decisions such as the density of the mesh, the material models, and the presence of thermally-induced residual stresses have a significant effect on the outcome of the analysis. Furthermore, the computational effort required to carry out a simulation of this kind is significant and increases with the level of complexity of the model.

The study presented in this paper was carried out with the goal of identifying modeling techniques that can be used to quantify the potential for fatigue-crack initiation and propagation in a reliable manner. The simulations were performed in the specific context of distortion-induced fatigue in steel girders, which is particularly complex because areas of the girders susceptible to fatigue damage are subjected to mixed-mode fracture. Emphasis was placed in using simple modeling techniques because increasing complexity in models corresponds with greater sensitivity to modeling assumptions, requires more sophisticated computer platforms, and longer run-time requirements.

While the focus of this paper was on describing and evaluating computer simulation techniques for distortion-induced fatigue, it was essential to have data from physical simulations

to validate the simulation results. A 2845-mm (112-in.) long steel girder subassembly was loaded through a cross brace under cyclic loading to study the formation and growth of fatigue cracks under distortion-induced fatigue and to evaluate the effectiveness of various retrofit measures to prevent the propagation of existing fatigue cracks. The girder sub-assembly was loaded "upside down", with the top flange of the girder fixed to the reaction floor of the laboratory. Because the test configuration restrained the girder from bending, the loading conditions were representative of a bridge girder in a location near the inflection point of a bridge.

Objective

The objective of this study was to evaluate accuracy of computer modeling techniques used to simulate the stress field in steel girders subjected to distortion-induced fatigue. Modeling techniques were evaluated by verifying that the computed stress fields could be used to identify locations with the highest likelihood of developing fatigue cracks, and used to quantify the effectiveness of various retrofit measures in reducing the rate of growth of existing fatigue cracks.

Scope

This study involves exploring and assessing simulation techniques in the context of bridge girders subjected to distortion-induced fatigue. The goal of the study was to calibrate finite element models of areas with high stress demands by comparing calculated stresses with experimentally observed crack patterns and measured values of stress. The calibrated models were subsequently used to provide an indication of whether various retrofit measures can be expected to perform effectively under field conditions.

Background

Distortion-Induced Fatigue

Fatigue cracks due to distortion-induced fatigue have been identified in many welded steel bridges built prior to the mid-1980s.   Bridges from this period often included cross frames or diaphragms attached to transverse stiffeners, which were welded to the web of the girders. The stiffeners were not connected to the tension flange due to concerns about the potential for fatigue damage, and sometimes were not connected to compression flanges either. When a live load is placed closer to one girder than another, the two girders deflect vertically in different amounts. The differential deflection causes the cross frames or diaphragms to introduce secondary stresses at the connections with the girders, giving rise to the phenomenon of distortion-induced fatigue (Fisher, 1984).

In these bridges, cracks form mostly in the negative moment region because the concrete deck provides some restraint from lateral motion in the positive moment region and many times the connection plate or stiffener is welded to the top flange. Cracks originate at the toe of the welds connecting the web and flange and also at the toe of welds connecting the web to the stiffener.

Previous Retrofits

Repairing cracks in the web gap can be done in two ways. The first is to increase the compliance of ("soften") the connection in order to reduce the stress demand. Softening of the connection will either reduce the distribution of forces between girders, or cause the system to find alternative paths to transfer the load between girders. New load paths are likely to engage connections with higher stiffness, which may cause the fatigue problem to migrate from one

location to another. The second approach is to stiffen the region by providing an alternate load path at the connection, which has the effect of reducing the deformations in the web gap region and consequently the stress demand. Zhao and Roddis (2007) studied both of these repair methods on a two-girder bridge near Manhattan, Kansas. High-resolution finite element models were created which showed that stresses in the top web gaps exceeded the yield point when an HS-15 fatigue truck was placed on the bridge. The softening repair method involved slotting the connection plate, and the simulation results showed that not only were cracks expected to reinitiate, but stresses in the top web gap also increased. According to Fisher (1984), in order for the slotted repair to work, the minimum removal length must be at least 305 mm (12 in.) or 20 times the thickness of the web. The other repair studied by Zhao and Roddis consisted of welding the connection plate to the flange. With this method, peak stress demands were reduced on the order of 90%, without forming new stress risers.

Crack Models

The *J*-Integral and stress intensity factors (SIF) are used in cracked models to quantify the potential for crack growth (Zhu et al., 2010). SIFs can be determined with accuracy by using the scaled boundary finite element method (SBFEM).   From there, the *J*-Integral can be converted from K_I and K_{II} for mixed-mode cracks.

Cook et al. (2002) explain that ABAQUS always calculates the *J*-Integral as positive. Looking at nodal displacements at the corners of the cracks will tell if a crack is opening or closing in a given direction. If the opening displacement is positive, then the crack is opening and the *J*-Integral is positive. The opposite is true as well.

Modeling Techniques

Material Properties

All materials modeled were isotropic and linear elastic. The modulus of elasticity for the steel was set to 200,000 MPa (29,000 ksi) and Poisson's ratio was set at 0.3. The density of steel used was 76.0 kN/m^3 (490 lb/ft^3). Young's modulus for the concrete was 27,780 MPa (4,030 ksi) and Poisson's ratio was set to 0.2. Composite blocks used in retrofit simulations had a modulus of elasticity of approximately 2×10^6 MPa (300,000 ksi) and Poisson's ratio of 0.1.

Mesh

The three-dimensional finite element model was created using ABAQUS 6.10. The elements used for the web were 8-node brick elements with 24 degrees of freedom. The mesh in the web was denser in the bottom and top web gaps where cracks will form in comparison to the other locations. Denser meshes increase the accuracy of the model in areas where the stress gradient is large, although at the cost of increased run time. The smaller mesh size in the bottom web gap was 2.5 mm (0.1 in.) and 9.5 mm (0.38 in.) outside of this area. Tetrahedral elements were used to transition between these two mesh sizes.

Boundary Conditions

The beam subassemblies were attached to the concrete floor through steel channels. In the simulation, both the concrete floor and the channels were modeled. Both ends of the subassembly were connected to the reaction frame through channels running perpendicular to the girder. In early simulations bolts and threaded rods were modeled explicitly, while in later simulations tie constraints were used instead to reduce computational time without any meaningful change in the calculated stress field at the web gap.

Angles were attached to both ends of the top flange to provide some lateral and torsional restraint to the girder, in the same manner that the flange would restrain the motion of an actual girder.

The actuator was defined as free to move up and down. Cross-frame elements were attached to the actuator through a WT10.5x27.5 with tie constraints. Cross- frame elements were connected to the girder specimen with bolts. Bolt simulation techniques are explained below.

Load

In the load-controlled model, a 22.2 kN (5 K) tension load was applied over the cross sectional area of the actuator in the loading step.

Welds

The web-to-flange and cross frame plate-to-web connections were modeled with 4.7-mm (0.19-in.) fillet welds. Tie constraints were used to connect the fillet welds to the girder and gusset plate. The welds were modeled as right triangles and each consisted of hexagonal 8-node brick elements with a mesh size of 2.5 mm (0.1 in.).

Bolts

Bolts with a diameter of 19 mm ($^{3}/_{4}$ in.) were modeled by merging one end of a shank with the head and the other side with the nut. Threads on the bolts were not modeled explicitly. The middle of the shank was partitioned so that an interior surface was present. An intermediate loading step was created in which a bolt load was applied to the interior face of the shank to simulate the tension force in the bolts.

Crack Modeling Techniques

A. Explicit Modeling

Cracks were first simulated in the model by removing a thin section of elements in the web. The mesh density in the bottom web gap area was very dense (0.023 in.) so that when the elements were removed, the crack would be as thin as possible. The crack was one element thick, or 0.6 mm (0.023 in.). Results showed that the magnitude of the stresses calculated in this manner was sensitive to mesh density. By removing elements in the web, the cracks were neither allowed to grow nor initiate. Other useful information pertaining to the potential of the crack to grown such as the *J*-Integral and Stress intensity factors could not be determined with this technique.

B. X-FEM

The second method for modeling cracks utilized the eXtended Finite Element Method (X-FEM). Cracks were modeled as zero-thickness 3-D planar shells. Because the crack part had no thickness, the accuracy was slightly greater than when elements were removed. Cracks were through-thickness cracks in the web so the width of the crack was 9.5 mm ($^3/_8$ in.). Crack lengths and locations were selected to be similar to those observed in the physical simulations of the subassemblies. Cracks were modeled as stationary and were also allowed to grow. Parts that contained cracks that are allowed to grow must have an additional parameter in the materials module. This parameter specifies when a crack if crack growth will take place based on one of six different failure criteria in terms of stress or strain, and also the displacement at failure. The failure criterion used in the simulations was based on the maximum principal stress and the failure stress was set as 276 MPa (40 ksi). Displacement at failure was set to 0.25 mm (0.01 in.).

C. Contour Integrals

The last method used to model cracks was based on contour integrals. The results of this method were more sensitive to mesh size than the results obtained with the X-FEM. Cracks were simulated according to the following method. First, the section that contained the crack was partitioned so that a crack location could be chosen from one of the partitions.   Next, the crack direction was specified by utilizing q vectors. The start coordinate of the q vector was specified as the end of the crack that was not propagating, and the end coordinate of the q vector was specified as the crack tip. Finally a seam was created in the same special section of the Interaction Property Module.

D. Cohesive Behavior vs. LEFM

There are two methods to model cracks in ABAQUS CAE, traction-separation cohesive behavior and linear elastic fracture mechanics (LEFM). Both methods can model crack propagation and are equally suited for modeling delamination. If a crack is not initially present, initiation can only be modeled through the traction-separation cohesive method. After initiation has occurred, LEFM can be used to model propagation.   The two methods cannot be used in conjunction to model identical crack behavior.   For example, properties for the cohesive method and LEFM cannot both be specified to model crack propagation. The cohesive method is an energy and strength criterion, while the LEFM is not (Chen and Mai, 2010). The results of LEFM are generally similar to the cohesive method.

In the cohesive method, damage evolution properties are specified for the material undergoing cracking. In this method it is assumed that failure of the cohesive bond is characterized by progressive degradation of the cohesive stiffness, which is driven by the

97

damage process (ABAQUS 6.10, 2010). The damage evolution property is based on the choice

of six stress or strain criteria.

1. Maximum principal stress (MAXPS)

2. Maximum principal strain (MAXPE)

3. Maximum nominal stress (MAXS)

4. Maximum nominal strain (MAXE)

5. Quadratic traction-interaction

6. Quadratic separation-interaction

The damage evolution components specified describe how the material will displace after

the maximum stress or strain is reached. The relationship between the damage evolution

property and displacement can be linear or nonlinear as shown in the figure below. For damage

evolution properties based on stress, the maximum cohesive traction, T_{max}, is the failure

parameter that defines the initiation or propagation of the crack. In the 9-ft specimen models, a

maximum principal stress criterion was chosen with a cohesive traction of 276 MPa (40 ksi) and

a maximum displacement of 2.5 mm (0.1 in.) was used as the damage evolution properties.
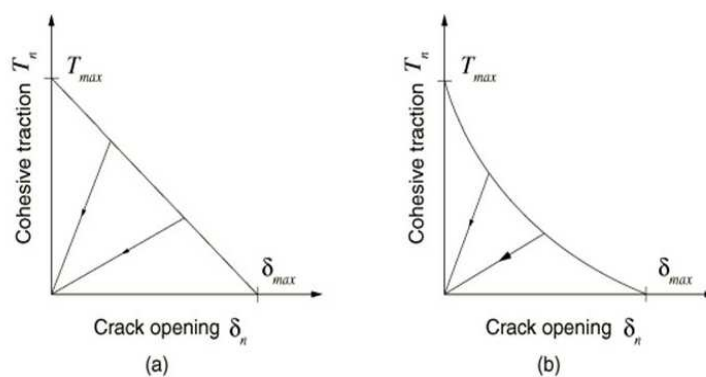
Figure 4-1: Traction separation response a) linear b) nonlinear

The LEFM method relies on the modified Virtual Crack Closure Technique (VCCT) to calculate the strain energy release rate at the crack tip. This method is more appropriate for brittle fractures along predefined surfaces (ABAQUS 6.10, 2010). In this method, failure occurs only at the crack tip.

The main properties of the LEFM method are specified in the Fracture Criterion in the Interaction Properties. A mixed-mode fracture criterion must be specified, and ABAQUS gives three choices: Benzeggagh-Kenane (BK), Power, and Reeder (ABAQUS 6.10, 2010). This criterion is used to estimate the onset and the angle at which the crack grows. In the BK and Reeder criterions, Mode I, II, and III critical energy release rates are chosen, and in the Power criterion additional exponents must be chosen. LEFM can only be used if a crack is pre-existing or will be nucleated during the analysis. If there is no crack, then it is initiated by using one of the six stress or strain criteria specified in the material properties.

If CFRP is modeled, the cohesive method combines the stress analysis and the debonding simulation, whereas in the LEFM method, these two steps are separate. In LEFM, the first step is to calculate stress and displacement. In the second step, these results are used to determine the stress intensity factors or the energy release rate. A crack will propagate when the energy release rate, G (calculated using the J-integral), is larger than the critical fracture energy, G_c. Because the LEFM method assumes linear behavior, the amount of work the computer must do is considerably less than with the cohesive method. The parameters that must be specified for the LEFM are less than in the cohesive method. There are many variables that can be specified in the LEFM, but only G_c is needed for fracture simulation (Rabinovitch, 2008). Because very little information is required for LEFM, the cohesive method can be more accurate for some debonding simulations. Overall, the two methods showed similar results.

Modeling of Retrofit Measures

Connectivity

Tie constraints were used to transfer stress and strain from the master surface to the slave. Sliding and entering into other parts was prevented by applying tie constraints which provided full connection between nodes. Load transfer from the actuator to connecting elements was kept in mind when selecting master and slave surfaces. For example, cross-frame elements were specified to be slave surfaces to sections of the WT, which was the first part subjected to the actuator loading. Model run time was optimized when both the slave and master surfaces were partitioned to be the same size and also when the master surface had a coarser mesh than the slave.

When more accuracy was required, interactions were used to allow parts to slide against each other. An interaction property was created which specified a surface-to-surface penalty hard contact and friction coefficient of 0.35 in the tangential and normal directions. Interactions were used between the angle, web, and shims in the angle retrofit to prevent the parts from entering each other and to allow for friction. Another interaction was created in the top web gap where the top of the connection plate was not welded to the top flange.

Measuring Fatigue Damage Potential

Peak Stress

The location of the peak stress throughout the model was different for the various crack and retrofit configurations. When there were no cracks or retrofits, the maximum stress overall was found at the weld connecting the cross-frame gusset plate to the web in the bottom web gap.

Maximum calculated stresses at the web and connection plate weld in the bottom web gap region exceeded the yielding stress of the steel.

### *Directional vs. Principal vs. Von Mises Stresses*

Different stress types, including directional, Maximum Principal, Von Mises, and Tresca, were evaluated to find which one provided the best indication of the crack locations in the girder subassemblies. Figure 4-3 shows that crack growth followed the direction of the peak maximum principal stress.

Hot Spot Stress Technique

The hot spot stress technique was used to quantify the stress demand in the web, near the toe of the fillet welds. The stress was monitored at a distance away from the toe of the welds equivalent to 0.5 times the thickness of the web, which was rounded to 5 mm (0.2 in.). Hot spot stress path #1 - bottom was a horseshoe shaped path approximately 102-mm (4-in.) long. This path was located in the bottom web gap on the interior face of the web. Hot spot stress path #2 - bottom was a 203-mm (8-in.) long horizontal path following the weld connecting the web to the bottom flange. Similar hot spot stress paths were extracted from the fascia side of the web in the top web gap. Hot spot stress path #1 – top was 101-mm (4-in.) long on the fascia side of the web in the top web gap. Hot spot stress path #2 – top was a 57-mm (2.25-in.) long horizontal path following the weld connecting the web to the top flange. The length of the paths was similar to the length of cracks measured in the girder subassemblies. By following this approach, stress demands calculated using uncracked models could easily be compared with stress demands computed using models that had cracks.

J-Integral and Stress Intensity Factors

The potential for crack growth was evaluated by comparing computed values of *J*-Integrals and stress intensity factors (SIFs) for contours surrounding crack tips in addition to the hot spot stress technique. The algorithms in ABAQUS only allow calculating these parameters for stationary cracks. Smaller models were made which consisted of a single plate with a crack half the length of the plate (Fig. 4-2). A 6.89 MPa (1 ksi) compression and tension pressure load was applied to the left and right sides of the plate to study how opening or closing of a crack affects the sign of the *J*-Integral and SIFs. In the model, a surface-to-surface interaction was placed between the both sides of the crack to prevent them from entering each other. From this smaller model, it was found that when loading causes a crack to close, SIFs become negative, and when the crack opens, SIFs stay the same magnitude, but opposite in sign. The *J*-Integral changed values, but the sign stayed positive.
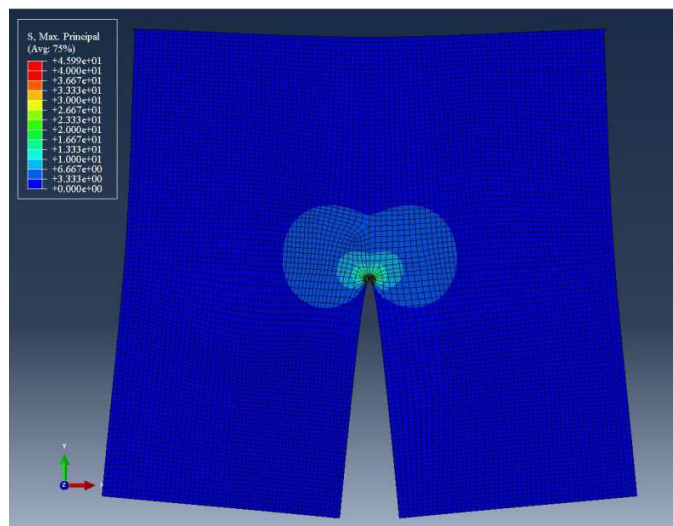

Figure 4-2 Focused mesh surrounding crack tip in a 3-dimensional model.

Parts that contained cracks had circles partitioned at the tips of cracks to define the contours. The *J*-Integral and SIFs were specified as separate history outputs generated at the end of the loading step. In the history output, the number of contour integrals was specified as 5. The accuracy of the *J*-Integral and SIFs increases as the contours move away from the crack tip. Therefore, data was read for the 4th and 5th contours, and the others were disregarded.

Comparison between FEA and Experimental

The simulation results were consistent with the results from the physical simulations. In previous studies on distortion-induced fatigue very little material was found indicating which type of stress indicator provides the best match for the location of fatigue cracks. As previously discussed, several types of indicators were evaluated in this study to identify the one that provided the best match to experimental results. Comparisons between computer and physical simulations showed that cracks in the girder subassemblies followed the maximum principal stress distribution. This can be observed in Fig. 4-2. In Fig. 4-2, the specimen is not symmetric about the vertical axis because of the cross-frame elements were attached to the connection plate only on one side. This caused the girder subassembly to be loaded asymmetrically, even though the connection plate was symmetric with respect to the girder web.

One of the observations from the physical simulations was that although the implementation of a retrofit measure in the bottom web gap of the specimen was effective in preventing any further crack growth in the bottom web gap, the weak point shifted to the top web gap which was left untreated.
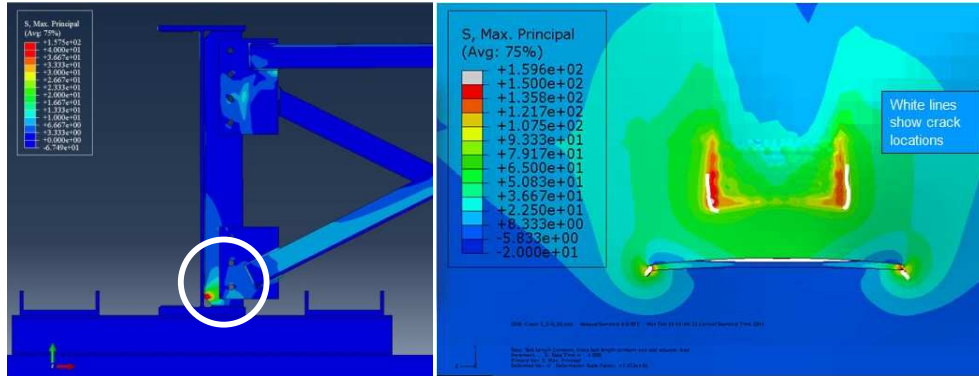
Figure 4-3: Crack growth comparison with maximum principal stress

Simulation results were consistent with that experimental observation. In models in which the girder subassembly was reinforced with the angles-with-plate retrofit only in the bottom web gap the stress demands at the top web gap remained very high, suggesting that a fatigue crack was likely to form at that location.

Retrofits and Stress Reduction

Various retrofit measures were modeled to evaluate which one was most effective in reducing the stress demand in the model, which would signify the most effective retrofit. Retrofits studied included crack stop holes, bolted angles to the web and flange and to the connection plate and flange, and composite blocks.

Applying crack stop holes at the tips of cracks in the simulation did not lower the stress demand at the bottom web gap, and therefore was considered to be a temporary stop-gap measure that would not prevent further crack growth (Fig. 4-3). In the physical simulations it was observed that after 14,000 cycles the crack reinitiated at the crack-stop hole drilled at both ends of the bottom horseshoe crack. The range of the calculated stresses in both pictures ranged between 0 – 276 MPa (0 – 40 ksi).

104
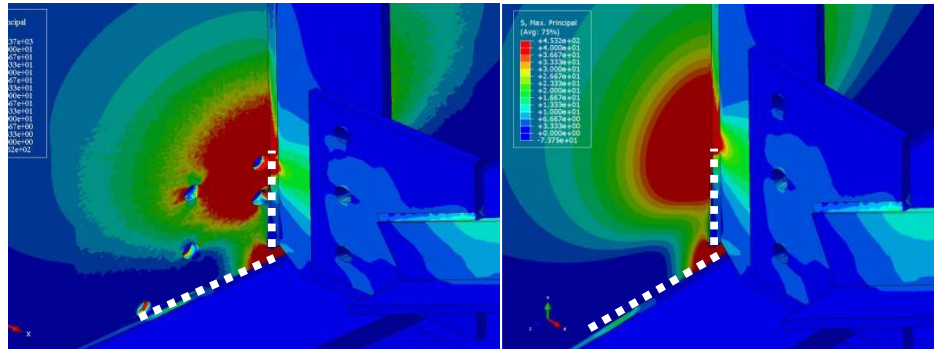
Figure 4-4: Calculated stress demands for a) crack-stop holes retrofit and b) unretrofited specimen

(white lines show crack locations)

Bolting angles on both sides of the connection plate in the bottom web gap to the web and adding a back plate to the fascia side of the web was shown to be an effective retrofit measure (Fig. 4-4). The maximum principal stress was greatly reduced in the bottom web gap, but the high stress on the fascia side of the web near the top web gap did not decrease. Experimental observations of a specimen retrofitted in this manner showed that after 1.2 million cycles, a distortion-induced fatigue crack initiated at the top web gap region of the subassembly.

A similar retrofit measure was studied, in which the angles were attached to the connection plate and bottom flange. This configuration was also found to be very effective in the simulations, but would be very difficult to construct because the concrete deck in a real bridge would have to be removed to attach bolts to the flange.
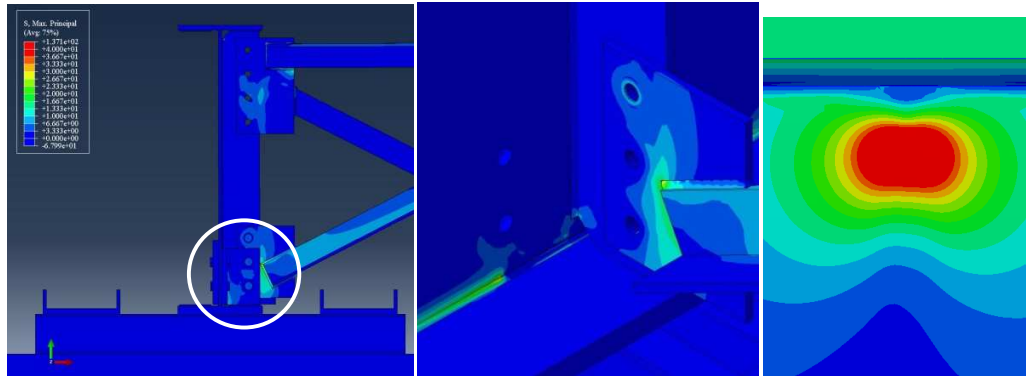
Figure 4-5: a) Retrofit location shown by the circle b) stress distribution in the bottom web gap c) stress demand at the fascia side of web in top web gap

Another retrofit measure, consisting of attaching composite blocks to the bottom web gap on both sides of the connection plate (Fig. 4-6), was also evaluated. Tie constraints were used to attach the composite block to the bottom flange, web, gusset plate, and connection plate. By connecting all of these parts, the bottom web gap was restrained which significantly reduced the stress demands. Composite blocks can be prefabricated to have any size or shape needed to fit the tight space in the bottom web gap. After this area was repaired, the high stresses demands shifted location to the weld connecting the bottom element of the cross-frame to the gusset plate. A larger composite block that covers this weld could be used to relive the stress at this location.
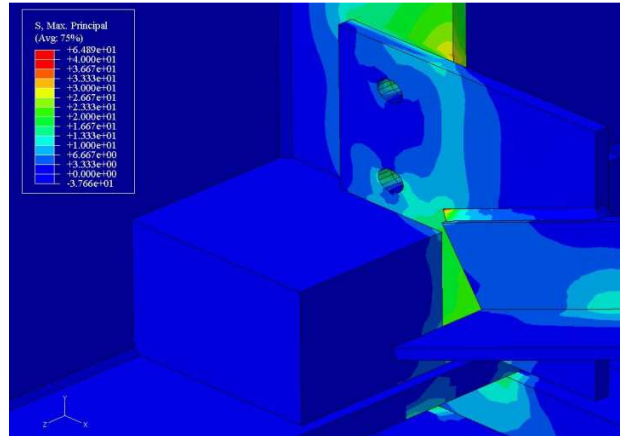
Figure 4-6: Calculated stress demand for composite block repair.

Identifying Locations with the Highest Potential for Fatigue Cracks

The location of the largest maximum principal stress demands in the computer models showed excellent correlation with crack locations (Fig. 4-2) found in the girder subassemblies. Figure 4-7 shows a simulation with crack stop holes. Locations of the largest maximum principal stress demands are shown in red and gray. These areas were found to be in close agreement with the location of observed cracks in the physical models.
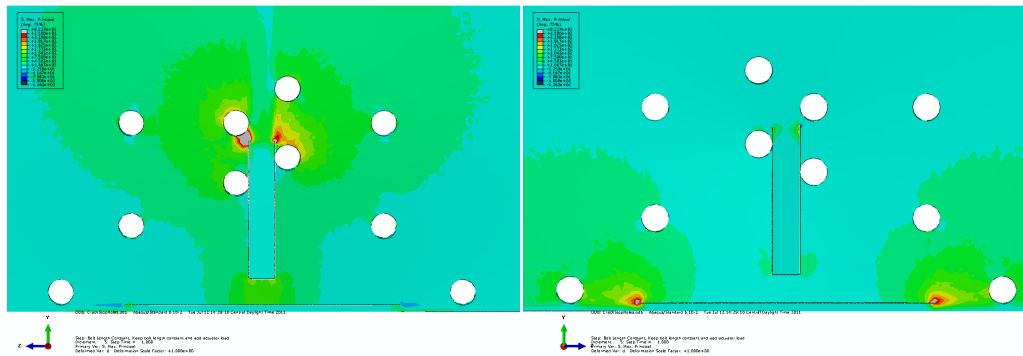
Figure 4-7: Calculated stress field for model with crack-stop holes a) connection-plate side b) fascia side

Conclusions

A suite of FE simulations was carried out to study the stress demand in the web gap region of girders subjected to distortion-induced fatigue. The main findings of the analytical study were the following:

- Of the three crack modeling techniques, removing elements, XFEM, and contour integrals, the XFEM crack modeling technique was the most simplistic and effective technique because cracked domains did not have to be remeshed and also because it is not required for cracks to lie at the edge of elements.

- Of the retrofit measures studied in the simulations the most effective were the angles-with-plate and the composite blocks. Both were equally effective, although the angles-with-plate retrofit measure is likely to be most economical and simplest to implement.

108

References

6.10, ABAQUS. 2010. *Simulia* Analysis User's Manual:10.6.1.

6.10, ABAQUS Version. 2010. *Simulia* CAE User's Manual 30.3.2.

Chen, C.R., and Y.W. Mai. 2010. Comparison of cohesive zone model and linear elastic fracture mechanics for a mode I crack near a compliant/stiff interface. *Engineering Fracture Mechanics*.

Cook, Gerry, Chris M. timbrell, and Miles Wiehahn. 2002. Using Abaqus to Analyse Fatigue Crack Growth Under the Combined Influece of Residual Stress and Cyclic External Load. *UK Abaqus User Group Conference*

Fisher, John W. 1984. Fatigue and Fracture in Steel Bridges: Case Studies.315.

Rabinovitch, Oded. 2008. Debonding analysis of fiber-reinforced-polymer strengthened beams: Cohesive zone modeling versus a linear elastic fracture mechanics approach. *Engineering Fracture Mechanics* 75 (10):2842-2859.

Zhao, Yuan, and W. M. Kim Roddis. 2007. *Fatigue Behavior and Retrofit Investigation of Distortion-Induced Web Gap Cracking*. Vol. 12: ASCE.

Zhu, C. L., J. B. Li, G. Lin, and H. Zhong. 2010. Study on the relationship between stress intensity factor and J integral for mixed mode crack with arbitrary inclination based on SBFEM. Paper read at 9th World Congress on Computational Mechanics and 4th Asian Pacific Congress on Computational Mechanics, WCCM/APCOM 2010, July 19, 2010 - July 23, 2010, at Sydney, NSW, Australia.

CHAPTER 5. CONCLUSIONS

Three different studies were carried out to investigate the potential for damage and to develop and evaluate repair techniques for distortion-induced fatigue. The first study concluded with the development of a new repair method, experimentally shown to be highly effective in limiting further crack growth due to distortion-induced fatigue in bridge girders. Major findings of the first study were:

- The angles-with-plate repair was a very effective method to reduce the propagation rate of fatigue cracks in girders damaged by distortion-induced fatigue.

- The angles-with-plate retrofit measure was effective in preventing distortion of the web gap region, drastically reducing stress demands calculated at the critical points. Finite element simulations showed that stress demands at the critical points of the web gap region reinforced with the angles-with-plate repair were on the order of 5% of those in the unreinforced configuration.

The second study investigated the repair of fracture-mode-1 with CFRP overlays. Main findings of the second study were:

- Experimentally observed reductions in stress range demand associated with the bonding of overlays were consistent with those observed in Finite Element simulations.

- Experimental results showed that bonding of pre-fabricated multi-layered CFRP overlays extended the fatigue-crack propagation lives of the steel specimens by as much as 50 times.   The observed increase in fatigue-crack propagation life was significantly higher with values ranging between 4.7 and 7.9 times reported in

110

previous studies on aluminum plates, steel plates, and steel beams. The main difference between the overlays used in this study and those used in other studies found in the literature is that the stiffness ratio *SF* was significantly higher.

The third paper described the simulations techniques used to evaluate the potential for fatigue damage and to perform preliminary evaluations of effectiveness of various retrofit measures to prevent further damage under fatigue loading. Major findings of the third study were:

- Of the three crack modeling techniques evaluated, i.e., removing elements, extended finite element method (XFEM), and contour integrals, the XFEM crack modeling technique was the most simplistic and effective technique because cracked domains did not have to be remeshed and because it is not necessary for cracks to lie at the edge of elements.

- The most effective of the retrofit measures for distortion-induced fatigue damage studied through FE simulations, were the angles-with-plate and the composite block retrofit measures.

For the two types of cracks evaluated, stress fields computed using high-resolution FE models showed good agreement between locations of peak stress demand and locations where the cracks formed in the physical models. The consistency between the two analysis shows that the FE models developed using the techniques described in the last paper can be used effectively to identify locations susceptible to fatigue damage, and to evaluate the effectiveness of various repair methods.

Experimental results showed that composite overlays, if properly bonded, are capable of preventing further crack growth and achieving run-out fatigue performance.

111

The angles-with-plate repair was shown to be a very economical and effective method to repair the web gap region of girders damaged by distortion-induced fatigue. This retrofit measure was also shown to be capable of achieving run-out fatigue performance, even though crack-stop holes were not drilled at the tip of the cracks.

The research presented in the three papers provide new and very effective alternatives for preventing and repairing distortion-induced fatigue damage in steel bridges. These retrofit techniques are valuable additions to the pool of methods already in use to mitigate this significant problem.

REFERENCES

Hassel, H.L. 2011. An Analytical Evaluation of Distortion-Induced Fatigue in Steel Bridges.

AASHTO, L. (2007). "AASHTO LRFD Bridge Design Specifications (2007)." American Association of State Highway and Transportation Officials.

Alemdar, F., A. Matamoros, C. Bennett, R. Barrett Gonzalez, and S.T. Rolfe. 2011. Use of CFRP Overlays to Strengthen Welded Connections under Fatigue Loading. Journal of Bridge Engineering 1:191.

Castiglioni, CA, JW Fisher, and BT Yen. 1988. Evaluation of fatigue cracking at cross diaphragms of a multigirder steel bridge. Journal of Constructional Steel Research 9 (2):95-110.

Cousins, TE, and JM Stallings. 1998. Laboratory Tests of Bolted Diaphragm-Girder Connections. Journal of Bridge Engineering 3:56.

Fisher, JW. 1990. Distortion-induced fatigue cracking in steel bridges: Transportation Research Board.

Hassel, H.L. 2011. An Analytical Evaluation of Distortion-Induced Fatigue in Steel Bridges.

Jajich, D, and AE Schultz. 2003. Measurement and Analysis of Distortion-Induced Fatigue in Multigirder Steel Bridges. Journal of Bridge Engineering 8:84.

Keating, P.B. 1994. Focusing on fatigue. Civil Engineering—ASCE 64 (11):54-57.

Keating, PB, and JW Fisher. 1987. Fatigue behavior of variable loaded bridge details near the fatigue limit. Transportation Research Record (1118).

Lindberg, A., and A. Schultz. 2007. Incorporation of Fatigue Detail Classification of Steel Bridges into the Minnesota Department of Transportation Database.

Roddis, K, and Y Zhao. 2001. Out-of-plane fatigue cracking in welded steel bridges. Welding Innovations 27 (2):2-7.

ASTM, D. 2000. 3039/D 3039M,". Standard Test Method for Tensile Properties of Polymer Matrix Composite Materials.

Lee, W. Y., and J. J. Lee. 2004. Successive 3D FE analysis technique for characterization of fatigue crack growth behavior in composite-repaired aluminum plate. Composite Structures 66 (1-4):513-520.

Liu, H. B., R. Al-Mahaidi, and X. L. Zhao. 2009. Experimental study of fatigue crack growth behaviour in adhesively reinforced steel structures. Composite Structures 90 (1):12-20.

Liu, H. B., Z. G. Xiao, X. L. Zhao, and R. Al-Mahaidi. 2009. Prediction of fatigue life for CFRP-strengthened steel plates. Thin-Walled Structures 47 (10):1069-1077.

Mall, S, and DS Conley. 2009. Modeling and validation of composite patch repair to cracked thick and thin metallic panels. Composites Part A: Applied Science and Manufacturing 40 (9):1331-1339.

Marquis, G, and A Kaehoenen. 1995. Fatigue testing and analysis using the hot spot method.

Naboulsi, S, and S Mall. 1996. Modeling of a cracked metallic structure with bonded composite patch using the three layer technique. Composite Structures 35 (3):295-308.

Sabelkin, V, S Mall, and JB Avram. 2006. Fatigue crack growth analysis of stiffened cracked panel repaired with bonded composite patch. Engineering Fracture Mechanics 73 (11):1553-1567.

Schubbe, JJ, and S Mall. 1999. Modeling of cracked thick metallic structure with bonded composite patch repair using three-layer technique. Composite Structures 45 (3):185-193.

Tavakkolizadeh, M, and H Saadatmanesh. 2003. Fatigue strength of steel girders strengthened with carbon fiber reinforced polymer patch. Journal of Structural Engineering 129 (2):186-196.

Umamaheswar, TVRS, and R Singh. 1999. Modelling of a patch repair to a thin cracked sheet. Engineering Fracture Mechanics 62 (2-3):267-289.

ABAQUS, Version 6.8-2, Simulia, 2009, http://www.simulia.com.

Barsom, J.M., and Rolfe, S.T. (1999). "Fatigue and fracture behavior of welded components." Fracture and Fatigue Control in Structures, 3rd ed., (10), American Society for Testing and Materials, West Conshohocken, PA, 35-53.

Roy, M., Lang, C., & May, I. (2009). Modelling composite repairs to cracked metal structures. Proceedings of the Institution of Civil Engineers. Structures and Buildings, 162(2), 107-113.

Hysol® 9412, Loctite 9412 Hysol Epoxy Adhesive, 2001, http://www.henkelna.com.

6.10, ABAQUS. 2010. Simulia Analysis User's Manual:10.6.1.

6.10, ABAQUS Version. 2010. Simulia CAE User's Manual 30.3.2.

Chen, C.R., and Y.W. Mai. 2010. Comparison of cohesive zone model and linear elastic fracture mechanics for a mode I crack near a compliant/stiff interface. Engineering Fracture Mechanics.

Cook, Gerry, Chris M. timbrell, and Miles Wiehahn. 2002. Using Abaqus to Analyse Fatigue Crack Growth Under the Combined Influece of Residual Stress and Cyclic External Load. UK Abaqus User Group Conference

Fisher, John W. 1984. Fatigue and Fracture in Steel Bridges: Case Studies.315.

Rabinovitch, Oded. 2008. Debonding analysis of fiber-reinforced-polymer strengthened beams: Cohesive zone modeling versus a linear elastic fracture mechanics approach. Engineering Fracture Mechanics 75 (10):2842-2859.

Zhao, Yuan, and W. M. Kim Roddis. 2007. Fatigue Behavior and Retrofit Investigation of Distortion-Induced Web Gap Cracking. Vol. 12: ASCE.

Zhu, C. L., J. B. Li, G. Lin, and H. Zhong. 2010. Study on the relationship between stress intensity factor and J integral for mixed mode crack with arbitrary inclination based on SBFEM. Paper read at 9th World Congress on Computational Mechanics and 4th Asian Pacific Congress on Computational Mechanics, WCCM/APCOM 2010, July 19, 2010 - July 23, 2010, at Sydney, NSW, Australia.